Injection Mechanisms in Laser Wakefield Acceleration

Dissertation

zur Erlangung des akademischen Grades

doctor rerum naturalium
(Dr. rer. nat.)
im Fach Physik

eingereicht an der
Mathematisch-Naturwissenschaftlichen Fakultät
Humboldt Universität zu Berlin

von
Dipl.-Phys. **Christian Koschitzki**

Präsident der Humboldt-Universität zu Berlin
Prof. Dr.-Ing. Dr. Sabine Kunst

Dekan der Mathematisch-Naturwissenschaftlichen Fakultät
Prof. Dr. Elmar Kulke

Gutachter:

1: Prof. Dr. Andreas Jankowiak
2: Prof. Dr. Lazlo Veisz
3: Prof. Dr. Matt Zepf

Tag der wissenschaftlichen Aussprache: 13.03.2017

Abstract

The acceleration of electrons in intense laser fields interacting with a plasma has been experimentally studied over two decades and is widely considered as a possible alternative to conventional RF-based accelerator concepts. The presented measurements are the first demonstration of Laser Wakefield Acceleration at the Max Born Institut and a setup was build to perform the described experiments. A detailed documentation of the applied diagnostics and their calibrations is shown. The current efforts in plasma source design are targeting two main topics. One topic is the development of methods to control particle trapping in the accelerating plasma wake. The other is the development of laser waveguides to maximize the acceleration length. Best performance regarding energy spread, stability and shot-to-shot fluctuation has been demonstrated in structures, that combine controllable injection and acceleration. This thesis focuses on controlled injection and two different methods will be compared. The first method of stimulated injection, presented in this thesis, is ionization injection, which typically causes electron trapping over an extended laser propagation distance. As electrons become injected at different positions, electrons will be accelerated over different distances, yielding a wide energy spread in the emitted electron beam. For this injection type, a threshold is found in terms of the product of laser power and plasma density, such that a correlation between the injection and the formation of an electron void ion column in the plasma wave is indicated.

The second stimulated injection method utilizes a supersonic phenomenon called shock front to stimulate a quasi-instantaneous injection. When a supersonic gas flow is disturbed by a sharp edge, a shock front is created and injection is stimulated at the crossing of the propagating laser pulse and the shock-front region. The shock front can be tuned by adjusting the position of the sharp edge and thus the position and angle of the shock front. It is found that the Mach number of the flow or the density transition in the shock front respectively, can be used to tune the total charge injected. This increase in total charge comes at the expense of an increased energy spread. Electron beams are demonstrated with an energy spread of less than 2% at peak energies of 300 MeV with 5 pC of charge. For the ionization injection as well as for the shock-front injection it is found, that the charge per energy interval and solid angle is constant and amounts to $(0.021 \pm 0.001)\,\mathrm{pC\,MeV^{-1}\,mrad^{-2}}$ for all observed electron beams. That the continuous injection and the quasi-instantaneous injection yield the same correlation between charge, divergence and energy spread, implies that this correlation is a property of the wakefield structure itself. So far it was assumed that charge per energy interval depends on the injection type alone and divergence was not yet considered in this context.

Zusammenfassung

Die Beschleunigung von Elektronen im Wechselwirkungsbereich hochintensiver Laserfelder mit einem Plasma, wird seit etwa zwei Jahrzehnten experimentell untersucht und wird als mögliche Alternative zu konventionellen Radiofrequenz basierten Beschleunigerkonzepten gehandelt. Die gezeigten Experimente sind die ersten Versuche zur Laser getriebenen Elektronenbeschleunigung am Max Born Institut. Entsprechend wird die Kalibrierung der eingesetzten Diagnostiken im Detail diskutiert werden. Aktuell werden beim Design von Plasmaquellen für Wakefield Experimente zwei Ziele verfolgt. Einerseits is man bemüht die Parameter, die zum Einfang von Elektronen führen, zu kontrollieren, anderseits wird versucht die Beschleunigungslänge mit Hilfe von Waveguides zu maximieren. Die besten Ergebnisse bezüglich Energiebreite, Stabilität und Schuß-zu-Schuß Fluktuation wurden mit kombinierten Strukturen demonstriert. Im Rahmen dieser Dissertation konzentriere ich mich auf kontrollierte Injektion und es werden zwei verschiedene Methoden gezeigt. Die erste demonstrierte Variante einer stimulierten Injektion ist die Ionisationsinjektion, welche typischerweise zu einem kontinuierlichen Elektroneneinfang über einen ausgedehnten Bereich entlang der Propagation des Lasers führt. Die injizierten Elektronen werden dadurch über unterschiedliche Längen beschleunigt, was zu einem breiten Energiespektrum des beschleunigten Eletronenpaketes führt. Für das Auftreten dieses Injektionstypes wurde ein Schwellwert in der Form eines Produktes aus Laserleistung und Plasmadichte gefunden, welcher auf einen Zusammenhang mit der Bildung eines, von Elektronen entleerten, Ionenkanals in der Plasmawelle schließen läßt.

Die zweite untersuchte Injektionsmethode basiert auf einem Überschallphänomen, welches eine quasi-instantane Injektion ermöglicht. Wird ein Überschall-Gasfluß durch eine scharfe Kante gestört, bildet sich ein scharfer Dichteübergang, bekannt als Schock Front, durch welchen eine Injektion stimuliert werden kann. Die Position und der Winkel der Schock Front können durch die Position der scharfen Kante manipuliert werden. Es wurde gezeigt, dass die Machzahl der Düse bzw. die Übergangshöhe der Schock Front dazu benutzt werden können, die injizierten Ladungsmenge zu kontrollieren. Eine Erhöhung der Ladungsmenge ist dabei mit einer Erhöhung der Energiebreite verknüpft. Es wurden Elektronenstrahlen demonstriert mit weniger als 2% Energiebreite bei einer Maximalenergie von 300 MeV und 5 pC Ladung. Es zeigte sich, dass sowohl bei Shock-Front Injektion als auch bei Ionisationsinjektion die emittierte Ladung pro Energieintervall und Raumwinkel konstant blieb, bei einem Wert von $(0.021 \pm 0.001)\,\mathrm{pC\,MeV^{-1}\,mrad^{-2}}$. Dass sowohl eine kontinuierliche als auch eine instantane Injektion dieselbe Korrelation zwischen Ladung, Divergenz und Energiebreite aufweisen, lässt darauf schließen, dass es sich um eine Eigenschaft der Plasmawelle selbst handelt. Bisher wurde angenommen, dass die emittierte Ladung pro Energieintervall nur von der gewählten Injektion abhängt und ein Zusammenhang mit der Divergenz wurde nicht berücksichtigt.

Contents

Introduction

Since the first theoretical prediction of plasma-based electron acceleration by Tajima and Dawson in 1979 [1] a vast number of experimental conformations and improved models have been published. Current models [2] predict multi 10 GeV electron beams under realistic experimental conditions and the current record of experimentally realized peak electron energy has been set by a team at the Lawrence Berkeley National Lab (LBNL) at 4.2 .GeV [3] over a distance of only 9 cm. Thus these machines are currently reaching comparable electron energies as classical radio frequency (r.f.) based accelerators with significantly reduced footprint. For comparison the Linear Coherent Light Source (LCLS) at the Stanford Linear Accelerator Center (SLAC) uses a 1 km long accelerator to achieve electron beams of 10 GeV peak energy. However, r.f. based accelerators outcompete the plasma based sources in other electron bunch parameters, that determine the usability of the accelerated electron bunches in Free Electron Lasers (FEL) or collision experiments. One of which is the stability of the electron beam parameters (see chapter 7). In 1994 at the Rutherford Appleton Laboratory in the UK Modena *et al.* showed electrons at peak energies of 44 MeV in a self modulated laser wakefield regime [4], almost 10 years after the existence of accelerating wakefields was shown at the University of California Los Angeles (UCLA) in the laser beatwave regime [5]. The difference was that for the first time electrons were not injected externally from a r.f source, but instead were trapped from the background plasma in a process often referred to as wavebreaking injection. This lifted the necessity of an external injector and made laser plasma based acceleration experiments significantly easier. In the past two decades, plasma based experiments have almost exclusively shown accelerated electrons trapped from the background plasma. In order to study the Laser Wakefield Acceleration (LWFA) mechanism experimentally, this method poses some challenges. If one wants to study the evolution of an injected electron bunch in an LWFA setup, the initial distribution needs to be at least constant, if not known. In the small scale accelerator experiments of typically a few millimeter, it is very challenging to create a localized injection of background electrons that remains constant, while the parameters of the accelerating part are changed. This is definitely true for the simplest target configuration of a gas cone produced by a supersonic jet (see section 8.2.1), where only the overall density can be changed for a given jet design. Other plasma sources like gas filled containers [6, 7] (see section

8.2.2) or discharge capillary waveguides [8] provide better control over the acceleration distance, but also do not provide independently tunable injection parameters. Typically it is assumed that, regardless of the injection condition, initially electrons have very little momentum in laser direction compared to the momentum they gain in the wakefield acceleration. Thus the available degrees of freedom, acceleration length and plasma density, are suitable to study the longitudinal momentum gain and models have been developed, that show a good agreement with experimental results [2]. In case of momentum perpendicular to the acceleration direction the initial distribution can not be neglected, because the initial product of spatial distribution width and momentum distribution width is expected to be preserved. Only recently an updated model for the wavebreaking injection of plasma background electrons, that can predict the onset of this injection mechanism in terms of a density threshold, has been published by Mangles *et al.* [9]. When designing targets with independent acceleration and injection parts, self injection in the acceleration part is to be avoided. It may even be recommended to avoid self injection completely and use methods of stimulated injection instead [10–12]. Operating below the density threshold for self injection is also advantageous for the acceleration itself, as current scaling laws predict better electron beam performance towards lower densities. Such injector/accelerator combinations have been demonstrated [13, 14] and significantly improved acceleration performance in terms of stability and injected charge. From the currently published injection methods and target types, a wide variety of combinations are possible. In order to design such an independently tunable plasma configuration, I will have to review the existing stimulated injection methods. In particular a method that intrinsically determines the position along the laser axis, at which electrons are injected into the accelerating structure, is of interest in this context. In the shock-front injection a supersonic phenomena is exploited, which leads to narrow density transition region at which electron injection is triggered. Earlier papers [11, 15] suggested that this method creates an initial electron distribution, that is largely independent of the density transition parameters and can easily be used to change the injection position. Thus it would allow to study the evolution of electron beam parameters as a function of acceleration length. At the Max Born Institut (MBI) the work presented in this thesis is the first investigation on laser driven electron acceleration. Thus the first challenge is, to provide basic infrastructure to perform electron acceleration experiments. Starting from the layout of the vacuum beamline and radiation safety (section 3), diagnostics for low density plasma (section 4) and detectors for high energy electrons (section 6) are discussed. I will show in this thesis how these devices can be absolutely calibrated to measure parameters like the plasma density and electron beam charge and energy distribution. In order to start an investigation of different plasma configurations, one needs to ensure that an unchanged plasma configuration exhibits comparable behavior on a daily base. I will present experiments that study the influence of the laser performance on the behavior of the electron acceleration (chapter 7). With this experience I will then

be able to study the dependence of electron beams on different types of plasma configuration (chapter 8). I will have to discuss some theory of these gas targets and will present measurements of those target properties in order to understand how they effect electron acceleration (characterization in section 4.3 and electron beam measurements in section 8.3).

Part I

Basics

1 Introduction to relativistic laser-plasma physics

In this first chapter I will introduce the basic properties of relativistic laser-plasma interactions. Starting in section 1.1, where the relevant mechanisms of ionization are discussed. In section 1.2 the propagation of waves and in particular electromagnetic (EM) waves in plasma are discussed and section 1.3 will show how single free electrons react with an oscillatory motion called quiver motion to the presence of an an infinite plane EM-wave. In this case the Woodward-Lawson [16] theorem applies, stating that no net energy transfer from the field to the electron is possible. The prerequisites for this theorem are easily violated for a finite field and particularly for a focused short pulse laser. The effect leading to a net energy transfer is called ponderomotive force and will be discussed in section 1.4. After it has been discussed how a laser pulse effects plasma and how plasma can effect a laser pulse, in section 1.5 it will be shown how this can drive instabilities and self modulation effects.

1.1 Ionisation

The plasma state of matter is defined by the presence of charged particles in a quasi-neutral state. This means that atoms are at least partially ionized and in the considered experiments this happens due to presence of the high intensity laser pulse. Considering a titanium sapphire laser system with a central wavelength of 800 nm, the corresponding photon energy of 1.55 eV is not sufficient to directly ionize Helium (24.6 eV for He^+ and 54.4 eV for He^{2+}). If at higher laser intensities the photon density is in the range of the atomic or molecular number density, then there is a non negligible chance that multiple photons are absorbed, causing multi photon ionization (MPI). For the perturbative approach in MPI it is assumed that atomic binding potential remains undisturbed by the laser field. This assumption remains roughly valid for a Keldysh parameter $\gamma_k > 1$ given by [17]

$$\gamma_k = \omega \sqrt{\frac{2E_{ion}}{I_L}} \tag{1.1}$$

with the laser angular frequency ω, an ionization energy E_{ion} and a laser intensity I_L. For our typical laser intensities $\gamma_k \ll 1$ and the laser strongly alters the atomic binding potential. This has been considered by Ammosov, Delone and Krainov [18]. A threshold intensity I_{thresh} can be derived at which the binding potential is suppressed by the laser enough, so electrons can escape spontaneously. In practical numbers it is given by

$$I_{thresh}\left[\mathrm{W\,cm^{-2}}\right] = 4 \times 10^9 E_{ion}^4\,[\mathrm{eV}]\,Z^{*2}, \tag{1.2}$$

with Z^* the charge of the resulting ion. The mechanism is called barrier suppression ionization (BSI). For the gases, used in this thesis, the thresholds are listed in table 1.1. Below this threshold the suppression of the binding potential can still increase the probability for tunneling ionization. The model shows a reasonable agreement with experiments for low Z gases. An accurate calculation of the injection rates needs to consider the finite laser pulse duration as well as the real 3D shape of the atom or molecule. The laser intensity in the presented experiments typically reaches values of $1 \times 10^{18}\,\mathrm{W\,cm^{-2}}$ or higher, so that Helium will become ionized picoseconds before the arrival of the main laser pulse (see section 5.2). The threshold intensities for N^{6+} and N^{7+} are on the same order of magnitude as our laser peak intensity, which plays a special role in the ionization injection mechanism (see sections 8.2 and 2.8).

Nitrogen					
Ion	N^{1+}	N^{2+}	N^{3+}	N^{4+}	
E_{ion}	14.5	29.6	47.5	77.5	eV
I_{thresh}	1.7×10^{14}	7.7×10^{14}	2.3×10^{15}	9.0×10^{15}	$\mathrm{W\,cm^{-2}}$
electron	N^{5+}	N^{6+}	N^{7+}		
E_{ion}	97.9	552.1	667.5		eV
I_{thresh}	1.5×10^{16}	1.0×10^{19}	1.6×10^{19}		$\mathrm{W\,cm^{-2}}$
Helium					
Ion	He^{1+}	He^{2+}			
E_{ion}	24.6	54.4			eV
I_{thresh}	1.5×10^{15}	8.8×10^{15}			$\mathrm{W\,cm^{-2}}$

Table 1.1: Ionization energies and corresponding laser intensities

1.2 Wave propagation in plasma

For the spatial and temporal scales, I am interested in, electrons can be treated as a fluid with the ions treated as a fixed neutralizing background. The dynamics of charged particles are described by the Maxwell equations, where bold fonts indicate

vectors:

$$\nabla \times \boldsymbol{E} = -\frac{\partial}{\partial t}\boldsymbol{B} \tag{1.3}$$

$$\nabla \cdot \boldsymbol{E} = \frac{\rho}{\epsilon_0} \tag{1.4}$$

$$\nabla \times \boldsymbol{B} = \frac{1}{c^2}\frac{\partial}{\partial t}\boldsymbol{E} + \mu_0 \boldsymbol{j} \tag{1.5}$$

$$\nabla \cdot \boldsymbol{B} = 0 \tag{1.6}$$

with the electric field $\boldsymbol{E}$, the magnetic field $\boldsymbol{B}$, charge density ρ and the current density $\boldsymbol{j}$ as functions of position $\boldsymbol{r}$ and t. c denotes the vacuum speed of light and is related to electric and magnetic field constant via $\epsilon_0\mu_0 c^2 = 1$. The magnetic field $\boldsymbol{B}$ can also be expressed in terms of a vector potential $\boldsymbol{A}$

$$\boldsymbol{B} = \nabla \times \boldsymbol{A} \tag{1.7}$$

This would be invariant for any scalar potential Φ

$$\boldsymbol{A} \Longrightarrow \boldsymbol{A'} = \boldsymbol{A} + \nabla\Phi \tag{1.8}$$

because in any case $\nabla \times (\nabla\phi) = 0$. This gauge invariance indicates a symmetry of the Maxwell equations, which is the invariance under Lorentz transformation. This leads to a degree of freedom when choosing the scalar potential. A common choice is called the Coulomb gauge ($\nabla \cdot \boldsymbol{A} = 0$) so that the scalar potential Φ represents the electrostatic Coulomb Potential and $\boldsymbol{A}$ is a purely rotational vector potential. The electric field in terms of these potentials can be written as

$$\boldsymbol{E} = -\frac{\partial}{\partial t}\boldsymbol{A} - \nabla\boldsymbol{\Phi} \tag{1.9}$$

With the continuity equation

$$\frac{\delta\rho}{\delta t} + \nabla\boldsymbol{j} = 0 \tag{1.10}$$

and assuming electrons initially at rest ($\nabla\boldsymbol{j} = 0$) the wave equation in matter for $\boldsymbol{A}$ reads as

$$\nabla^2\boldsymbol{A} - \frac{1}{c}\frac{\partial^2}{\partial t^2}\boldsymbol{A} = -\mu_0\boldsymbol{j} \tag{1.11}$$

A solution is the linearly polarized ($\hat{x}$) plane wave propagating in z direction

$$\boldsymbol{A} = A_0 e^{i(kz-\omega t)}\hat{x} \tag{1.12}$$

With the background density N_0 I can introduce the plasma frequency ω_p

$$\omega_p^2 = \frac{e^2 N_0}{m_e\epsilon_0}, \tag{1.13}$$

and a dispersion relation for light propagating in a cold collisionless plasma is obtained

$$\omega^2 = \omega_p^2 + k^2 c^2 \tag{1.14}$$

This dispersion relation has no solutions for light frequencies lower than the plasma frequency, which means light can only propagate if ($\omega \geq \omega_p$). Or respectively there is a critical density at which our laser can not propagate through the plasma anymore. For our laser wavelength of 800 nm this critical density is $N_{crit} = 1.74 \times 10^{21}\mathrm{cm}^{-3}$. Metals are reflective for the exact same reason, as their conducting electrons form a highly dense electron plasma. With the phase velocity $v_{ph} = \omega/k = c/\eta$ and the group velocity $v_g = \mathrm{d}\omega/\mathrm{d}k = c\eta$, the refractive index can be obtained as

$$\eta = \sqrt{1 - \frac{\omega_p^2}{\omega^2}} \tag{1.15}$$

Thus the refractive index of a plasma is smaller than one, approaching zero as the wave frequency approaches the plasma frequency. The phase velocity in plasma can be greater than c, while the group velocity is smaller than c. I have stated that ions are treated as immobile. This can be checked by inserting the ion mass and charge into the definition of the plasma frequency (Eq. 1.13) to obtain the ion frequency ω_{ion}. The approximation remains valid as long as the longest considered timescale is still shorter than $1/\omega_{ion}$. If the continuity equation 1.10 is combined with the equation of motion for an electron in an electric field

$$m_e \frac{d\boldsymbol{u}}{dt} = -e\boldsymbol{E} \tag{1.16}$$

where $\boldsymbol{u}$ is the electrons velocity, a dispersion relation can be obtained [17] as follows

$$\omega^2 = \frac{e^2 N_0}{\epsilon_0 m_e} = \omega_p^2 \tag{1.17}$$

According to this all plasma oscillations have the same frequency, which is the plasma frequency, independent of their wavelength. For a warm plasma the thermal electron pressure needs to be taken into account and this result modifies to

$$\omega^2 = \omega_p^2 + 3k^2 v_{th}^2, \tag{1.18}$$

where v_{th} is the thermal electron velocity. For typical densities $\omega_p^2 \gg 3k^2 v_{th}^2$. This means the propagation of light, as well as plasma density waves, largely depend on the plasma frequency, which itself is mostly defined by the plasma density. A contribution from relativistic mass gain to the electron mass in equation 1.13 will be discussed in section 1.5.1.

1.3 Single electron in EM-field

In order to derive the relativistic motion of a charged particle in an electromagnetic field one starts from the relativistic Lagrangian

$$L(\boldsymbol{r}, \boldsymbol{u}, t) = -mc^2\sqrt{1-\beta^2} - e\boldsymbol{u}\boldsymbol{A} + e\Phi \tag{1.19}$$

with $\beta = u/c$ and the Euler-Lagrange equation.

$$\frac{d}{dt}\frac{\partial L}{\partial \boldsymbol{u}} - \frac{\partial L}{\partial \boldsymbol{r}} = 0 \tag{1.20}$$

The equation of motion can then be obtained as

$$\frac{d}{dt}(\boldsymbol{p} - e\boldsymbol{A}) = -(\nabla e\boldsymbol{A}) \cdot u + \nabla e\Phi \tag{1.21}$$

Using the fact that $\frac{d}{dt} = (\frac{\partial}{\partial t} + \boldsymbol{u} \cdot \nabla)$, the vector identity $\boldsymbol{u} \times \nabla \times \boldsymbol{A} = (\nabla \boldsymbol{A}) \cdot \boldsymbol{u} - (\boldsymbol{u} \cdot \nabla)\boldsymbol{A}$ and the relations between fields and potentials given in equations 1.7 and 1.9, I can retrieve the well known equation of motion in terms of $\boldsymbol{E}$ and $\boldsymbol{B}$.

$$\frac{d\boldsymbol{p}}{dt} = -e(\boldsymbol{E} + \boldsymbol{u} \times \boldsymbol{B}) \tag{1.22}$$

and the canonical (e.g. Lorentz invariant) momentum

$$\boldsymbol{p}_{can} = \frac{\partial L}{\partial \boldsymbol{u}} = \frac{m\boldsymbol{u}}{\sqrt{1-\beta^2}} - \frac{e}{c}\boldsymbol{A} = \boldsymbol{p} - \frac{e}{c}\boldsymbol{A} \tag{1.23}$$

with $\boldsymbol{p} = \gamma m\boldsymbol{u}$ and $\gamma = 1/\sqrt{1-\beta^2}$. Introducing the normalization $\boldsymbol{A} = e\boldsymbol{a}/mc$ for the vector potential and solving for the plane wave in the form

$$\boldsymbol{a} = a_0 \cos(i\Phi)\hat{x} \tag{1.24}$$

with the phase $\Phi = (kz - \omega t)$, the following relation can be found [17]

$$\gamma = 1 + \frac{a^2}{2}, \tag{1.25}$$

for an electron initially at rest. Using the definition $\gamma = E_{Kin}/E_0 + 1$ with the rest energy E_0 it can be seen that the non relativistic definition $E_{Kin} = \frac{1}{2}mu^2$ would require $u = c$ if $a_0 = 1$. In practical units a_0 reads as

$$a_0 = \sqrt{\frac{I_0\left(\frac{W}{cm^2}\right) \times \lambda^2\,(\mu m^2)}{1.37 \times 10^{18}}} \tag{1.26}$$

and for a wavelength of 800 nm an $a_0 = 1$ equals an intensity of $2.1 \times 10^{18} W/cm^2$. This wavelength dependent intensity is typically referred to as relativistic threshold

intensity. These intensities can be reached in our laser focus and thus a theoretical description of the laser plasma interaction requires a full relativistic treatment. Solving the equation of motion 1.21 for the linearly x-polarized plain wave with propagation direction z, the following set of orbit equations can be obtained [17].

$$x = \frac{ca_0}{\omega} sin(\Phi) \tag{1.27}$$

$$z = \frac{ca_0^2}{4\omega}(\Phi + \frac{1}{2} sin(2\Phi)) \tag{1.28}$$

Figure 1.1 **a)** shows the trajectory described by equations 1.27 and 1.28. This motion is the sum of a drift motion and an oscillatory motion. It has to be noted that the drift motion in the presence of the field is not related to an energy transfer between field and particle. A particle initially at rest will be at rest again, if the field is turned off. If we observe the orbit from a comoving average rest frame, the orbits form a "'figure 8"' (1.1 **b)**). The fast oscillatory motion is called the quiver motion and electrons can reach velocities close to the speed of light. The above considerations are only strictly valid for an infinite plane wave, but hold if the field varies little on the scale of its wavelength.

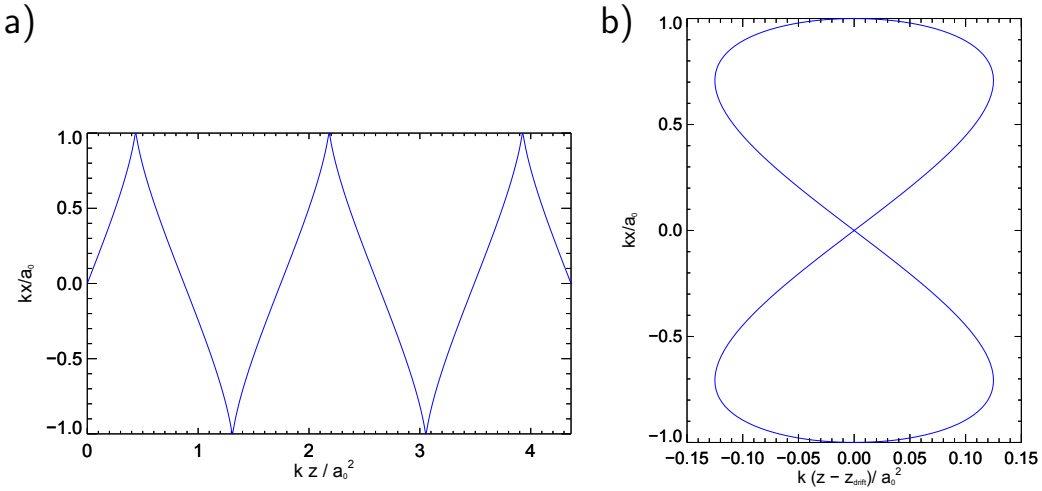

Figure 1.1: Electron trajectories in plane wave normalized to k/a_0 in x and k/a_0^2 in z direction. **a)** shows the lab frame and **b)** shows the motion from the perspective of a co-moving average rest frame.

1.4 Ponderomotive force

After deriving the fast oscillatory motion of the electrons in the presence of a laser, I now consider a time average $\langle\rangle$ over the fast oscillation. This yields a net momentum gain called ponderomotive force and is well known [19] for $a_0 \ll 1$ for the non relativistic case. From taking a time average over the fast laser period of the equation of motion for an electron in an electromagnetic field one can derive the following equation

$$\frac{d\langle \boldsymbol{p}\rangle}{dt} = -\frac{e^2}{2m_e\omega_0^2}\nabla\langle E^2\rangle = -\frac{e^2}{2m_e}\langle A^2\rangle = -\frac{1}{2}m_e c^2\nabla\langle a^2\rangle, \tag{1.29}$$

The derivation of this expression relies on the commonly used non relativistic approximation of neglecting the $\boldsymbol{v}\times\boldsymbol{B}$ term against the contribution of the electrical term $\boldsymbol{E}$ in the equation of motion 1.22. While this approximation must be dropped in order to derive a correct relativistic description, another approximation must be applied in the relativistic case. This is that the characteristic scale of the laser pulse envelope must be larger than the amplitude of the fast oscillatory motion, i.e. the laser wavelength. This applies to the transverse gradients, i.e. $S_{trans} = \frac{1}{k_0 w_0} \ll 1$ with focal waist w_0, as well as for the pulse length, i.e. $S_{time} = \frac{\lambda_0}{c\tau}$, but also requires the initial velocity of the electron, normalized to c, to be small compared to both S_{trans} and S_{time}. Quesnel and Mora [20] have performed accurate calculations using the relativistic motion of an electron and electromagnetic fields, that describe a focused laser pulse. Their calculations yield the following expression for the relativistic ponderomotive force

$$\frac{d\langle \boldsymbol{p}\rangle}{dt} = -\frac{e^2}{2m_e}\langle A^2\rangle = -\frac{1}{2}m_e c^2\frac{1}{\langle\gamma\rangle}\nabla\langle a^2\rangle, \tag{1.30}$$

where $\langle\gamma\rangle$ is the averaged gamma over a fast oscillation. This means the ponderomotive force is reduced due to the relativistic mass increase gained in the quiver motion. Quesnel and Mora state that the derivation of the relativistic ponderomotive force is highly dependent on the description of the laser field as it focuses and diffracts.

1.5 Relativistic cold plasma and nonlinear plasma effects

We have seen that the relativistic expression for the ponderomotive force can be derived by taking the average mass increase due to quiver motion into account. In a similar fashion we can now modify the non relativistic expressions for the cold plasma. As the plasma frequency depends on the electron mass, it can be modified

to

$$\omega_{prel} = \sqrt{\frac{N_0 e^2}{\langle\gamma\rangle m_e \epsilon_0}}, \tag{1.31}$$

One can immediately see that now our index of refraction is also altered to

$$\eta = \left(1 - \frac{\omega_p^2}{\langle\gamma\rangle\omega_0^2}\right)^{\frac{1}{2}} \tag{1.32}$$

Thus the mere presence of a high intense laser induces a change in the index of refraction. If we now assume a relativistically underdense plasma, i.e. one in which $\frac{\omega_p^2}{\langle\gamma\rangle\omega_0^2} \ll 1$, we can expand the refractive index to:

$$\eta = 1 - \frac{1}{2}\frac{\omega_p^2}{\langle\gamma\rangle\omega_0^2} \tag{1.33}$$

The Lorentz factor in terms of the time averaged normalized vector potential for linearly polarized light is given by $\langle\gamma\rangle = 1 + \frac{a_0^2}{4}$. We may also consider that the ponderomotive force will lead to an actual electron displacement and thus perturbations in the plasma density, as well as perturbations of the local frequency of the laser due to gradients in the index of refraction. If these are in the form $N = N_0\frac{\delta N}{N_0}$ and $\omega_L = \omega_0 + \frac{\delta\omega_L}{\omega_0}\omega_0$ we can obtain for the index of refraction

$$\eta = 1 - \frac{1}{2}\frac{\omega_p^2}{\omega_0^2}\left(1 + \frac{\delta N}{N_0} - \frac{2\delta\omega_L}{\omega_0} - \frac{a_0^2}{4}\right) \tag{1.34}$$

This expression is only valid for small perturbations of density and frequency and weakly relativistic lasers, but allows some physical insight. In the following we will only consider a laser traveling in a homogeneous plasma, and thus perturbations are caused by the laser itself. External density modifications in longitudinal as well as in transverse direction may be applied to further exploit the effects described.

1.5.1 Transverse focusing

A transverse variation of the refractive index will curve the wavefront of the laser towards the higher refractive index. In laser pulses the intensity is higher at the center, which leads to a higher relativistic mass gain and thus higher refractive index at the center. This rotationally symmetric index of refraction around the beam center causes a wavefront curvature similar to a focusing lens and is thus commonly referred to as 'relativistic self-focusing'. In addition the ponderomotive force pushes electrons away from the center, leading to a lower density at the center and thus a higher refractive index at the center as well. For the case of relativistic self-focusing it is possible to derive a threshold at which the lasers diffraction is

balanced and thus the laser is guided. In order to find expression for the divergence of a laser, we can examine the variation in phase velocity at a distance w from the center. If the phase velocity differs across the wavefront, that will lead to a curved wavefront which represents a focusing (or defocusing) beam. Assuming an initially flat wavefront at $t = 0$ with a local phase velocity $v_{\phi 1}$ at a point x_1 on the laser axis and second point x_2 with distance w from the center and a phase velocity $v_{\phi 2}$, the phase front will, after a short time Δt, have a tilt by an angle $\theta \simeq \Delta v_\phi \Delta t/w$. By using the fact that $\Delta v_\phi = w\frac{\delta v_\phi}{\delta r} = -w\frac{c}{\eta^2}\frac{\delta \eta}{\delta r}$ we can express the time dependent change of v_ϕ in terms of the transverse refractive index

$$\frac{\delta \theta}{\delta \tau} = -\frac{c}{\eta^2}\frac{\delta \eta}{\delta r} \tag{1.35}$$

If we now consider that energy flows perpendicular to the wavefront with the group velocity v_g, we can state that there is transverse energy flow proportional to $v_g sin\theta \simeq v_g\theta$. Since a change in the energy contained in the focal spot corresponds to a change in focal spot size, we can obtain an expression for rate of change of the focal spot

$$\frac{\delta w}{\delta \tau} = -\frac{c^2}{\eta}\frac{\delta \eta}{\delta r}\Delta t, \tag{1.36}$$

where we used the fact that the group velocity is given by $v_g = c\eta$. Thus the 'acceleration' of the spot size due to the presence of plasma is

$$\frac{\delta^2 w}{\delta \tau^2} = -\frac{c^2}{\eta}\frac{\delta \eta}{\delta r} \tag{1.37}$$

While this expression is valid for any kind of refractive index profile, we will now only consider the relativistic part of equation 1.34. Assuming that a guiding threshold will occur when the laser approaches relativistic intensities, i.e. $a_0^2 < 1$ and that the beam profile remains Gaussian so that the beam envelope is described by $a(r,z) = a_0 exp\left(-\frac{r^2}{\omega^2(z)}\right)$. The refractive index is then:

$$\eta = 1 - \frac{1}{2}\frac{\omega_p^2}{\omega_0^2}\left(1 - \frac{a_0^2(r,z)}{4}\right) \tag{1.38}$$

Neglecting terms of the order ω_p^4/ω_p^4 equation 1.37 then becomes

$$\frac{\delta^2 w}{\delta \tau^2} = -\frac{c^2}{8}\frac{\omega_p^2}{\omega_0^2}\frac{\delta}{\delta r}a^2(r,z) \tag{1.39}$$

Assuming the laser envelope is approximately

$$\frac{\delta}{\delta r}a^2(r,z) \approx \frac{|a_0^2|}{w_0}, \tag{1.40}$$

we find for the relativistic self-focusing that

$$\frac{\delta^2 w}{\delta \tau^2} = -\frac{c^2}{8}\frac{\omega_p^2}{\omega_0^2}\frac{|a_0^2|}{w_0}. \tag{1.41}$$

In order to derive a balance between relativistic self-focusing and the natural diffraction in the form

$$\frac{\delta^2 w}{\delta \tau^2} \mid \text{rel focusing} + \frac{\delta^2 w}{\delta \tau^2} \mid \text{diffraction} = 0 \tag{1.42}$$

we can use the well know function for the beam waist of a Gaussian beam as a function of distance to the focus

$$w = w_0 \left(1 + \frac{z^2}{z_R^2}\right)^{\frac{1}{2}} \tag{1.43}$$

Where $z_R = \pi w_0^2/\lambda$ is the Rayleigh length. If we assume the region of interest being near the focus of the laser so that $z < z_R$ and use the fact that $\frac{\delta z}{\delta t} \simeq c$ we can approximate the second term of equation 1.42 by differentiating the equation 1.43 with respect to time and obtain

$$\frac{\delta^2 w}{\delta \tau^2}_{\text{diffract}} = \frac{4c^4}{\omega_0^2 w_0^3} \tag{1.44}$$

We can now insert equations 1.41 and 1.44 into equation 1.42 and obtain

$$w_0^2 |a_0^2| = 32\frac{c^2}{\omega_p^2} \tag{1.45}$$

Since a_0^2 is related to the intensity of the laser pulse through

$$a_0^2 = \frac{e^2}{4\pi^2 m_e^2 c^6 \epsilon_0} I_0 \lambda^2 \tag{1.46}$$

and the power P is defined as peak intensity times area of the laser pulse

$$P = \frac{m_e^2 c^3 \omega_0^2}{16 e^2} a_0^2 w_0^2 \tag{1.47}$$

Then equation 1.45 yields that a threshold power exists for which relativistic self-focusing occurs in the form

$$P > P_{crit} = 2\frac{m_e^2 c^5}{e^2}\frac{\omega_0^2}{\omega_p^2} = 17.3\frac{N_c}{N} GW \tag{1.48}$$

where N_c is the critical density for which a laser with a given wavelength can propagate in a plasma. This means for underdense plasmas where $N/N_c < 1$, the

threshold decreases with increasing density. The fact that equation 1.48 does only depend on power, leads to a self balanced guiding at $P = P_c$. That means that the spot size remains constant over the guided range. However, work by Sprangle *et.al.* [21] suggests that relativistic self guiding is ineffective for pulses shorter than $1/\omega_p$, since the laser is modulated on the plasma time scale, instead of on the laser time scale. Work by Sun et al suggests that the ponderomotive charge displacement is severe for $P/P_c > 1$ leading to a cavitated bare ion column that can be used to guide the laser pulse as shown by Delfin *et.al.* [22]. This has been done with longer laser pulses, where the ponderomotive force and the repelling force of the ion channel balance each other. For short laser pulses no rigorous analytical solution is available right now, but in the work of W. Lu *et. al.* [2] it is implied, that his matching condition for an optimal LWFA

$$a_0 \approx 2 \left(\frac{P}{P_c} \right)^{\frac{1}{3}} \tag{1.49}$$

also gives a matched self guiding with little laser spot size oscillations for $P/P_c > 8$ according to their simulations. If $P/P_c \geq 8$ together with equation 1.49 are fulfilled than for a given focal length density and power are fixed. In order to optimize the ratio of density and power for maximum electron energy gain, one may want to drop this condition, but if no guiding occurs electron acceleration will be limited by the Rayleigh length. LWFA experiments designed to reach the highest possible electron energy gain, usually introduce an additional degree of freedom by applying some form of external guiding [8].

1.5.2 Longitudinal modulation

A highly intense laser pulse traveling in an underdense plasma can experience a comoving gradient of the index of refraction, either caused by the laser envelope and relativistic refractive index or by displacement of electrons due to ponderomotive force. This leads to a difference of the phase velocity as well as the group velocity of the laser along the laser pulse. While both changes cause different effects they can not occur independent of one another. If two points z_1 and z_2 longitudinally along the laser pulse, initially separated by a distance L and traveling at different group velocities are considered, a change in separation will occur after a time Δt

$$\Delta L = (v_g 2 - v_g 1)\, \Delta t \tag{1.50}$$

The difference in group velocity over a distance L can be written as gradient of the group velocity $\Delta v_g \approx \frac{\delta v_g}{\delta z} L$ and if I move into a comoving reference frame with the laser pulse by $\xi = x - ct$ and $\tau = t$ I find the rate of change as:

$$\frac{1}{L} \frac{\delta L}{\delta t} = -c \frac{\delta \eta}{\delta \xi} \tag{1.51}$$

Considering that electrons get expelled by the laser, the density is lower at the end of the pulse than at the front. This means that the front moves slower than the back and the pulse will be compressed. For pulses longer than c/ω_p we will show that successive compression and stretching will cause the laser pulse to break up into several beamlets separated by c/ω_p.

In a similar fashion I consider now two points separated by a 2π phase difference, i.e. separated by one wavelength. The phase at these two points can now travel at different phase velocities, but since we have defined the difference as 2π, this corresponds to a change in wavelength after a time Δt. If the change in phase velocity is small over a wavelength I can write this as $\Delta v_\phi = \frac{\delta v_\phi}{\delta z}\lambda_0$ and obtain the rate of change as

$$\frac{\delta\lambda}{\delta t} = \frac{\delta v_\phi}{\delta z}\lambda_0 \tag{1.52}$$

If this is expressed in terms of frequency rather than wavelength and the refractive index rather than $\frac{\delta v_\phi}{\delta z}$ and change to comoving frame I obtain for the rate of change of the laser frequency

$$\frac{1}{\omega}\frac{\delta\omega}{\delta\tau} = \frac{c}{\eta^2}\frac{\delta\eta}{\delta\xi} \tag{1.53}$$

Considering the same direction of the gradient as in the case of pulse compression above, I obtain a frequency up shift. This is often referred to as 'photon acceleration'.

1.5.3 Modulation instabilities

So far I have considered how a change in the plasma, caused by a laser pulse, can act back on the laser. Now this change can then further increase the original perturbation leading to a family of so called 'modulation instabilities', of which the most important shall be briefly discussed in this section. Generally I need to describe how the laser envelope, $\langle a^2\rangle$, is modulated by changes in refractive index. It can be shown that, if the classical action of the laser field (equivalent to the number of photons) is conserved, we can write:

$$a^2\omega_L w^2 L = constant \tag{1.54}$$

For most underdense plasma interaction the conservation of classical action is a good assumption [23], but this excludes all absorption processes as for example ionization. Equation 1.54 thus implies that the vector potential can only be changed by the three methods described above, by longitudinal bunching (changes in L), photon acceleration (changes in ω_L) and transverse focusing / defocusing. A modulation to the vector potential causes an associated change in the ponderomotive force of the laser. It can be shown that the response of the plasma to the

ponderomotive force is given by [23]

$$\left(\frac{\delta^2}{\delta t^2} + \omega_p^2\right)\frac{\delta n}{n} = c^2\nabla^2\frac{\langle a^2\rangle}{2} \tag{1.55}$$

To calculate the growth rate for a given instability one now has to calculate the rate at which the vector potential modulates the refractive index as well as the rate at which a perturbation in the refractive index modulates the vector potential. By combining these two rates and using Fourier analysis one can solve for the growth rate of the instability.

1.5.3.1 Longitudinal instabilities

The first instability I want to consider is a 1D longitudinal instability and can thus only interact with the laser via pulse compression and photon acceleration. I consider a sinusoidal perturbation in the refractive index, which for example can be caused by a low amplitude plasma wave. For pulses longer than c/ω_p successive compression and stretching will cause a sinusoidal modulation of the laser envelope at the plasma frequency. The effect of the resulting bunching and photon shift on $\langle a^2\rangle$ can be written as a rate equation using equations 1.51 and 1.53:

$$\frac{\delta}{\delta\tau}\langle a^2\rangle = \frac{\delta\eta}{\delta\tau}\langle a^2\rangle - \frac{c}{\eta^2}\frac{\delta\eta}{\delta\xi}\langle a^2\rangle \tag{1.56}$$

This bunching of the laser pulse can couple back to the plasma via harmonic oscillator equation 1.55 and reinforce the initial modulation. A modulated laser envelope can easiest be described as a beating between two frequencies separated by the beat frequency. Thus in the laser spectrum satellites will appear shifted from the fundamental by ω_p. As the amplitude of the plasma wave grows more satellites can appear shifted by integers of ω_p. With the two rates of change 1.55 and 1.56 Mori [23] has applied the method described above to derive the growth rate of this instability to be

$$\gamma_0 = \frac{\sqrt{2}}{4}\frac{\omega_p^2 a_0}{\omega_0} \tag{1.57}$$

Thus this instability grows faster for higher densities and higher laser intensities, which is a typical result for modulation instabilities. In real plasma experiments the laser is tightly focused and the transverse dimensions are usually also on the order c/ω_p. This means that in the longitudinal regions with lower intensity the transverse focusing will be weaker and diffraction will be increased and vice versa. Thus in realistic 3D scenarios the growth rate of the longitudinal instability will be enhanced by transverse effects.

1.5.3.2 Transverse instabilities

A transverse instability must be connected to self-focusing / diffraction, which can either arise due to ponderomotive or relativistic effects. One instability of that kind is filamentation where the beam breaks up into an number of filaments. This can arise due to a local guiding, seeded by transverse density or beam modulation, rather than a guiding of the full beam, which then enhances itself and separates the filaments from each other. This has been observed in experiments [24, 25] and in theory [26, 27]. It is usually an undesirable effect in LWFA experiments, since the local intensity is lower than in the case of no filamentation. Another instability does indeed affect the beam globally and causes the beam to kink or hose as it propagates through the plasma. This so called 'Hosing Instability' arises from an initially small perturbation of the laser centroid, creating an asymmetric plasma wave. The asymmetry in the plasma wave will then enhance the original perturbation in the laser profile [28]. Hosing instabilities have been experimentally observed by Kaluza *et. al.* [29] using shadowgraphy.

2 Laser Wakefield Acceleration

As a laser propagates in an underdense plasma, it will push electrons out of the way due to the ponderomotive force. These electrons will oscillate at a frequency ω_p. As the laser propagates with the group velocity $v_g \approx c\sqrt{1-\frac{\omega_p^2}{\omega_0^2}}$ it will continuously push electrons out of the way. The phase difference between a region where the oscillation started at $t = 0$ and that where the oscillation started at a time $t = \Delta t$ is therefore $\Delta\Phi = 2\pi v_g \Delta t/\lambda_p$. Although each oscillating region is (in a cold plasma) essentially independent, the laser drives a plasma wave with a phase velocity equal to the group velocity of the laser. This means the plasma wave has also a wavelength given by $\lambda_p = \frac{2\pi v_g}{\omega_p}$. Starting from an electromagnetic field oscillating in transverse direction to laser propagation direction, this condition generates a region from quarter a plasma wavelength to half a plasma wavelength behind the laser pulse and on the laser axis, where a temporally constant electric field in laser propagation direction is generated. This is suitable to transfer energy from the laser to charged particles that are co-propagating with the laser pulse in that region. This was first suggested by Tajima and Dawson [1] in 1979. They not only discussed wave generation by laser pulses shorter than a plasma period, but also the possibility of generating waves with pulse trains, where individual pulses are separated by a plasma wavelength. As I have shown in section 1.5.2 this will automatically occur for longer laser pulses and may even be seeded using a two laser setup, tuned to a beat frequency that equals the plasma frequency. This Laser Beat Wave Acceleration [5] and self modulated acceleration [4] were the first experimental realizations of laser plasma acceleration. In the further description I will however only discuss wave excitation phenomena caused by single pulses. The physics of plasma waves changes drastically from the linear regime, where the density is only slightly disturbed compared to background density $\delta N/N_0 \ll 1$ as compared to high amplitude nonlinear waves where $\delta N/N_0 \to 1$. There is a limit to which the amplitude of a plasma wave can grow called the wave breaking limit caused by non linearity of the electron oscillation. Since highest accelerating fields are desired, the nonlinear regime will be further discussed and a phenomenological scaling law for the electron energy, following the work of W. Lu *et.al.* [2], will be presented. In order to accelerate electrons certain conditions need to be fulfilled to trap electrons from the background plasma in order to accelerate them. The trapping condition will also be taken into account in order to determine a working regime for our

LWFA.

2.1 Linear plasma wave

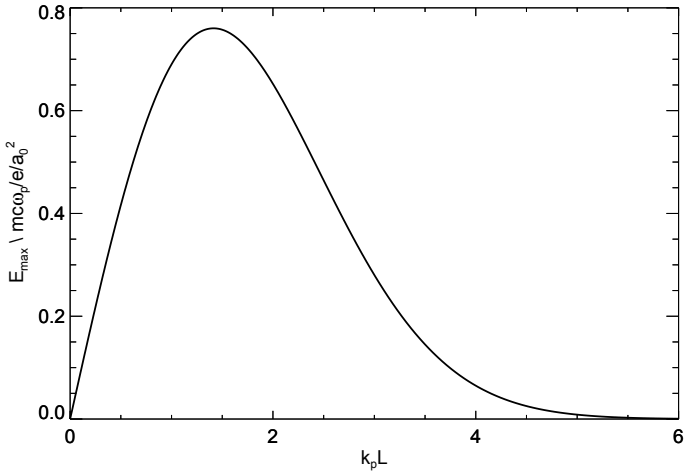

Figure 2.1: Wave amplitude as function of k_pL has a maximum at $\sqrt{2}$ for $a_0 \ll 1$.

Several publications have covered the generation of plasma waves in the standard wakefield regime [30, 31]. The most elegant equation can be derived from the linearized electron fluid equations [32]

$$\left(\frac{\delta^2}{\delta t^2} + \omega_p^2\right)\frac{\delta n}{n_0} = c^2\nabla^2\frac{\langle a^2\rangle}{2} \tag{2.1}$$

This equation represents a forced oscillator type of equation, where the driving force is the ponderomotive force $\nabla\langle a^2\rangle/2$ and the restoring force is the plasma response due to space charge effects $\omega_p^2\delta N/N_0$. The solution to this equation is found by the method of Green's function.

$$\frac{\delta N}{N_0} = \frac{c^2}{\omega_p}\int {}_0^t dt' sin\omega_p(t-t')\nabla^2\frac{a^2}{2} \tag{2.2}$$

In one dimension Gorbunov [30] has derived a solution for the amplitude of the plasma wave driven by a Gaussian profile laser pulse of the form $a^2 = a_0^2 exp(-\zeta^2/L^2)$(where $\zeta = z - v_g t$) with amplitude $a_0 \ll 1$

$$\frac{E_{max}}{E_0} = \left(\sqrt{\pi}\frac{a_0^2}{2}\right)k_pLe^{\frac{-k_p^2L^2}{4}} \tag{2.3}$$

Figure 2.1 shows equation 2.3 plotted as a function of k_pL. A maximum of the plasma wave amplitude can be observed at $k_pL = \sqrt{2}$. For a plasma wave with $v_{ph} \approx c$ this condition becomes $\omega_p\tau = \sqrt{2}$, with τ being the duration over which the pulse is within $1/e$ of its maximum value. This relationship also implies a scaling of the wave amplitude with $I\lambda^2$ for $a_0 \ll 1$.

2.2 Nonlinear plasma waves

At low wave amplitudes $\delta N/N_0 \ll 1$ the density perturbation resembles a sinusoidal form. The associated electric field is given by $\nabla \cdot \boldsymbol{E} = -e\delta n/\epsilon_0$ and is thus also sinusoidal. For larger amplitude plasma waves the electron velocity can vary strongly along the wave as opposed to low amplitude waves, which leads to parts of the wave 'catching up' with another. This can be represented by higher order harmonics of the plasma frequency so that, for a given plasma wave amplitude $\delta N/N_0$ the density perturbation $\delta N(X)$ takes on the form [33]:

$$\delta N(x) = N_0 \sum_{m=1}^{\infty} \frac{m^m}{2^{m-1}m!} \left(\frac{\delta N}{N_0}\right)^m cos(mk_px) \tag{2.4}$$

Equation 2.4 is plotted in Figure 2.2 for a low amplitude wave (a) and high amplitude wave (b). The density for high amplitude wave tends towards a series of sharp spikes, while the electric field tends towards a sawtooth profile. While the underlying physics are different in the one dimensional case, the same sawtooth profile of the electric field is also obtained in the 3D case on the laser axis [2].

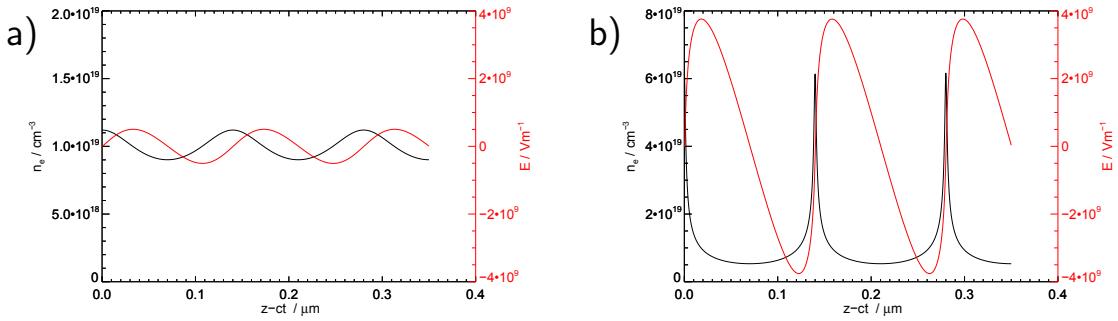

Figure 2.2: The density perturbation and corresponding electric field at a density $N_0 = 1 \times 10^{19}\text{cm}^{-3}$ for $\delta N/N_0 = 0.1$ **a)** and $\delta N/N_0 = 0.7$ **b)**.

2.3 Wavebreaking

As the wave amplitude grows, electrons will eventually reach velocities equal the phase velocity. This effect is often referred to as wavebreaking. Using Poison's equation and assuming the oscillations are harmonic one can derive a maximum electric field associated with this

$$\nabla \cdot \boldsymbol{E} = -\frac{e\left(N_0 - N\right)}{\epsilon_0} \tag{2.5}$$

$$i\boldsymbol{k_p} \cdot \boldsymbol{E_0} = -\frac{eN_0}{\epsilon_0} \tag{2.6}$$

If I assume that the phase velocity approaches the speed of light so that $k_p = \omega_p/c$ is recovered:

$$E_0 = m_e c\omega_p/e \tag{2.7}$$

If relativistic effects are taken into account the cold relativistic wave breaking limit for plasma waves with a relativistic phase factor $\gamma_p > 1$ is

$$E_{WB} = \sqrt{2(\gamma_p - 1)}E_0 \tag{2.8}$$

as shown by Akhiezer and Polovin [34]. The phase velocity of a plasma wave in a homogenous plasma is close to the group velocity of the laser so that $\gamma_p \approx \omega_0/\omega_p$. For underdense plasmas γ_p can be much greater than 1 rendering the wake very robust and allowing for exceedingly high field strength. For example a plasma wave driven by a laser pulse of 800 nm wavelength in a plasma density $1 \times 10^{18} e^{-}\mathrm{cm}^{-3}$ can reach a field strength exceeding 870 GV/m. So far I have only considered homogenous plasmas where electrons oscillate independently after being excited by the driver and thus defined the plasma wavelength, i.e. the distance of the 2π phase of the plasma wave as

$$\lambda_p = \frac{2\pi v_g}{\omega_p} \tag{2.9}$$

where ω_p is a function of the density. If the laser pulse now travels in a plasma gradient towards a lower density, the plasma wavelength becomes larger. This change of distance means, that the phase velocity at a distance 2π behind the driver is changed by change rate $\frac{d\lambda_p}{dt}$. This change rate can be obtained by differentiating equation 2.9 with respect to density giving

$$\frac{\delta\lambda_p}{\delta N} = -\pi c\sqrt{\frac{\epsilon_0 m_e}{e^2}}N^{-\frac{3}{2}}, \tag{2.10}$$

where the $v_g = c$ is assumed and thus higher order terms of N have been neglected. Now the 2π phase moves at a velocity with respect do the driver of

$$v_{2\pi} = \frac{\delta\lambda_p}{\delta N} N' c \tag{2.11}$$

and the phase velocity of the 2π phase is thus $v_{ph2\pi} = v_g r - v_{2\pi}$. Taking the above example and assuming a density down gradient of $N' = 1 \times 10^{17} e^- \mathrm{cm}^{-3}\mathrm{mm}^{-1}$ in laser direction a limit for wavebreaking of $E_{WB} \approx 530\,\mathrm{GV/m}$ is obtained, which is 40% lower than the result obtained above. If one assumes an up gradient, $v_{ph2\pi}$ becomes greater than the speed of light and no wavebreaking can occur.

2.4 Physical effects of wavebreaking

In the last section wavebreaking has been introduced as the limit, when electrons reach the phase velocity and a maximum field was associated with this phenomena. Wavebreaking was first shown as a fact of mathematics, e.g., the nonexistence of a traveling wave solution to the cold fluid equations for amplitudes beyond a limit [34]. It was later shown that the breakdown of the fluid equations is directly due to particle trajectory crossing [35], i.e. sheet crossing. It is worth noting that in the 1D fluid model complete wave steepening and particle trapping occur simultaneously with sheet crossing. Thus experimental papers in the past have used the cold relativistic wavebreaking threshold as an approximation for the accelerating field if electrons were injected [15]. Dawson showed that if transverse oscillations are considered trajectory crossing occurs at arbitrarily small wave amplitudes. For example the aforementioned cavitation behind a laser pulse can not be explained without particle trajectory crossing. If there was a trajectory closer to the laser axis for every given trajectory a bare ion channel could not be formed. This does not necessarily mean that particles are being trapped in the wave, so trajectory crossing and injection become different in multidimensional cases. Still experimental papers are using the term "'wavebreaking"' to describe injection processes [9], which leads to some ambiguity of that term. Up to now there is no analytical solution for 3D plasma waves traveling close to the speed of light. Analytical models can be refined using distribution functions to handle multi flow conditions, but necessary assumptions need to be handled very carefully [36]. However with the growing availability of computational power, detailed particle in cell (PIC) simulations have been performed to investigate high amplitude plasma waves. These simulations, given a high enough resolution, allow for a very detailed insight into plasma effects for a given parameter set. As a single 3D PIC Simulation can take up to several weeks on a computer cluster, wide range parameter scans remain very expensive. Two groups have developed a scalable model for current LWFA experiments based on 3D PIC simulations [2, 37]. In the following I will summarize the model presented by W. Lu *et. al.*.

2.5 LWFA energy scaling

The model by W. Lu *et.al.* gives a scaling law for the so-called blowout regime. The blowout regime is characterized by a cavitated spherical volume behind the driver with a radius $R \approx \sqrt{a_0}/k_p$. Because of the spherical shape this structure is often referred to as the plasma bubble. In order to excite a plasma structure of this kind, the laser focal spot size w_0 must be matched to this sphere.

$$k_p R \simeq k_p w_o = 2\sqrt{a_0} \tag{2.12}$$

This can be reformulated to

$$a_0 \simeq 2\left(\frac{P}{P_c}\right)^{\frac{1}{3}} \tag{2.13}$$

They argue that this condition coincides with the matching condition for optimal self guiding if $P/P_c \geq 8$. For the validity of the model however only $P/P_c \geq 1$ is required, but external guiding may need to be applied to keep the laser from diffracting before optimal acceleration is achieved. It is to be noted that Lu assumes circular polarization. So in order to apply the matching condition one has to use $a_{0,circ} = \sqrt{2}a_{0,lin}$. As explained in section 1.5.1 the front of the laser pulse can not be self guided and will thus etch away with a rate $v_{etch} \simeq c\omega_p^2/\omega_0^2$. This will lead to a depletion of the laser pulse at a distance

$$Ł_{etch} \simeq \frac{c}{v_{etch}} c\tau_{FWHM} \simeq \frac{\omega_0^2}{\omega_p^2} c\tau_{FWHM} \tag{2.14}$$

The phase velocity of the wave can be written as $v_\phi \simeq v_g - v_{etch}$. For a very underdense plasma $\omega_p^2 \ll \omega_0^2$ the phase velocity is thus

$$v_\phi \simeq c\left(1 - \frac{3\omega_p^2}{2\omega_0^2}\right) \tag{2.15}$$

As electrons get trapped and accelerated they approach the speed of light and thus outrun the wave. If the electrons enter the bubble from the back they reach the center of the bubble after a distance (dephasing length)

$$L_{deph} \simeq \frac{c}{c - v_\phi} R \simeq \frac{2}{3}\frac{\omega_0^2}{\omega_p^2} R \tag{2.16}$$

and decelerate after that. Their simulations show a good agreement with the etching velocity approach for $a_0 \geq 2$. Since the bubble is void of electrons the electric field has linear dependence with the distance to the center of the bubble along the propagation direction. This is similar to the result that was obtained in 1D, although for different physical reasons. The peak useful field is obtained as

$$E_{z,max} = \frac{m_e c\omega_p\sqrt{a_0}}{e} \tag{2.17}$$

If the acceleration distance is the dephasing length and electrons are injected at the back of the bubble then the average accelerating field is simply $E_{LW} = E_{z,max}/2$ and the energy gain can be calculated by

$$\Delta E = E_{LW} L_{deph} \simeq \frac{2}{3} mc^2 \frac{\omega_0^2}{\omega_p^2} a_0 \simeq mc^2 \left(\frac{Pe^2}{m^2c^5}\right)^{\frac{1}{3}} \left(\frac{n_c}{n_p}\right)^{\frac{2}{3}} \tag{2.18}$$

This yields a stronger dependence of the energy gain on the density than on the laser power. If the density is reduced for a given laser power, guiding becomes more difficult. For optimal acceleration one wants to assure that dephasing is reached shortly before depletion, leading to the condition that $c\tau_{FWHM} > (2R)/3$. Reaching the dephasing limit means that leading high energy electrons will start decelerating, which effectively compresses the energy spectrum. One can also rewrite the energy gain in practical units and in terms P/P_c as

$$\Delta E\,[GeV] \simeq 3.8 \left(\frac{P}{P_c}\right)^{-\frac{2}{3}} \frac{P\,[TW]}{100} \tag{2.19}$$

The assumptions for this phenomenological model have been verified by PIC simulations and show very good agreement with simulations for $2 \leq a_0 \leq 4$. The model however extends to some degree for lower intensities down to $a_0 \geq 1$. In the model it is assumed that the wave is largely excited by the front of the pulse, while the back of the laser pulse propagates in the ion channel and thus in vacuum condition reducing longitudinal modulation effects. In this scenario Lu assumes that the laser pulse only depletes at the front at approximately the same rate the front of the pulse diffracts. This assumption loses some validity as a_0 is reduced and a larger fraction of the laser pulse can be modulated in the plasma. It is worth noting that also transverse electrical fields have linear dependnce on the distance to the laser axis in the blowout regime, which is beneficial to keep the emittance of the accelerated electron bunch low. The work of Gordienko [37] assumes that the acceleration length is given by the depletion length which as opposed to the assumptions in Lu's model depends on a_0. Thus their energy scaling law has a higher dependence on laser power and reads as follows

$$\Delta E \simeq 0.16 mc^2 \frac{c\tau}{w_0} \left(\frac{Pe^2}{m^2c^5}\right)^{\frac{2}{3}} \left(\frac{n_c}{n_p}\right)^{\frac{1}{3}} \tag{2.20}$$

Gordienko has presented simulations for the parameter range of a_0 between 4 and 10. Most recent experiments however, have been performed at $a_0 \approx 1$. For these intensities the W. Lu model shows a better agreement with experimental results. It is a great success for the field that a simple set of engineering formulas, describing such a complicated process, shows good agreement with experimental result, but they are necessarily an oversimplification. It is common practice that individual experiments are backed up with 3D PIC simulations for their particular parameter set. But the W. Lu model can serve as a guideline to set up new experiments.

2.6 Self injection

In order to summarize self injection I will follow the work done by S. Mangles *et.al.* [9]. The calculation is based on the prediction that self trapping will occur when the radius of the bubble R is larger than a certain value

$$k_p R > 2\sqrt{ln(2\gamma_p^2) - 1} \tag{2.21}$$

stated in [38] with $\gamma_p \approx \sqrt{n_c/(3n_e)}$ [39], that is combined with equation 2.12 and 2.13 in the form

$$k_p R = 2\sqrt{2}\left(\frac{\alpha E}{\tau P_c}\right)^{\frac{1}{3}} \tag{2.22}$$

The factor α represents the fact that only the center of the focal spot will be guided and laser energy in the wings will effectively be lost, thus not contribute to the wake excitation. The necessity of that factor is demonstrated by degrading the focus and comparing the effect on injection with attenuated laser beams. They demonstrated an identical behavior for both cases and I will take that into account in section 5.3. It was thus concluded that a self injection threshold will be reached when

$$\alpha E > \frac{\pi\epsilon_0 m_e^2 c^5}{e^2}\left[ln\left(\frac{2n_c}{3n_e}\right) - 1\right]^3 \frac{n_c}{n_e}\tau(l) \tag{2.23}$$

In their work it is taken into account that the laser pulse modulates and compresses over distance with a certain rate [40]

$$\tau(l) \approx \tau_0 - \frac{n_e l}{2cn_c} \tag{2.24}$$

Thus even if a laser pulse does not initially meet the criteria for injection, it may do so if the plasma is long enough and the laser pulse does not deplete according to equation 2.14. It is notable that neither the focal spot quality nor pulse compression are considered in the W. Lu model. While not considering α the model by Lu*et.al.* may overestimate the electron energy gain, but in other cases pulse compression may lead to an underestimation of the achievable electron energy gain.

2.7 Phase space

An important concept that helps understanding injection is the concept of the phase space that is spanned by a particles impulse and it's position in a potential. In case of a time independent parabolic potential one can start from any point of a phase space diagram, i.e. an initial particle position and impulse, solve the equations of motion and will obtain a closed orbit phase space trajectory. This

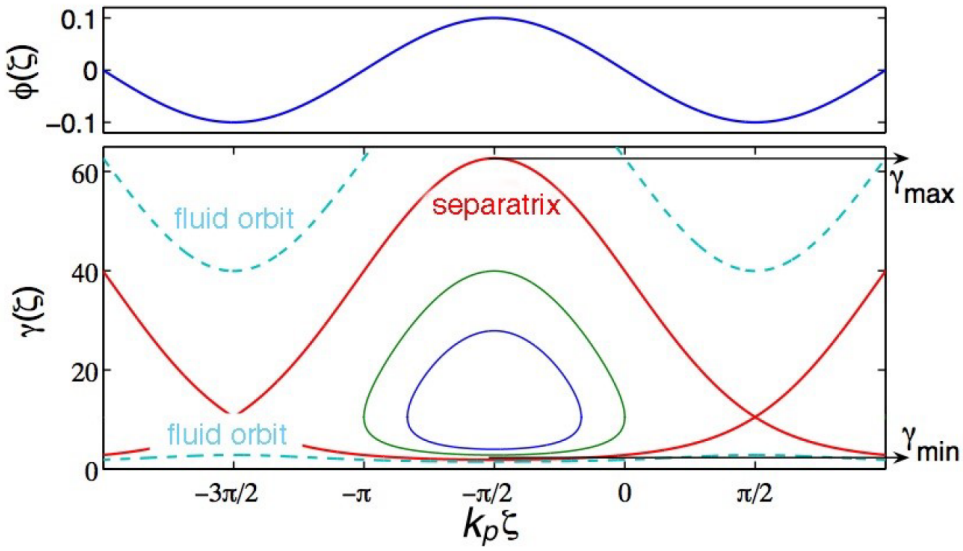

Figure 2.3: Phase space trajectories in a sinusoidal potential from [41]

represents an oscillatory motion as the equations of motion in a parabolic potential yield the harmonic oscillator. This particle would be trapped in the potential and the trajectory represents the sum of potential and kinetic energy. For a time independent potential and linear motion these trajectories of different energies never cross. If I now consider a periodic finite potential like the wake created by the laser pulse, there will be phase space trajectories where particles can cross between the potential wells and escape to infinity. In the context of LWFA these orbits represent the background plasma electrons forming the wake and thus are called fluid orbits. Between the trapped orbits and the fluid orbits is a special trajectory separating the two regimes which is called the separatrix. The above mentioned dephasing limit is represented by the highest impulse value for a given phase space trajectory in longitudinal phase space. Typically the accelerator length is limited to one dephasing length, but one could also accelerate over one and a half dephasing lengths and obtain the same result, if the laser does not deplete or diffract. The full phase space of a particle is necessarily a 6D phase space and in the LWFA scheme particles are also trapped in transverse direction undergoing betatron oscillation. It can be shown [42–44] that the transverse oscillation betatron frequency ω_B is the plasma frequency corrected for relativistic mass gain from longitudinal acceleration.

$$\omega_B = \frac{\omega_p}{\sqrt{2\gamma_e}} \tag{2.25}$$

This transverse oscillation leads to synchrotron radiation comparable to a wiggler and is called betatron radiation. It is also connected to the electron beam divergence as this defines the behavior of the transverse momentum and thus the

divergence. If I assume that the amplitude is given by the offset A_0 as the electron is injected and decreases with $1/\sqrt{\gamma_e}$ as the electron undergoes relativistic mass gain, we can write the oscillation as

$$y = \frac{A_0}{\sqrt{\gamma_e(t)}} \sin\left(\frac{\omega_p}{\sqrt{\gamma_e(t)}} t\right). \tag{2.26}$$

Assuming a constant acceleration gradient g and thus $\gamma(t) = gt$ I can take the derivative of equation 2.26. This derivative is proportional to the divergence angle ϕ_{div} and thus

$$\phi_{div} \propto \frac{\omega_p A_0}{\gamma_e}, \tag{2.27}$$

where the second term in the differentiation can be neglected if $\omega_p \gg g$. If the divergence angle is measured as a function of γ, this oscillation can be directly measured as shown ins section 8.3.1.

2.8 Stimulated injection

As shown in section 2.3 the phase velocity γ_p of the wake reduces if a plasma density down gradient is present and thus the wavebreaking threshold is reduced in equation 2.8. As wavebreaking and self injection are linked phenomena, γ_p also appears in the equations for self injection (equation 2.21). An injection of similar kind than self injection, can thus be stimulated by introducing a localized plasma down gradient. When creating a density transition, the lowest as well as the highest density can be below the threshold for self injection. Only in the gradient is the wakes phase velocity sufficiently reduced to stimulate injection. Experiments by Gonsalves *et.al.* [13] and Hansson *et.al.* [45] have shown down gradient injection by combining different gas sources like a discharge capillary with a gas jet or gas tube with a gas jet. Work done by Schmid*et.al.* [11] and Buck*et.al.* [15] has shown that narrow density transitions can also be introduced by disturbing super sonic gas flows. Another way to stimulate injection below the self injection threshold is to use gases with higher ionization threshold in a mix with a low ionization threshold gas. Barrier suppression ionization, for which the atomic binding potential is suppressed by the laser field, has been discussed in section 1.1. The corresponding laser intensity thresholds are listed in table 1.1. It was found that the 1s electrons of nitrogen have ionization thresholds on the order of the peak intensity of the laser pulse. The helium and remaining nitrogen electrons typically become ionized picoseconds before the peak of the laser pulse is reached. But the 1s electrons of nitrogen have a significantly higher chance to become ionized inside the plasma wake, created by the leading edge of the laser pulse. These electrons have little initial momentum and can then become trapped inside the wake. This method is

called ionization injection. The third option is to collide a second laser pulse with the driving laser pulse [12]. At the moment the pulses superimpose the necessary conditions for injection can be met. One important parameter of the accelerated electrons is the energy spread. It is typically given by the time between the onset and the stop of injection. For self injection and ionization injection energy spreads of a 100% are commonly observed, when the necessary injection criteria are met for the entire acceleration distance. A truncated ionization injection by tailoring the gas mix has been shown by Pollock *et al.* [14] and a truncation due to laser mismatching by Mirzaie*et al.* [46]. Self injection may also produce limited bandwidth, if the laser plasma parameters are adjusted close to the self injection threshold, such that injection truncates as the laser modulates over a certain distance [8]. Colliding pulse injection and gradient injection are intrinsically limited to the density transition or pulse collision location and typically produce electron spectra with limited bandwidth.

2.9 Beamloading

As charge is injected into the wake, the injected charge will also contribute to the wake formation. Electrons in the accelerating phase of the wake will generally reduce the effective accelerating field strength. This has been studied in theory by Tzoufras*et al.* [47], where it was concluded that the accelerating fields are reduced differently throughout an electron bunch of certain length, depending on the charge distribution. Generally this can lead to an increased energy spread of an initially monoenergetic electron bunch. Rechatin*et al.* [48] have demonstrated an experimental observation of this effect, using colliding pulse injection. By tuning the pulse energy of counter propagating pulse, they were able to tune the amount of injected charge at otherwise unchanged acceleration conditions. What they observed was a decrease of electron energy by 15% as they varied the charge from 1 pC to 20 pC. They also observed a proportional increase in energy spread. The method of colliding pulse injection is expected to occur over a very short distance, but in the case of high charge an energy spread of 25% was observed at a peak electron energy of 170 MeV.

2.10 The LWFA design

When designing an experimental setup I have to first decide for an appropriate focal length. The equation 2.12 states a matching condition for density, laser power and intensity. Since the intensity is linked to the laser power by the focal spot size and thus, assuming diffraction limited focal spotsize $w_0 = \frac{4}{\pi}\lambda N_A$, it can be rewritten in terms of the numerical aperture $N_A = f/D$. The numerical aperture is the ratio

of focal length and beam size. This yields

$$\frac{1}{C_m^2}\frac{P^{\frac{1}{3}}}{N^{\frac{2}{3}}} = N_A^2 \tag{2.28}$$

$$C_m = 2 \times 2^{\frac{2}{3}} \sqrt{\frac{e^2}{\epsilon_0 m_e}} \omega_0 \left(\frac{\epsilon_0 m_e \omega_0 P_0}{e}\right)^{\frac{1}{6}} \tag{2.29}$$

so that for a given focal length a certain ratio of $P^{\frac{1}{3}}/N^{\frac{2}{3}}$ satisfies the matching condition. But in equation 2.18 I have stated that the maximum energy gain $E \propto P^{\frac{1}{3}}/N^{\frac{2}{3}}$ and thus the focal length, or numerical aperture respectively, immediately fixes maximum achievable electron energy as plotted in figure 2.4**a)**. This does assume that diffraction of the beam can be avoided , the target length is matched to the dephasing length and the matching condition is satisfied. Increasing the focal length for a given laser power will however cause a lower P/P_c until eventually guiding condition $P/P_c > 8$ as well as $P/P_c > 1$ condition become violated. Thus if the maximum energy gain is to be achieved I may pick a focal length close to the point where matching condition and achievable laser power satisfy $P/P_c > 1$ with some safety margin. Interestingly there is also connection of the second matching condition $c\tau_{FWHM} > (2R)/3$ and the focal length. While the first matching conditions ensures that the Bubble radius R is matched to the spot size w_0, this second condition ensures that the beam is not entirely etched away and thus depleted before electrons can reach dephasing. With the definition of the edge velocity it can be shown that the numerical aperture $N_A \propto L_{deph}/L_{depl}$. This gives an upper limit for the focal length of f =1.2 m (beamsize 0.1 m) if dephasing is to be reached before the laser pump depletes. This limit for the f-number depends only on the pulse duration. If depletion due to the etching effect described by Lu is limiting the energy I still obtain higher electron energies for longer focal length and lower densities. The etching velocity is proportional to the density $v_{etch} \propto N$ and thus also the depletion length will grow. The energy gain due to depletion limitation has the same power dependency as the dephasing limited one and thus it is still only dependent on focal length for the matched case. If I set up an experiment close to $P/P_c = 1$ than we need to expect that we may not reach self injection and the laser may not self focus. In that case the acceleration length is given by the Rayleigh length, which increases quadratically with focal length. But in order to stay matched the density has to be decreased strongly and the acceleration gradient decreases quadratically, which compensates each other. The maximum energy gain thus mostly depends on the weak influence of the laser power P on the acceleration $E_{grad} \propto \sqrt{P}$. The drop in figure 2.4 **b)** below a focal length of 1 m occurs when the dephasing length becomes shorter than the Rayleigh length.

By the time we ordered the parabola we were not aware of Mangles work [9], as the paper only appeared that same year and opted for a 1.5 m focal length parabola. Without the Mangles α it is expected that with fully available laser power we can lower the density to $4 \times 10^{17} e^- \,\mathrm{cm}^{-3}$ without violating $P/P_c > 1$.

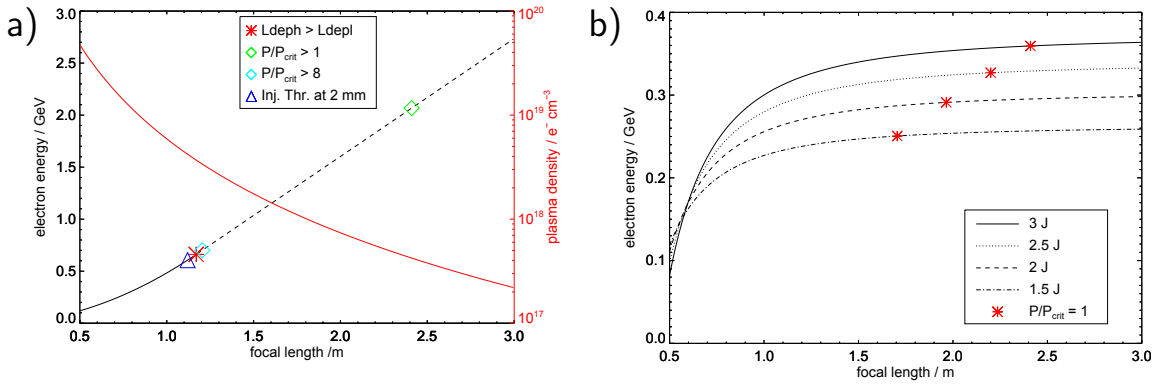

Figure 2.4: Electron peak energy as function of focal length assuming matched conditions for **a)** dephasing and depletion limited acceleration and **b)** for diffraction limited acceleration.

We will show indication (8.2.3) that this limit is $\approx 2 \times 10^{18} e^- \,\mathrm{cm}^{-3}$. Thus we could not achieve matching in the sense of the Lu model at 1.5 m focal length if we apply αE and should have opted for a parabola with focal length of less than 1 m. As it later turned out we achieved good results using a density above $\approx 2 \times 10^{18} e^- \,\mathrm{cm}^{-3}$ and achieved a reasonable match with the Lu model of energy gains using the effective laser energy $E_{eff} = E\alpha$. It is not clear if the Lu model is very insensitive to violations of its proposed matching conditions or whether or not α need to be applied to calculate the density matching condition. Focal spot measurements show that in our experiments typically α =30% of the laser energy is contained within the FWHM. Our above considerations and the plots in figure2.4 assume very strict matching, which may arguably have lead to false conclusions about the choice of the focal length.

Part II

Experiment design

3 General setup and vacuum

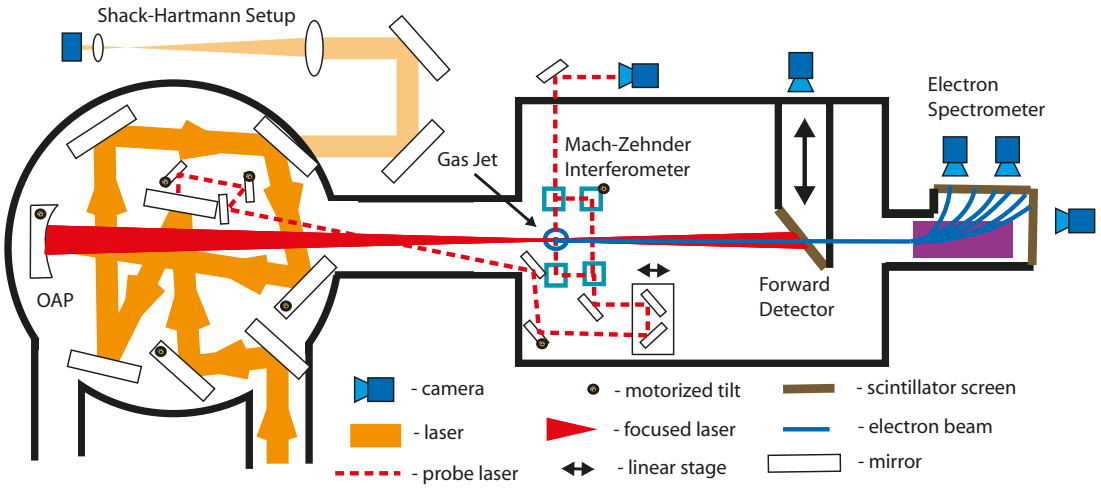

Figure 3.1: Scheme of the LWFA Setup. The gas jet can be linearly adjusted in 3D, but not tilted.

In figure 3.1 the experimental setup in the radiation shielded lab is schematically drawn. The key parameter for the design of the setup is the focal length of the off axis parabola (OAP). It determines the longest distance in the setup, as I have to provide at least 1.5 times that distance in order to safely separate the laser beam and the electron beam after the plasma interaction. In section 2.10 I have reasoned the choice for a 1.5 m focal length. After temporal compression in a grating compressor the laser beam has to be propagated in vacuum to avoid ionization and the formation of an air plasma in the beamline. The round vacuum chamber containing the OAP and the rectangular vacuum chamber containing the gas target were available from previous experiments. The vacuum chamber for the electron spectrometer was specifically designed and build for that purpose. One other important choice was to split off a part of the laser beam (dashed red line in figure 3.1 and 3.2**b)**) for use in an imaging interferometer to diagnose the laser plasma interaction. The necessary delay of the main laser beam causes the rather complicated beam path folded into the first round vacuum chamber. The split off probe beam has a delay stage for fine adjustment added into its beampath. In

addition to the imaging interferometer an additional camera is placed on top of the target chamber, which directly images the gas target. I also added a diagnostic

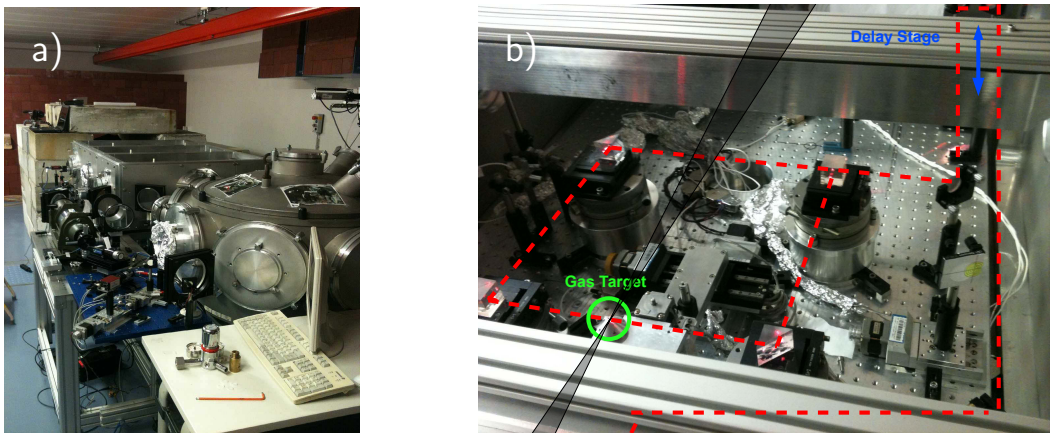

Figure 3.2: **a)** shows the target area with the laser diagnostic table on the left. **b)** shows the inside of the rectangular target chamber with gas target and interferometer. The beam path of the probe beam is shown as dashed line. The main beam is shown in transparent red.

table to study the amplified and compressed laser beam. A particularly large mirror with a special mount to propagate the full beam aperture to outside of the vacuum chamber was used. The full aperture diagnostic table contains a large spherical lens (f=1.1 m) and the focus can be imaged onto a camera with a microscope objective (NA=0.4). Alternatively the beam can be collimated by a 40 mm focal length lens and used to measure the wavefront in a Shack-Hartmann detector (see section 5.3.1). The laser beam can be switched between wavefront and reference focus, but they can not be measured at the same time. The probe beam for interferometry and the full aperture diagnostic beam are split off using the leakage or transmitted light of the main beamline mirrors. On several other mirrors along the beamline leakages are used for laser alignment. The main beam is focused into a second rectangular vacuum chamber with the plasma target surrounded by the interferometer. After a distance of 1 m the beam has diverged enough to be dumped onto an aluminum sheet forming the front of the forward detector. To increase the surface this aluminum sheet is oriented at 45° with respect to the laser. A scintillating screen is mounted on the backside of the aluminum sheet and is imaged with a camera (see section 6.1). The accelerated electrons can penetrate the aluminum sheet and even though scatted the electrons do not loose energy in the 100 µm thick sheet. Thus I was able to measure angular and energy distribution simultaneously at the forward screen and the electron spectrometer. Yet in this mode I can not measure energy dependent angular modulations. The final setup uses 12 Cameras, 40 step motors, a detector for backing pressure and 4 vacuum sensors. In order to operate at typical repetition rates 0.1 Hz, automation is needed to collect the data. For this setup a control system was implemented

using the CS-Framework [49]. For every single shot all motor axis parameters and camera parameters were saved along with the camera images and scalar detector values. The software was also capable to activate the trigger chain leading to a laser plasma interaction. An automated operation was demonstrated, with the system taking hundred shots without user interaction.

3.1 Radiation Safety

As the experiment produces ionizing radiation the experimental area had to be prepared and evaluated according to German radiation safety laws. As part of the thesis a simulation for the expected radiation produced in the setup has been performed. Radiation levels depend linearly on the particle energy as well as on the bunch charge. Thus a full 3D FLUKA [50] simulation has been performed assuming an energy conversion efficiency from laser to electron beam energy of 25% [2]. This theoretical prediction assumes a combination of stimulated injection and guiding. A worst case scenario is assumed, where the accelerated charge is dumped into the yoke of the magnet electron spectrometer. In the simulation it is simplified to an iron block. In this scenario the highest radiation dose outside the target area would occur in the plane of the magnet spectrometer (source of radiation in figure 3.3) and thus additional shielding around the electron spectrometer was required. Figure 3.3 shows radiation levels in the plane of the beam for γ, neutron and proton radiation in top view for this scenario. With the radiation level distribution one can extrapolate the number of shots until the legal threshold could possibly be exceeded. For this I identified the location with the highest levels of radiation outside the shielded area and added the contribution for all radiation types. The extrapolated number of shots till the legal limit is reached was 200.000 shots per year, which is reasonable for the planed experiments in this thesis. For a theoretical 10 Hz operation of 8 hours a workday one could achieve 60 million shots per year and possibly exceed the radiation levels allowed. Thus it was required to implement a hardware counter to ensure, that no more than 200.000 shots of accelerated charge were generated per year. In order to decide which shots are counted towards the shot limit and which shots are considered safe preparation work, a scenario had to be defined in which harmful radiation could be potentially generated. The scenario is the operation of more than two of the main amplifier pump lasers pumping the main crystal and beam line shutters opened, i.e. the laser beam is amplified and focused. In this scenario the personal safety interlock system (PSI) prevents access to the target area and shots passing into the target area are counted. This procedure was favored over adding substantially more shielding to the target area to make it safe for 60 million shots. On the other hand this does prevent any 10 Hz operation with the fully amplified beam, for example for beam diagnostic purposes. Even if the beam was amplified and then attenuated to safe levels, this attenuator needs to be implemented into the PSI system, which I did not do. The performance

of the main amplifier can thus only be diagnosed before compression in the laser grating compressor or in single shot mode, which poses some limitations (5.3.1).

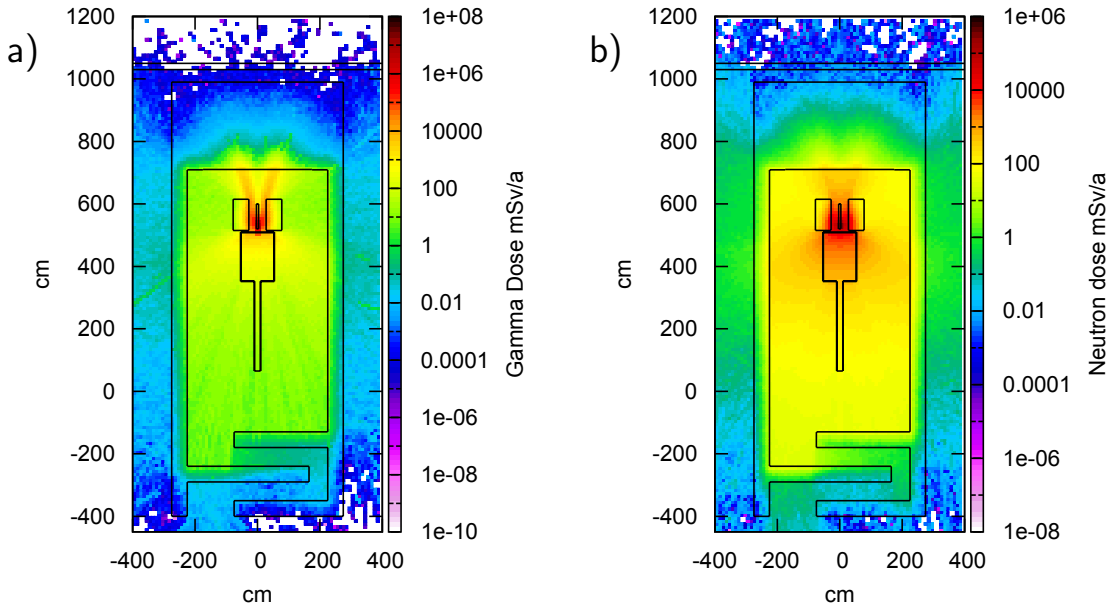
a)
1200
1000
800
600
400
200
0
-200
-400
cm
-400 -200 0 200 400
cm
1e+08
1e+06
10000
100
1
0.01
0.0001
1e-06
1e-08
1e-10
Gamma Dose mSv/a
b)
1200
1000
800
600
400
200
0
-200
-400
cm
-400 -200 0 200 400
cm
1e+06
10000
100
1
0.01
0.0001
1e-06
1e-08
Neutron dose mSv/a

4 Plasma targets and diagnostics

The majority of the experiments have been carried out using supersonic gas nozzles with Helium gas. I will introduce our target design and a calibration that has been performed at the Friedrich Schiller University of Jena. Then a theoretical model for the density and Mach number expected at the exit of such nozzles is presented and compared to the calibration. The theory of shock fronts is introduced and calibration measurements for shock front formation will be presented. I will later demonstrate how electron injection for LWFA can be triggered at the crossing point of the laser and the shock front. At this point I will have discussed the density distribution and will have shown some measured density profiles. These density profile are obtained from interferometric measurements and such an interferometer is also included into my setup. I will discuss the interferometric density measurements in detail on the example of a typical plasma trace, obtained during an electron acceleration experiment.

4.1 DeLaval nozzles

The first design for a convergent-divergent (CD) nozzle followed the recommendations published by Semushin in 2001 [51]. The exit cone expands from a throat with 0.52 mm diameter to its exit diameter of 2 mm over 5 mm length with a cone angle of 17 degrees. The nozzles were manufactured by drilling cones from opposite sites with an arrowhead shaped canon drill in order to achieve the best surface quality inside the cones. Also I noticed, that it is essential to use short-chipping alloys like brass or aluminum alloys with lead content in order to drill a clean cone surface. The nozzle is drilled into a threaded cylinder for easy mounting. This nozzle was calibrated in a jet tomography setup at the Friedrich Schiller University of Jena [52]. The setup is a Mach-Zehnder type interferometer with cubic prisms. The jet is mounted on a rotation stage and interferograms can be measured for different jet orientations. The gas cone above the jet becomes static after a build up time of ≈ 3 ms, following the opening of the pulsed valve. This determines the trigger delay between the pulsed valve and the laser trigger for our experiments.

This build up time is also essential for the repetition rate of our laser plasma ex-

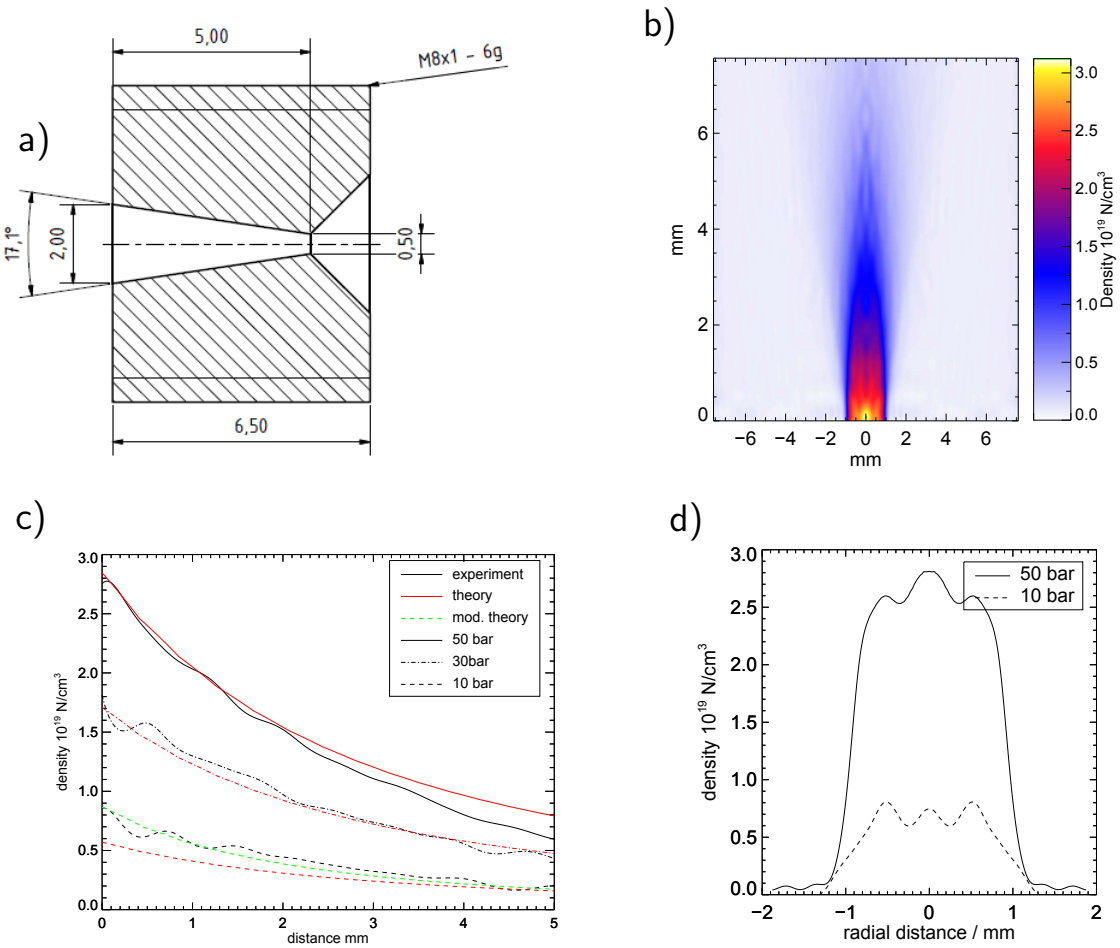

Figure 4.1: a) Drawing of the jet nozzle **b)**. Density profile at 50 bar **c)**. Comparison of averaged density profile (r= ±0.5 mm) over distance from nozzle exit for different backing pressures. For 10 bar an effectively reduced exit diameter of 1.7 mm is assumed to account for boundary layers (green curve) **d)**. Comparison of density profile across the nozzle exit at different backing pressures indicates reduction of exit diameter.

periments. In laser plasma experiments the opening time of the jet must be kept as short as possible. With a 4 ms opening time of the jet pulser the pumps were typically able to restore the vacuum to 10^{-4} mbar within 5 to 10 seconds. When the jet has reached a stable equilibrium one can also use an analytical model to calculate the density (see section 4.2). With a static density distribution I could perform the interferometric measurements with the high quality laser mode of a 633 nm CW Helium Neon laser and exposure times of some microseconds. I was able to obtain a projected map of the phase shift or the density respectively. I will discuss the data analysis of interferograms along with the the interferometer

incorporated into our setup in section 4.4 and a step by step picture gallery of the reconstruction of the gas cone is added in appendix A.2. The gas cone was sufficiently resolved and I could reconstruct the cone density using inverse Abel transformation. However even for a 2 mm path length and using Argon the phase shift became too small to obtain a calibration for backing pressures of significantly less than 10 bar. Figure 4.1 **b)** shows the reconstructed density profile of the jet at 50 bar. At heights of less than 2 mm above the jet the density distribution can be treated as flat top distribution. Above that point the edges of the jet cone start to decay significantly. Although I have measurements from multiple angles, I did not perform a full Inverse Radon transformation. In his publication B. Landgraf *et al.* [52] demonstrated that improved reconstruction of rotationally symmetric distributions is possible if the rotation axis of the tomography stage is precisely located within the images. In [52] it was derived from image analysis tailored to the specific shape of the nozzle. A similar code was not available for our nozzle design and thus an inverse Abel transformation was used, which assumes rotational symmetry. I have evaluated the data from different angles, checked for left-right asymmetries and difference in cone width and found none. I can thus be sure that our target produces rotationally symmetric gas cones. We performed the calibration for three backing pressures and the density at the center of the jet is plotted for different pressures and heights in figure 4.1 **c)**. From a simple 1D theory one expects the density to scale linearly with the backing pressure. We noted that particularly the density at 10 bar is underestimated using linear scaling. The density profile across the jet directly above the nozzle exit is compared for 50 bar and 10 bar in figure 4.1 **d)**. The width of the density profile is narrower for the lower backing pressure. This has also been observed by K. Schmid [53] and his proposed corrections to the 1D model of gas flow, will be discussed after introducing the 1D model in the next section. A list of all manufactured nozzle designs is listed in table 4.1. The diameters have been measured with a microscope and the throat was typically 20 µm wider than the corresponding nominal width of the drill used to drill the throat prior to the shaping with the canon drill. In this thesis only results from type I and II are presented.

Type	Throat	Exit	Length	Mach # (exit)	Density (exit 10 bar)
I	0.52 mm	2.0 mm	5 mm	5.9	$11.0 \times 10^{18} e^- cm^{-3}$
II	0.27 mm	2.0 mm	5 mm	9.4	$2.9 \times 10^{18} e^- cm^{-3}$
III	0.27 mm	3.0 mm	5 mm	12.4	$1.3 \times 10^{18} e^- cm^{-3}$
IV	0.52 mm	5.0 mm	7 mm	11.2	$1.5 \times 10^{18} e^- cm^{-3}$

Table 4.1: List of manufactured nozzle types. The density is calculated for 10 bar backing pressure Helium, assuming double ionization, at the nozzle exit for nominal diameter (for effective diameter see section 4.2).

4.2 1D model of CD-nozzles and boundary layer effect

In the following section I will follow the work of K. Schmid [54]. It can be shown that in an equilibrium state the gas velocity at the nozzle throat must be the maximum velocity that small perturbations can travel within a gas. This velocity is the well known speed of sound c_s, which for the perfect gas evaluates to

$$c_s = \sqrt{\kappa \frac{R}{m} T} = \sqrt{c_p (k-1) T} \tag{4.1}$$

with the gas constant $R = 8314.46\,\mathrm{J/(kg\,K)}$, the temperature T and the specific heat for constant pressure c_p. The specific heat ratio κ between specific heat for constant pressure c_p and specific heat for constant volume c_v provides a connection between thermodynamics and kinetic gas theory

$$\kappa = \frac{c_p}{c_v} = \frac{2 + f_d}{f_d}, \tag{4.2}$$

with f_d corresponding to the number of degrees of freedom of the molecules constituting the medium. Possible values for f_d are 3 for atoms, 5 for molecules containing 2 atoms and 7 for molecules containing 3 or more atoms. Schmid states that 1D flow theory is a sufficient description for rotational symmetric micro jets. I need to introduce the flow cross section f and the flow velocity w. Of course the total mass flow $\dot{m} = \rho w f$ with the density ρ has to be constant throughout the flow as long as no sources or sinks are present. For the flow in a 1D system following equation can be derived

$$\left(1 - M^2\right) \frac{1}{w} \frac{dw}{dx} = \frac{1}{\rho w} \frac{d\left(\rho w\right)}{dx} = -\frac{1}{f} \frac{df}{dx} \tag{4.3}$$

with Mach number $M = w/c$ being the ratio between the flow velocity and the local speed of sound. Equation 4.3 thus states that the flow velocity increases with decreasing cross section for subsonic gas flows, but grows with growing cross section for supersonic flows ($M > 1$). This effect is exploited in convergent-divergent nozzles (CD-nozzles), where $M = 1$ is reached in the throat. For a reservoir initially at rest it is possible to relate the reservoir conditions (index 0) to the conditions at the throat (index t) by using the fact that, $M = 1$ in the throat and

applying the isentropic equations.

$$w_t = \sqrt{\frac{\kappa-1}{\kappa+1} 2 c_p T_0} = c_{s0} \sqrt{\frac{2}{\kappa+1}} \tag{4.4}$$

$$\frac{p_t}{p_0} = \left(\frac{2}{\kappa+1}\right)^{\frac{\kappa}{\kappa-1}} \tag{4.5}$$

$$\frac{\rho_t}{\rho_0} = \left(\frac{2}{\kappa+1}\right)^{\frac{1}{\kappa-1}} \tag{4.6}$$

$$\frac{T_t}{T_0} = \frac{2}{\kappa+1} \tag{4.7}$$

$$\frac{\rho_t w_t}{\rho_0 c_{s0}} = \left(\frac{2}{\kappa+1}\right)^{\frac{\kappa+1}{2(\kappa-1)}} \tag{4.8}$$

c_{s0} is the speed of sound in the reservoir. With all these quantities fixed the mass flow in the throat can be obtained.

$$\dot{m}_t = f_t \left(\frac{2}{\kappa+1}\right)^{\frac{\kappa+1}{2(\kappa-1)}} p_0 c_s 0 \tag{4.9}$$

and also one can get a relation for the Mach number in the entire flow domain

$$\frac{f_t}{f} = \frac{\rho w}{\rho_t w_t} = M \left[1 + \frac{\kappa-1}{\kappa+1}\left(M^2-1\right)\right]^{-\frac{\kappa+1}{2(\kappa-1)}} \tag{4.10}$$

The Mach number only depends on the diameter ratio, gas type via f_d. This is an important prediction in order to calibrate the gas nozzles, as the distribution of density in the gas cone depends on the Mach number only. Thus the 'shape' of the gas cone remains constant for different backing pressures and different monoatomic gases. Thus I can use Argon at high backing pressure to calibrate our gas nozzles. It may be noted that equation 4.10 can not be solved analytically for M. But in order to use the preservation of mass flow and the known mass flow in the throat to calculate all quantities throughout the entire flow regime, the flow speed in equation 4.10 is needed. Thus equation 4.10 needs to be solved numerically first. The density depends linearly on the density in the reservoir, but also depends on the reservoir temperature because $w_t \propto \sqrt{T}$ in equation 4.4. For the evolution of the unconstrained flow above the nozzle exit Malka et al. [51] states that the opening angle of the gas cone θ only depends on the Mach number at nozzle exit.

$$sin(\theta) = 1/M. \tag{4.11}$$

For a certain distance above the nozzle exit, one can use the cone diameter analogical to the diameter in the constraint flow. In figure 4.1 **c)** the theoretical predictions for the different backing pressures are plotted in red. This assumption gives a reasonable agreement up to 2 mm above the jet, where the density can be considered a

flat top profile with sharp edges. Above that the softening of the jet edges starts to affect the density even at the center of the jet. For lower pressures the theoretical model underestimates the density even at the nozzle exit. According to Schmid et al [53] this can be explained by the presence of boundary layers. A boundary layer is layer of gas close to the nozzle walls with a subsonic velocity. The core flow behaves according to the equations above, but with an effectively reduced diameter f_{eff} by the thickness of the boundary layer. The boundary layer grows with the length of the nozzle, larger opening angles and lower backing pressures. Schmid has calculated boundary layers for several backing pressures and nozzle geometries and concluded a scaling for these boundary layers with $d_{thr}p_{back}$ for the backing pressure and severely altered exit diameters for values smaller than 10 mm bar. The measured density profile at 10 bar shows a good agreement with the 1D theory assuming an effective exit diameter of $f_{eff} = 1.7$ mm (green curve) and with the measured profile width at exit 4.1 b). The 1D model can predict the plasma density with good accuracy for heights below 2 mm and backing pressures above 10 bar. For a height of 1.5 mm, 10 bar backing pressure and an effective exit diameter of 1.7 mm this model yields a density of $8.5 \times 10^{18} e^- cm^{-3}$. I have later found that the optimal density for our experiments is in the range of $1 - 5 \times 10^{18} e^- cm^{-3}$. If a lower density flat top profile needs to be created, while avoiding boundary layer effects, a different throat to exit diameter ratio is required. The throat diameter can not be made significantly smaller, because of limitations from the manufacturing. A nozzle with a 0.27 mm throat to a 2 mm exit also exhibited boundary layer effects at higher backing pressures. Thus one has to increase the exit diameter, creating a longer plasma interaction length. In either case will an increased throat to exit diameter ratio increase the Mach number. For the purpose of creating a density distribution for LWFA the Mach number is not an important parameter. However if shock fronts are created the Mach number determines the density ratio in the shock front. Shock fronts are discussed more in detail in the next section 4.3. If a combination of low density and low Mach number is to be achieved close to the nozzle exit, than boundary layers are hard to avoid. The presence of boundary layers reduces the effective throat to exit diameter ratio and thus decreases the Mach number even further. The lower Mach number on the other hand causes a stronger deviation from a flat top profile. Working in a regime with significant boundary layers requires direct density measurements during the LWFA experiment or a numerical simulation in two dimensions for rotationally symmetric nozzles or three dimensions for arbitrary nozzle shapes.

4.3 Shocks in supersonic gas flows

In a gas flow small perturbations can only travel through the gas with a maximum velocity equal to the speed of sound. This does not apply to very strong perturbations, which can travel at speeds much larger than the speed of sound. If

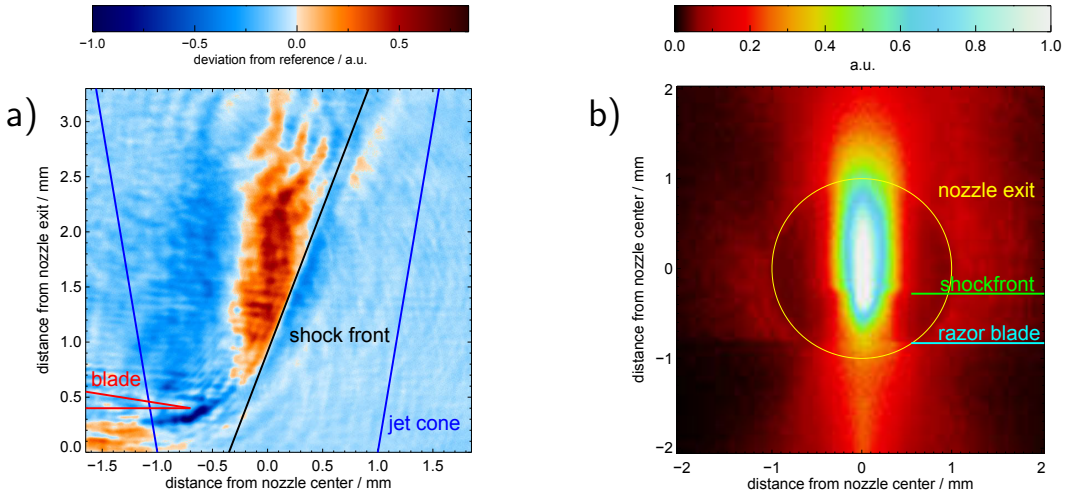

Figure 4.2: **a)**Image of the shock front in Argon using flat phase interferometry from the side 4.11. **b)** Shockfront in plasma trace viewed from top.

a supersonic flow encounters an obstacle the flow upstream of the obstacle has to adapt. That implies that a perturbation has to adapt upstream a super sonic flow, which means it has to propagate at a speed higher than the speed of sound. Since a small perturbation can not do this, this condition enforces a strong perturbation to form in the steady state, which is called a shock front. Such a shock front can for example be formed by disturbing the flow of a supersonic CD nozzle with a sharp razor blade (figure 4.2). Gas flow at such a shock front is compressed and the flow velocity is forced to a subsonic velocity within the order of a few times the mean free path. The change of state from before to after the shock is given by the following set of equations

$$\frac{w_2}{w_1} = \frac{\rho_1}{\rho_2} = 1 - \frac{2}{\kappa+1}\left(1 - \frac{1}{M^2}\right) \tag{4.12}$$

$$\frac{p_2}{p_1} = 1 + \frac{2\kappa}{\kappa+1}\left(M^2 - 1\right) \tag{4.13}$$

$$\frac{T_2}{T_1} = \frac{c_2^2}{c_1^2} = \frac{1}{M^2}\left[1 + \frac{2\kappa}{\kappa+1}\left(M^2-1\right)\right]\left[1 + \frac{\kappa-1}{\kappa+1}\left(M^2-1\right)\right] \tag{4.14}$$

$$M_2^2 = \frac{1 + \frac{\kappa-1}{\kappa+1}\left(M^2-1\right)}{1 + \frac{2\kappa}{\kappa+1}\left(M^2-1\right)} \tag{4.15}$$

In figure 4.2 shock fronts are shown that are not perpendicular to the gas flow. Schmid suggested that the above formulas are applicable if one uses a modified

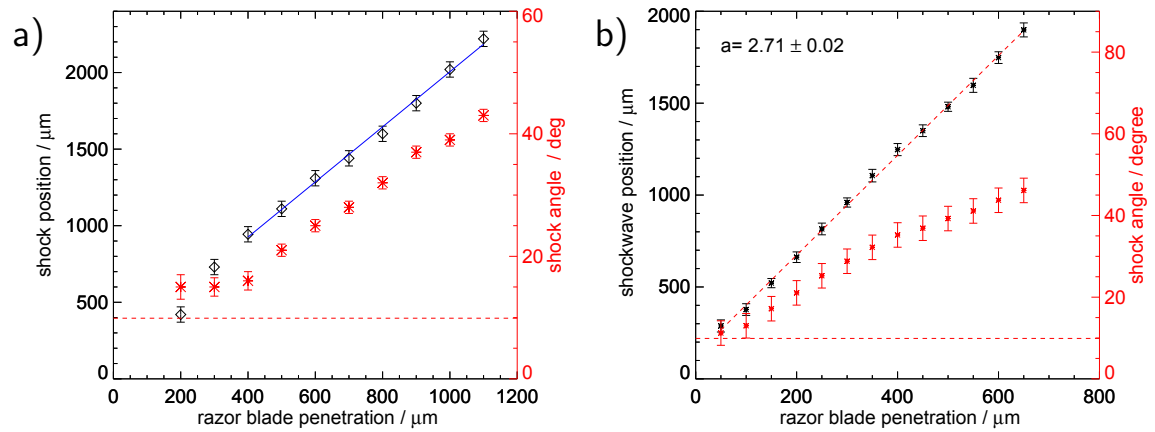

Figure 4.3: Longitudinal Shock position at 1.2 mm above the nozzle and shock angle as function of razor blade penetration depth as measured from **a)** Argon flat phase interferometry and **b)** with top view plasma trace. Dashed line shows the minimum angle for this nozzle.

Mach number by taking the angle ϕ_M between the flow and the shock and use $M_\phi = M \sin \phi_M$ with M being the Mach number of the flow on the super sonic side of the shock front. The modified M_ϕ can not be smaller than 1, because a shock is necessarily a super sonic ($M > 1$) phenomena. This implies that there must be a minimum angle at a which the shock front can form in the flow given by $\phi_{min} = \sin^{-1}(1/M)$. The shock front is typically observed as discontinuity in our plasma observations as shown in figure 4.2 (b). A full picture of the shock front formation is revealed in Argon at high backing pressure 4.2 (a). The measurement was done in our setup with parallel interferometer beams. In this case phase offsets appear darker (more red) or brighter (more blue) with respect to a reference image. This method has a better spatial resolution, than the method introduced in the next section 4.4. This helps to recover the shock angle and shock position. However it can not be used to quantify the density distribution. Figure 4.3 shows the dependence of shock angle and position with respect to razor blade penetration depth. It shows that with increasing penetration depth the shock angle increases linearly. At less than 400 µm the shock front seems to build up as the shock angle 1 mm above the blade is approximately the theoretical minimum angle. For this nozzle with an exit Mach number of $M = 5.9$ the theoretical value is $\phi_{min} = 9.9°$ (dashed line). As the shock angle grows linearly with penetration depth the shock position at 1.2 mm above the exit changes by (1.62 ± 0.05) µm for every micrometer the razor blade is moved. This method does only show the behavior with Argon at high backing pressures. With the direct imaging system I was able to observe a feature in the plasma trace, that represents the shock front as seen in figure 4.2 **b)**. The jet is set up with the typical experimental condition of 8 bar backing

pressure and a plasma trace is created with the preamplified laser 1.2 mm above the nozzle. This method can't show the curvature of the shock front and the angle must be estimated assuming a straight line from razor blade to the observed feature. However this method resembles the experimental condition used in LWFA experiments more closely. The ratio for razor blade and shock front position is 2.71 ± 0.02 in this case. I was only able to resolve the location of the shock front, but can't provide any measurements for the density after and before the shock front, due to low signal to noise ratio in my interferometer. For little penetration depth I may still apply our model and use the equations above to calculate the transition ratio. For larger razor penetrations the nozzle exit will be blocked enough to significantly change the entire gas cone. The razor blade also breaks the rotational symmetry and a full 3D simulation is required in order to predict the density. Because the shock front is very narrow, a high spatial resolution of this simulation is needed as well, making these simulations numerically expensive.

4.4 Target diagnostic and interferometry

The density of the plasma is the most crucial experimental parameter for LWFA experiments. As I have shown in section 4.2 and section 4.1 this density can in some cases be hard to predict from flow models. For plasma and gas the index of refraction is a function of the respective density. This gives the opportunity to measure the phase shift of laser light passing through the target and thus determine the gas density from the measured index of refraction. The phase shift can be measured using interferometry and I will discuss some basics of data analysis for interferometric data along with the specifics of our setup. The first problem is that helium at a density of $1 \times 10^{18}\,\mathrm{cm}^{-3}$ does not have an index of refraction noticeably different from the vacuum index of refraction $n_{vac} = 1$. In order to measure the full target density distribution I have to use Argon at high density (high backing pressure) and scale the results down to actually used backing pressure in the experiment as it has been discussed in section 4.1. During an experiment a plasma is produced and close to the focus one can assume it is fully ionized. The plasma index of refraction deviates strongly from the vacuum index of refraction and a phase shift is easily detectable even for low densities and short path length, i.e. small plasma structures. As the surrounding helium does barely contribute to the phase shift I can detect the trace of the laser pulse in the plasma with our interferometer setup. Our interferometer uses a Mach-Zehnder type layout with cubic prism splitter and combiner placed inside the vacuum chamber. On the two remaining corners of the rectangular interferometer setup I have used two 90 degree prisms (see figure 3.2 **b)**). Using the back reflections from the prism faces, the four prisms can be prealigned into a perfect rectangle. The combined beams are then imaged onto a camera with a telescope consisting of an aspherical lens (f= 10 cm) and a microscope objective (f= 8 mm). The delay stage of the

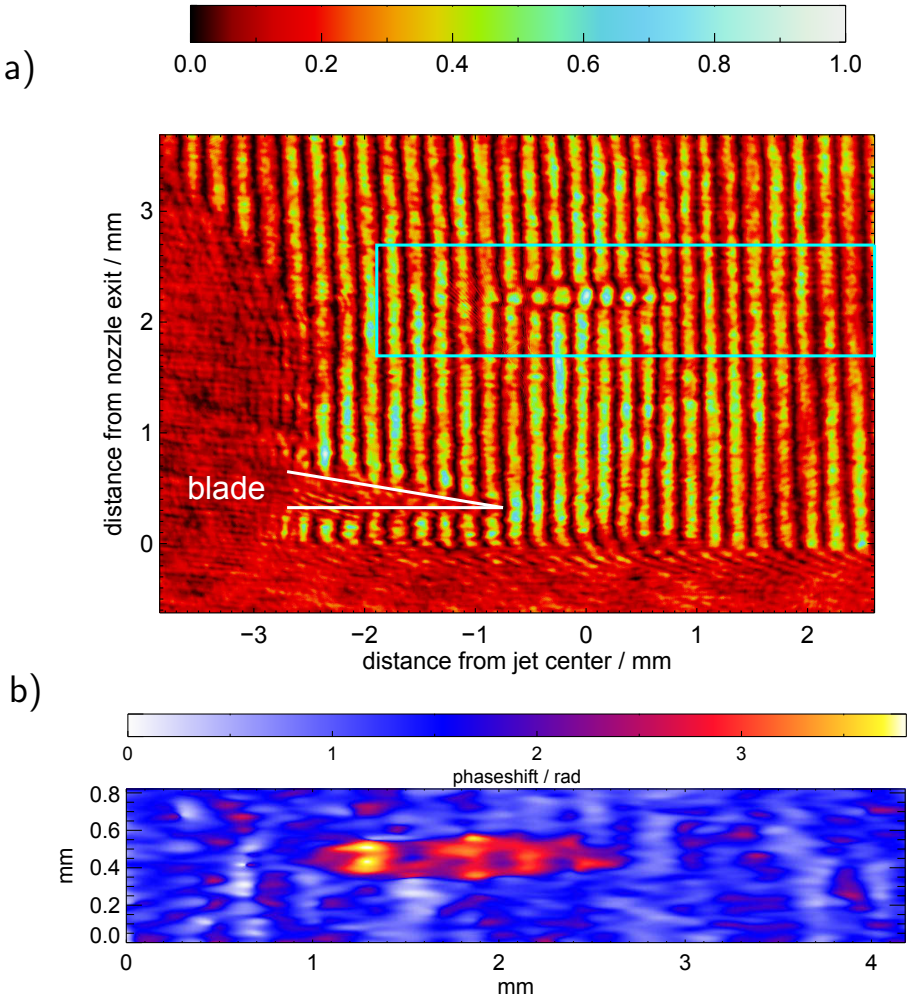

Figure 4.4: a) Interferometer image of a type I target at 5 bar backing pressure with plasma trace in side view. Laser passes from left to right. Razor blade is visible in the lower left corner. **b)** shows the phase shift obtained from the area in the blue box.

probe beam is set so that the probe beam passes the plasma interaction a few 10 picoseconds after the main laser pulse has passed. Significant changes of the plasma trace have not been observed until a few hundred picoseconds later. A typical interferometer image is shown in figure 4.4 **a)**. In the part of the image with the characteristic fringe pattern the path of the probe beam is not obstructed and the modulated fringe pattern in the blue box represents the plasma trace caused by the laser. The obstruction in the lower part of the image represents the edge of the nozzle and on the left side the mounting block for the razor blade. The blade itself is visible in the lower left corner. The laser passes from the left to the right. The mounting block has an opening for the laser, which is not visible in this

perspective. Halfway in the plasma trace a disturbance from a shock front may be identified by a skilled observer. It is significantly easier to observe small plasma structures if instead of a fringe pattern the 2 interferometer beams are aligned perfectly parallel as shown in figure 4.5 **b)**. In the second picture a very similar scenario is shown. Although localization of plasma features is easier in the second case, it does not contain quantifiable information about plasma properties. As the measurement beam in the interferometer gets phase shifted the signal will vary between constructive (bright) and destructive (dark) interference. However as the maximum and minimum phase shift are not quantified the phase shift can not be quantified either. Primitively this is the reason, why one introduces a phase shift by tilting the two interferometer beams with respect to each other. The separation of two maxima $\Delta_{2\pi}$ is a 2π phase difference related to the tilt angle ϵ by

$$\epsilon = \frac{\lambda}{\Delta_{2\pi}} \tag{4.16}$$

Furthermore as the interference is changed with respect to the surrounding, the fringe patterns starts to bulge. If such a bulge in a fringe reaches a size of the distance between two fringes, it represent a phase shift by 2π. The phase shifts are thus modulated into a periodic pattern and the density reconstruction is done in 4 steps:

- **Fourier Filter:** A Fourier transform of the image yields a distinct signal in Fourier space at the frequency of the fringe pattern, with all modulations of the fringe pattern encoded as Fourier coefficients close to the fringe frequency. I can filter out all coefficients close to this carrier frequency and back transform. The result is complex number and because of the polar form of complex numbers

  $$z = r \exp i\phi \tag{4.17}$$

  I can extract only the phase term of the result and immediately retrieve the phase angle of the carrier frequency, which can be shown to be the phase shift introduced by the tilt of the interferometer beams plus the phase shift from the medium.

- **Unwrap:** The next step in the analysis can be very difficult for laser plasma traces at high densities. The phase shift is still encoded in a periodic pattern as the phase is only obtain as modulo 2π. This means that all phase differences between neighboring pixels close to 2π need to be stitched together. There are powerful algorithms available and I have used an algorithm called "residue unwrapper" [55] for this task. The problem is when phase shifts introduced by the medium cause phase differences by more than 2π seen when the fringe pattern is not only bulged but broken. For our setup this happens frequently at densities above $1 \times 10^{19} e^{-} cm^{-3}$ for the analysis of laser plasma

traces. A higher resolution can help with this problem, but typically comes at the expense of a smaller field of view.

- **Plain:** The next step is to get rid of the phase shift that was introduced with the tilt angle (see appendix figure A.2 **d)**). The background can viewed as a tilted plane in direction of the beam tilt angle. The most simple approach is to take a reference image without the signal, run the steps above and subtract the reference from the measurement. However the angle might change slightly introducing a linear background signal by 1π across the image in arbitrary directions. I thus fit the background and extrapolate it into the part of the image with the measurement. At this point a map of the phase shift is reconstructed from the raw image as shown for the laser plasma trace in figure 4.4 **b)**.

- **3D reconstruction:** This image however is only a projection of the index of refraction as the phase shift is accumulated over the beam path. In order to retrieve the density one needs the phase shift per distance. A full tomographic reconstruction via inverse Radon transformation requires measurements from different viewing angles and precise localization of the rotation axis. For rotationally symmetric structures the reconstruction may be done from a single image using the Inverse Abel transformation. In the case shown above the plasma trace is on average 36 ± 4 pixels wide ($180 \pm 20\,\mu$m). the noise has a standard deviation of 0.1π, while the background corrected signal is 0.4π. In this case I have too little resolution and signal to noise ratio in order to meaningfully perform an Abel Inversion. I may simply divide the mean phase shift by the width of the plasma trace and obtain a phase shift of $\phi = (6.5 \pm 1)$ rad per mm. With the index of refraction $\eta = 1 - \phi\lambda_{laser}/(2\pi)$ and the laser wavelength I can use equation 1.13 and equation 1.15 to obtain the density as

$$N = \frac{e^2}{(2\pi c)^2 \epsilon_0 m_{el}} \frac{1 - \eta_{pl}^2}{\lambda_{laser}^2} \tag{4.18}$$

  Thus a plasma density of $(2.8 \pm 0.4) \times 10^{18} e^- cm^{-3}$ is obtained. I have also performed reconstruction of interferometric data for the calibration of our nozzles in section 4.1. In that case the resolution was good enough to perform the inverse Abel transformation. A gallery of a step by step gas jet reconstruction is shown and discussed in appendix A.2 including an image in Fourier space, back transformed filtered image and a visualization of the tilted background.

The model yields a plasma density $2.8 \times 10^{18} e^- cm^{-3}$ for a 2 mm exit diameter and a density of $3.2 \times 10^{18} e^- cm^{-3}$ for an effectively reduced exit diameter to 1.7 mm. Given the uncertainty in the size of the effective exit diameter and the decay

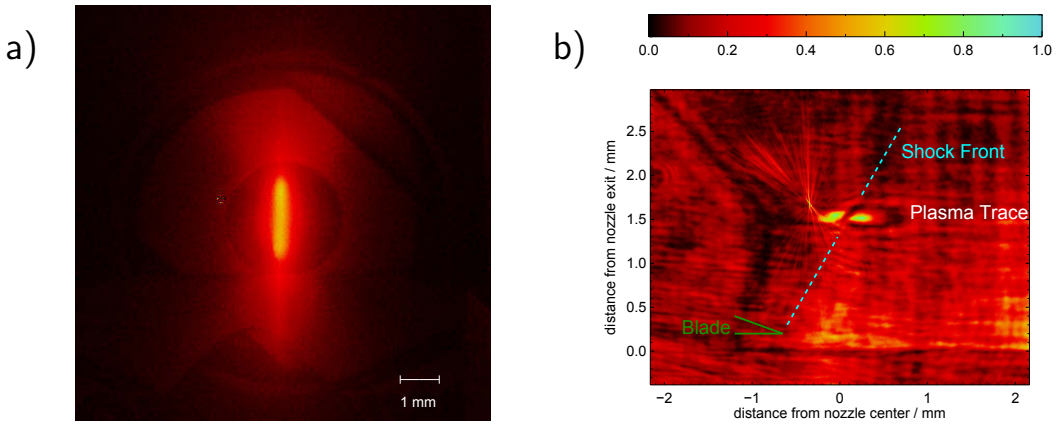

Figure 4.5: a) Laser plasma trace directly imaged from top. Laser is attenuated. **b)** Interferometer image with parallel beams (no fringes). The shown scenario is similar to figure 4.4. Shock front is clearly visible.

of the flat top distribution the model and the measurement show a reasonable agreement. In both cases the density distribution along the beam path could not be resolved and the average plasma density can be determined with an accuracy of $\pm 0.5 \times 10^{18} e^{-} cm^{-3}$. One possible improvement could be a further magnification and improved optical resolution of the plasma trace. However, this would shrink the field of view. I could use the setup to measure the distance of the plasma trace from the nozzle exit with reasonable accuracy. Furthermore to maintain the distance of fringes in the image, I would have to increase the tilt angle even more, which was already limited with the given setup. Despite the low resolution for density measurements, the interferometer was very valuable to locate the position of the plasma trace. With the direct imaging system, viewing the target from the top, it was very difficult to get a good imaging of plasma features at full laser power, due to strong scattering of laser light. I typically aligned the laser in top view with an attenuated beam prior to the experiment as shown in figure 4.5**a)**. With a fully amplified laser beam, the imaging interferometer delivered the better results in order to localize plasma features. It has also helped to identify laser prepulses or misaligned foci, which caused characteristic deformations of the plasma trace.

5 The laser system and diagnostics

The necessary technology to amplify laser beams is sufficiently covered in literature and thus only one particular aspect shall be covered in this thesis. In order to safely reach an electrical field strength many orders of magnitude higher than the dielectric strength of vacuum, one makes use of the fact that a laser pulse can be stretched and compressed temporally and spatially. The laser pulse is typically stretched before the amplification to keep the intensity below the damage threshold of the optical components. It only gets fully compressed at the position of the interaction and the theoretical limit of this compression will be the topic of section 5.2 for the time domain and of section 5.3 for the transverse spatial domain. The lowest order of spectral spatial effects will be discussed in section 5.4. The following section 5.1 will list the necessary keywords to distinctively identify the laser system used in the presented thesis.

5.1 Amplitude Pulsar System at MBI

The laser system at Max Born Institute is Double Chirped Pulse Amplification (DCPA) system based on titanium sapphire (Ti:Sa) amplifiers. A front end system with a Kerr-lens mode locked (KLM) Oscillator, a Booster Amplifier and a cross wave polarizer (XPW) setup provides a seed pulse for two amplifier chains. For the experiments in this thesis I have used the amplifier chain commercially bought from Amplitude Technologies. This chain consists of one regenerative amplifier and three multipath amplifiers. A schematic overview is shown in figure 5.1. Worth mentioning is the Dazzler and the Mazzler built into the regenerative amplifier to prevent gain narrowing [56] 5.2 **a)** and to control the spectral phase. The Ti:Sa crystal of the last or main amplifier is housed in a cryostat, to avoid thermal lensing in the crystal. With the main amplifier running, the focused laser beam could potentially produce ionizing radiation. Thus the pump lasers are controlled by the PSI 3.1 and require the beam line shutters to be closed or radiation interlock to be activated. For calibration or preparation I typically operated the laser system without the pump lasers of the main amplifier being activated.

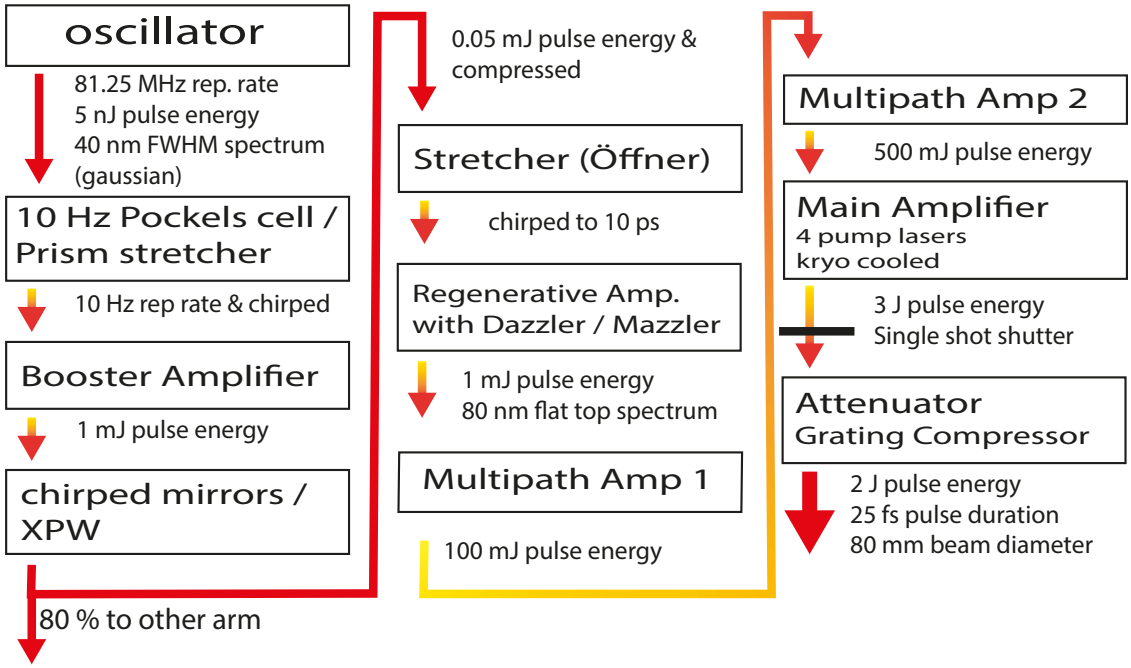

Figure 5.1: Schematical overview of the laser chain.

5.2 Temporal compression and transform limit

The plain wave is the most simple solution of the Maxwell equations and the wave equation. The Fourier theorem tells us, that arbitrary functions can be described as infinite sum of sine and cosine functions. Furthermore the Fourier transform allows us to calculate the relative amplitudes of the sine and cosine $I(\omega)$ needed to obtain the desired temporal function $I(t)$.

$$I(\omega) = (\mathfrak{F}\{I(t)^{1/2}\})^2 \tag{5.1}$$

A very simple function to transform is the Gaussian function. The result of the Fourier transform of a Gaussian function with a FWHM σ is simply another Gaussian function with an FWHM of $\sigma_T = \frac{C}{\sigma}$. Thus the product of the spectral width and the shortest pulse duration is a constant called the time bandwidth product. For the product of the FWHM of a Gaussian and the FWHM of its respective Fourier transform this value is 0.44. For other analytical functions similar products can be found using their FWHM and FWHM in Fourier space. For a flat top spectrum this product is 0.89 and 0.22 for a Lorentzian distribution. Equation 5.1 ignores the spectral phase due to the square, but it is only valid for frequency independent spectral phases. The change of phase with respect to the frequency is called the group delay T_g. Optical elements can introduce a change of T_g which is

called the group delay dispersion (GDD)

$$T_g = \frac{\partial \varphi}{\partial \omega} \qquad GDD = \frac{\partial T_g}{\partial \omega} = \frac{\partial^2 \varphi}{\partial \omega^2} \tag{5.2}$$

It is sometimes referred to as second order dispersion and usually specified in fs^2. For example the window used to extract the beam from the compressor to our diagnostic setup introduces a GDD of $700 fs^2$ due to its dispersion relation. The direct temporal intensity distribution measured with autocorrelator highly depends on the actual pulse shape and different pulse shapes can lead to similar autocorrelator traces. Thus when one measures the pulse duration, the spectral phase distribution and the spectral intensity distribution is measured and $E(t)$ is reconstructed [57]. Reaching the shortest pulse duration, being transform limited and the pulse having a frequency independent phase are synonymous statements. In order to achieve highest intensity in the focus, one has to achieve the shortest pulse. In order to reach the transform limit we control the spectral intensity using a Mazzler [56] and spectral phase up to higher orders using a Dazzler [58]. A flat top spectral intensity profile with a FWHM width of 80 nm centered around 810 nm 5.2 is obtained. This corresponds to a frequency width of 3.75×10^{13} Hz and using the time bandwidth product for flat top distributions we obtain transform limited pulse duration of 23.7 fs. The pulse duration is measured on a daily base with typically nearly transform limited pulse duration of 25 fs. But we also observed a slow drift of approximately 800 fs^2 from morning till evening. A deviation from the optimum pulse duration was also directly observed from a plasma based observation, which gave me a chance to compensate any drifts without an autocorrelator measurement (see section 7.4). In section 1.1 I have shown that barrier suppression ionization sets in at a laser intensity of $10^{14} - 10^{16}\,\mathrm{W\,cm^{-2}}$. This intensity is reached a few picoseconds before the peak of the pulse as seen from figure 5.2 **b)**, which is order of magnitudes before the onset of wake formation. However the ASE level preceding the peak pulse by several nanoseconds should not exceed this limit as typical sonic speeds are in the order of micrometer per nanosecond and too early ionization would cause ion displacement. This gives a minimum laser contrast of better then 10^{-5} as we are focusing the laser pulse to peak intensities of $2 \times 10^{18}\,\mathrm{W\,cm^{-2}}$. High ASE contrast has been an important parameter for overdense laser plasma interaction experiments at MBI and the XPW front end ensures contrast of better than 10^{-8}.

5.3 Focussing or spatial compression

In Fourier optics, focusing can be described with the same mathematics introduced in the previous chapter extended into 2 dimensions. The diffraction pattern $F(x, y)$ of an aperture $f(x, y)$ at a distance is given by the Fresnel-Kirchhoff diffraction equation. Our limited beam profile can be viewed as an aperture applied to an

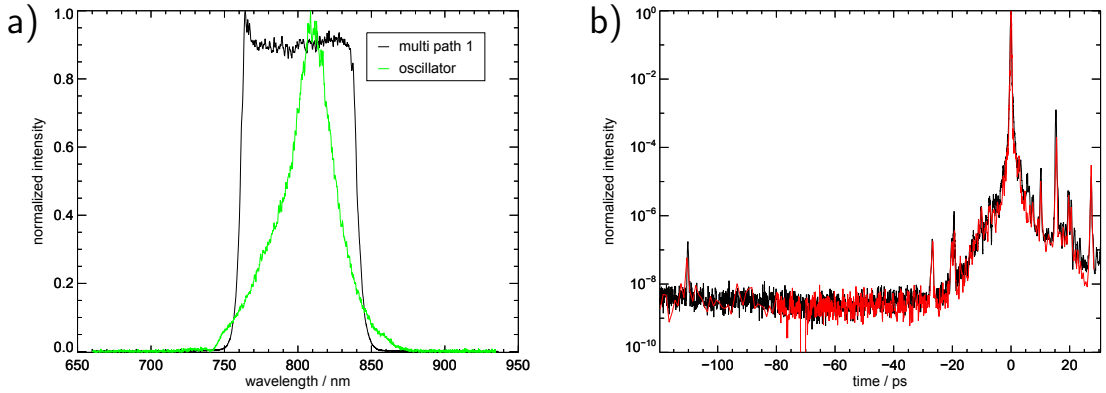

Figure 5.2: **a)** Laser spectrum measured after oscillator and last preamplifier. **b)** Contrast measurements from 28.05.2014 (black) and 04.12.2014 (red)

infinite plain wave. For an infinite distance from the aperture the Fraunhofer approximation can be used and one obtains for this case that the diffraction pattern $F(x, y)$ becomes simply the two dimensional Fourier transform of the aperture $f(x, y)$. A lens images the infinite distance into the focal plane. Thus the intensity distribution at the focus becomes the Fourier transform of the beam profile. The corresponding Fourier space of the spatial focal domain is the angular domain. Collimated light gets bend by a lens with an angle $2r/f$ where f is the focal length and r is the distance to the lens center. In correlation to the time bandwidth product one can find a similar constant product for the spatial width d_F and the width of the angular spectrum D/f

$$C = d_f \frac{D}{f\lambda} \tag{5.3}$$

The value of C can be calculated for analytical functions. For example if a circular aperture with diameter D is assumed, the corresponding Fourier transformation is the Airy function. If d_f is diameter of the first null of the Airy function then $C = 2.44$ or for its FWHM $C = 1.06$. If the beam is Gaussian shaped and sigma is being used for d_f and D then $C = 2/\pi \approx 0.64$. In analogy to the previous section the Fourier or diffraction limited focus has the highest intensity, smallest spot size and requires a flat transverse phase angle. The transverse phase front describes the delay of one part of the beam against another, but the propagation direction of the beam is always perpendicular to phase front. This means in an obscured phase front different parts of the beam move in different directions. This is used in a Shack-Hartmann sensor where the beam is focused with a micro lens array. Each individual focus will experience an offset from its lens axis proportionally to its propagation direction. Thus the pulse front can be reconstructed 5.4. It is useful

to describe the measured phase map as series expansion of orthogonal set of 2D polynomials like the Zernike polynomials. This set of polynomials is particularly useful as each element of the series has a physical interpretation like divergence, astigmatism and coma. Optical elements that introduce phase front distortions prevent diffraction limited focusing. Typically the effects of individual optical elements are small, but in a large laser system the accumulated effect can become problematic. In order to correct the phase distortion an adaptive optic is installed, that can be shaped to produce an inverse phase distortion to the accumulated effect of the laser system and beamline. In order to do that the phase measurement uses the leakage of the second to last mirror before our focusing optic. Since I can't measure a beam with 80 mm diameter a telescope reduces the beam to a diameter of 3.5 mm. In addition I can switch a mirror to measure the focal spot of the

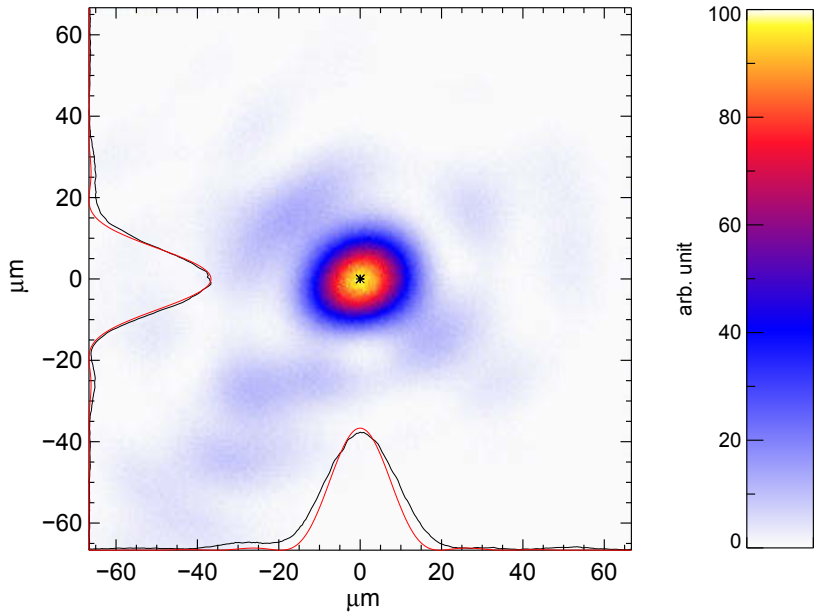

Figure 5.3: Measured parabola focus with 31% of the laser energy within an FWHM region of 19.5 µm (hor) × 17 µm (vert). Shown in red is the profile of a diffraction limited focus.

large diameter spherical lens ($f = 1100$ mm) of the telescope. This reference focus can give easy access to the measurement of focal distortions due to distortions of the phase front, without the need, to set up a focus measurement at the plasma target location. The reference focus was typically checked prior to every LWFA

experiment or occasionally recorded for every single shot (see section 7.3). For the experiment shown in 7.1 another camera was put into the convergent beam at a distance, where the beam illuminates a reasonable fraction of the chip. I could thus measure the phase and the profile simultaneously. The used beamsplitter is not shown in the simplified drawing in figure 3.1. Figure 5.3 shows the focus of the off axis parabola. A microscope objective (NA=0.4) was used to image the focus onto a camera. It was measured with the main amplifier turned off and after phase correction. I measured an energy content of 31 % within an FWHM region of 19.5 µm (horizontal) × 17 µm (vertical). The red curve shows a theoretical focus of a 80 mm diameter beam at $\lambda = 800nm$ with 50 % of laser energy contained within the FWHM of 16 µm.

5.3.1 Phase distortion from the cryo amplifier

When I first started to accelerate electrons in the setup, I observed only very little charge. This was an indication that the laser intensity at focus was lower than expected. After rigorously checking the laser parameters for the system, running at reduced laser power, i.e. the pump lasers of the main amplifier deactivated, I found no evidence for laser parameters being other than expected. Only then I set up the high power laser diagnostic table and found that the focus became heavily obscured, when the pump lasers of the main amplifier were turned on. The Shack-Hartmann sensor and allowed to quantitatively measure the phase distortion. The measurement revealed that the distortion did saturate after approximately 20 min, indicating a thermal effect. A feedback loop to the adaptive mirror was closed and the working solution for the majority of our measurements was to wait for the laser to thermalize. After 20 min I used single shot phase measurements to apply phase corrections to the beam. The consequence was that, I had to wait and compensate with every change of pump energy. Identical cryo amplifiers are in operation at other laser systems. In particular the JETi 200 laser system at Helmholtz Institut Jena reported the same problem. It was found that the Brewster windows used for the cryo amplifier vacuum chamber have an insufficiently low absorption coefficient for the Ti:Sa laser and got non uniformly heated up by a maximum of 2 degrees (see [59] and 5.5). Amplitude technologies suggested to replace these windows with a low absorption fused silica ones and those were tested in Jena first. We received replacement windows, after the majority of the presented measurements in this thesis were already finished. I could measure an increase in laser pulse energy by 10% compared to the old windows at the output of the main amplifier. Also no significant phase distortion effects could be measured. This allowed to reasonably perform the experiment shown in 7.3.

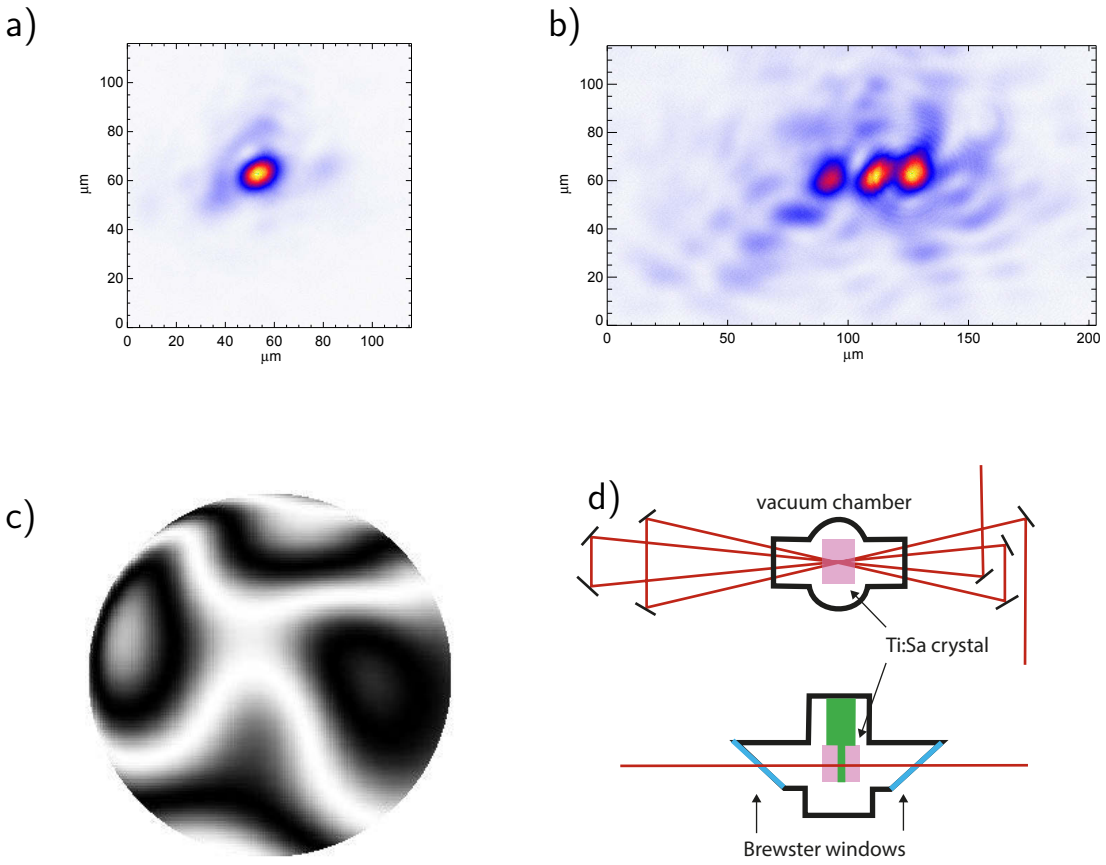

Figure 5.4: Measured foci in the high power diagnostic setup right after turning on the main amplifier **a)** and after 20 min **b)**. **c)** Transverse phase measured with the Shack-Hartmann sensor after 20 min and after correcting for divergence change. **d)** Schematic of the main Amplifier

5.4 Angular chirp

In the last two section I discussed 1D spectral-temporal compression in propagation direction and 2D angular-spatial compression in transverse direction separately. In order to achieve optimal 3D compression of the laser pulse I have to also consider the lowest order of crosstalk between the two domains. For example one can achieve a diffraction limited focus for two different parts of the spectrum which are not centered on top of each other and thus the focal spot taken with full spectrum would appear smeared out 5.5. One may also measure a different but still frequency independent value for the spectral phase for two different parts of the beam. These two effects are actually synonymous to each other and the underlying effect is

either called angular chirp (AC) or pulse front tilt. It is the well known effect of prisms or gratings which causes different colors of the beam propagating in different directions and is typically specified in μrad per nm. For example the first grating in our compressor causes an AC of 1.6 $\mathrm{mrad\,nm^{-1}}$ while in section 7.3 it is shown that for the experiments values better than 0.1 $\mathrm{\mu rad\,nm^{-1}}$ are required. If the beam has AC, the rotation of the compressor gratings can be used as an easy way to compensate for it. For a groove spacing $s = 1480\mathrm{lp/mm}$ and an incidence angle $\alpha = 53°$ and an output angle of the center wavelength (800 nm) $\beta_0 = 22.7°$ on the first grating, I can calculate the residual AC $\partial\phi/\partial\lambda$ from the respective rotation angle of the main gratings ϵ [60].

$$\frac{\partial\phi}{\partial\lambda} = \frac{2\epsilon \tan\beta_0}{s\cos\alpha} \tag{5.4}$$

Thus a misalignment by 50 μrad corresponds to an AC of 0.1 $\mathrm{\mu rad\,nm^{-1}}$. In our compressor the necessary resolution could initially not be achieved with the given step motor resolution. Only after installing a 1:100 gear box our resolution was increased to 6.2 μrad. But rotating the grating parallel to the groves affects the AC only in the horizontal plane. In order to have full control of the AC angle I would also need to rotate the gratings perpendicular to the groves, which the compressor at MBI is not designed for. Thus I propose to use a combination of two wedges to compensate for residual angular chirp. Each wedge creates an AC of a certain magnitude in direction of the wedge angle. The total AC of the wedges can then be calculated using vector addition. It should be possible to create arbitrary magnitudes from minus to plus 2 times the AC of one wedge at arbitrary angles. With BK7 glass as wedge material I have measured an AC of 0.35 $\mathrm{\mu rad\,nm^{-1}}$ per degree wedge angle. The measurement of AC values as low as 0.1 $\mathrm{\mu rad\,nm^{-1}}$ however is difficult. I have set up an interferometric method described by Varju et al [61], and achieved reasonable resolution for values higher than 0.5 $\mathrm{\mu rad\,nm^{-1}}$. I have measured the effect of AC on the electron signal as shown in section 7.3. Another correlated effect to the angular chirp is the spatial chirp. I have stated that the beam profile of the collimated beam represents the transverse angular spectrum and thus all above described effects of angular chirp on the focus and the profile are inverted between the two. Angular chirp causes foci of different wavelength to have an offset with respect to each other, while the pulse front of the collimated beam is tilted with respect to the propagation direction. In case of a spatial chirp the beam profiles of different wavelength are offset with respect to each other and the pulse front is tilted in the focal plane. Of course angular chirp will cause spatial chirp, if the beam is propagated over distance. Typically spatial chirp is not considered a problem as the peak intensity of the focus is only affected due to an effectively decreased pulse duration at focus and this is typically less than residual spectral phase offsets. At this point however I am not aware of a published study on the effects of spatial chirp on laser wakefield acceleration. There is a strong indication that our current way of operating the laser system does not reproduce the same

angular chirp or spectral spatial correlation on a daily base. While optimizing the focus using the transverse phase I obtain similar results for a focus measured with a bandwidth filter. The unfiltered focus however has a varying quality from day to day. Figure 5.5 shows a typical monochrome and different full spectrum foci measured with reference focus setup on the high power laser diagnostic table.

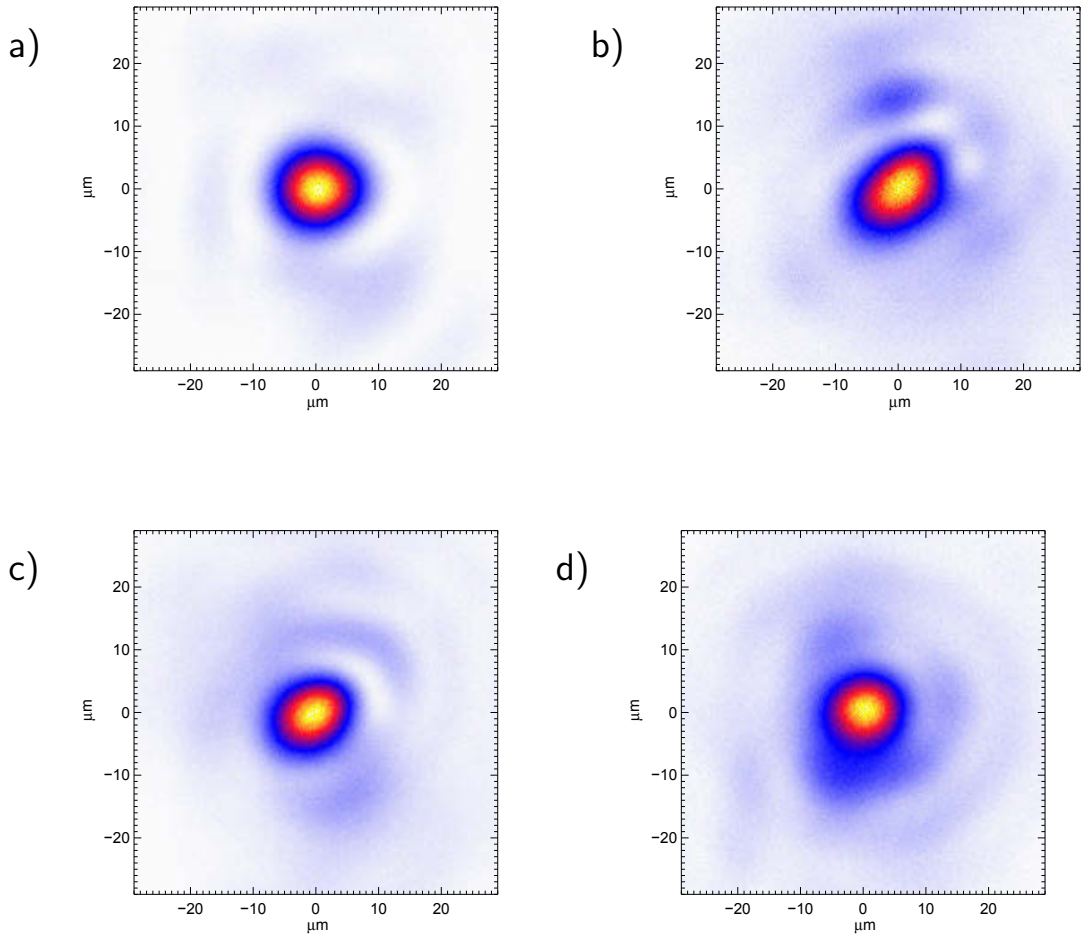

Figure 5.5: **a)** Typical Focus measured with bandwidth filter. Full spectrum foci measured on **b)** 27.02.2015, **c)** 03.03.2015 and **d)** 19.03.2015

5.5 Summary of beam compression

High power ultra short laser pulses have a wide spectrum and beam diameters of up to 200 mm. They represent a technical challenge in controlling the 3D phase relations in order to achieve Fourier limited compression. For LWFA experiments

spectral phase modulators like a DAZZLER, transverse phase modulators like large aperture adaptive optics and high resolution angular/spatial chirp control are vital to produce best results. Deviations from the optimum phase relation can make it difficult to compare results from different laser systems or even between different experiments. For our laser system the use of the adaptive mirror was necessary to produce electron beams. With the adaptive mirror it is possible to further improve the focal quality as shown by Johann Müller [62]. He showed that after preoptimisation for the measured phase front, one can use genetic algorithms to improve the adaptive mirror setup with respect to live measured focal parameters. This method has been shown to significantly improve the focus after 1000-3000 Shots. In our setup the thermal relaxation of the main amplifier in combination with the PSI shot limit prevents us from using that method. But as it has been shown that the quality of the phase front must be measured at full beam amplification, a high power attenuator linked to the PSI would be a recommended future upgrade for the laser. For the measurements presented in this thesis the inability to measure the parabola focus at full power or deduce the focus from a low power measurement, results in an uncertainty for the energy contained in the FWHM of the focal spot or α (section 2.6) respectively. Assuming that after phase correction the high power focus will have similar values to the focus obtained by just running the preamplifiers of the laser chain, I expect an energy content of 20% to 30% in a focal area of 18 µm FWHM. Further assuming a pulse energy of 3 J and a pulse duration of 25 fs I obtain a normalized laser potential of $a_0 = 1.4$.

6 Electron detectors

There are commercially available scintillating screens that can be used for the detection of fast electron, which will be discussed in section 6.1. A screen placed in forward direction was used to measure the angular distribution and overall charge accelerated. Furthermore I have used a calibrated magnet spectrometer to disperse electrons and deduce the electron momentum distribution from the electron trajectories as shown in section 6.2.

6.1 Scintillating screens

For medical imaging scintillating screens have been developed, which convert soft X-rays into visible light. They can also be excited by charged particle beams and are sensitive enough to detect electron beams from LWFA experiments. A. Buck [63] has presented a comprehensive calibration of light conversion efficiency for several different types of scintillating screen material available. K. Nakamura [64] has shown that for the Kodak LANEX Fast Back the conversion efficiency is nearly constant over a broad range of electron momenta. For our setup I used LANEX Fast Front and LANEX Fast Back to detect electrons and image the scintillating screens with AVT Manta G125-B, 12 Bit Ethernet cameras. In order to apply the calibration from [63] I need to obtain a photon count to digital count scale S_{P2D} for our optical setup first. The emission spectrum of the scintillating screens has a sharp peak at 546 nm and I thus used a 550 nm CW diode laser as calibration standard. The CW laser was cross calibrated with a PIXIS 512F camera and has a flux of $(1.6 \pm 0.2) \times 10^{15}$ Photons per second. The laser beam was then aligned through the imaging system onto the CCD chip and S_{P2D} for the entire system of optics and CCD chip could be obtained. As opposed to a diffuse calibration standard, all the light emitted is detected on the chip and angular distribution of the emission can be neglected for this step. On the one hand the laser should be visible for the alignment and then strongly filtered to avoid saturation of the CCD chip. On the other hand this strong filtering yields an uncertainty of 5%, as the transmission sensitively depends on the angle of the filter with respect to the beam. Another 7% uncertainty stems from the uncertainty of the quantum efficiency of the camera, used to calibrate the diode laser photon emission. With

this source of known flux I could obtain the quantum efficiency S_{P2D} for the 4 different optical systems, that are used to image scintillating screens. One camera images the forward screen and 3 cameras are used to image the scintillator screens attached to the magnet spectrometer, labeled MS1, MS2 and MS3 in table 6.1. Table 6.1 contains the summarized calibrations for all 4 camera setups. For the diffusely emitting screen I have to take the solid angle into account. For a camera objective with aperture A and straight distance D to screen the solid angle Φ is defined as

$$\Phi = \frac{(0.5 \times A)^2 \, \pi}{D^2} \tag{6.1}$$

The photon yield per charge can be obtained from the publication of Nakamura [64] as $S_{C2P} = 11.2 \times 10^9$ Ph ster^{-1} pC^{-1} for the LANEX Fast Back and 5.6×10^9 Ph ster^{-1} pC^{-1} for the LANEX Fast Front. The Back screen is twice as thick as the Front screen and I consider a linear dependence of the light yield with the path length, hence the photon yield is doubled. I can thus obtain a scaling factor between digital camera counts and charge S_{C2D} with the unit digital count per pC as follows

$$S_{C2D} = S_{C2P} \cdot \Phi \cdot S_{P2D} \tag{6.2}$$

This value is further modified and in this form it is only applicable for a signal

Camera	Forward Screen	MS1	MS2	MS3	Unit
Lanex	Fast Back		Fast Front		
S_{C2P}	11.2		5.6		$\times 10^9$ Ph. sr^{-1} pC^{-1}
S_{P2D}	0.075	0.12	0.10	0.05	per Photon
Focal length	25		6		mm
Angle of View H	11.1		44		degree
Angle of View V	8.3		33.5		degree
Incidence Angle	45	f(E)	f(E)	≈ 17	degree
f#		1.4			
Distance	88 ± 2	51 ± 2	52 ± 2	49 ± 2	cm
Solid angle	32.0	5.8	5.5	6	$\times 10^{-5}$ sr
S_{C2D}	385	33	26	15	$\times 10^3$ pC^{-1}

Table 6.1: Calibration for Cameras observing scintillating screens

in the center of the image, and only if electrons cross the screen perpendicular. Electrons crossing the screen at an angle, have an effectively longer pass through the scintillating material which linearly increases the light yield [64]. For the case of the forward screen the LANEX is mounted at a 45° angle with respect to the electron trajectories increasing the path length by a factor $\sqrt{2}$. In case

of the magnet spectrometer screen I will have to apply a calibration along the screen to account for the different angles at which electrons cross the scintillator material (see section 6.2). Furthermore there are several optical effects that lead to a decreased sensitivity of imaging systems towards the edges of the field of view called vignetting.

- If I assume that the imaged screen is a plane, tangent to the center of the image, take into account the difference in distance $D_\alpha = D/\cos\alpha$ with the observation angle α and plug it into equation 6.1, I obtain a dependence with $\cos^2\alpha$ for the deviation from the image center.
- Then I have to take the Lambertian law into account, which states that a diffusely emitting surface will radiate intensity in cosine angular dependence with respect to its surface.
- And finally, I have to take into account the projected lens aperture, which gives another power of $\cos\alpha$.

This adds up to a $\cos^4\alpha$ dependence for the camera vignetting and is sometimes referred to as natural illumination falloff. I have measured this effect using a tritium filled scintillator capsule (figure 6.1). The capsule was cross referenced against our CW laser to allow for a quicker and easier calibration. These capsules emit light at constant rate and are referred to as constant light sources (CLS). The use of these CLS as references has been discussed in [63] and it was shown, that these tritium dots also follow the Lambertian law around their symmetry axis. The CLS used for our calibration was measured to emit 7.4×10^7 Ph. $\mathrm{ms}^{-1}\,\mathrm{ster}^{-1}$. I have tested the $\cos^4\alpha$ dependence by placing the tritium dot at different positions along the screen and found indeed a good fit.

6.2 Permanent magnet spectrometer

In order to disperse the accelerated electron beam, a magnet was used with a field distribution perpendicular to the electron beam as depicted in figure 6.2. The field was measured with hall probe setup provided by the "Helmholtz-Zentrum Berlin für Materialien und Energie" [65] as shown in figure 6.2**b)** and it was also simulated using the Radia code for Mathematica [66] as shown in figure 6.2 **a)**. The difference of the two calibrations is plotted in figure 6.2 **c)** and the difference does not exceed 2% of the maximum field value of 0.66 T. The magnet is 80 cm long and weighs ≈250 kg. When I calibrated the magnetic field, I could only obtain field measurements in the plane, centered between the pole shoes ±2 mm. The sensor head containing the Hall probe was 11 mm thick, while the gap of the magnet spectrometer is 14 mm. As the simulated field distribution fits the measurement very well, I continue the trajectory calculations with the simulated field, which is available for the full gap. For a particle entering the field of the

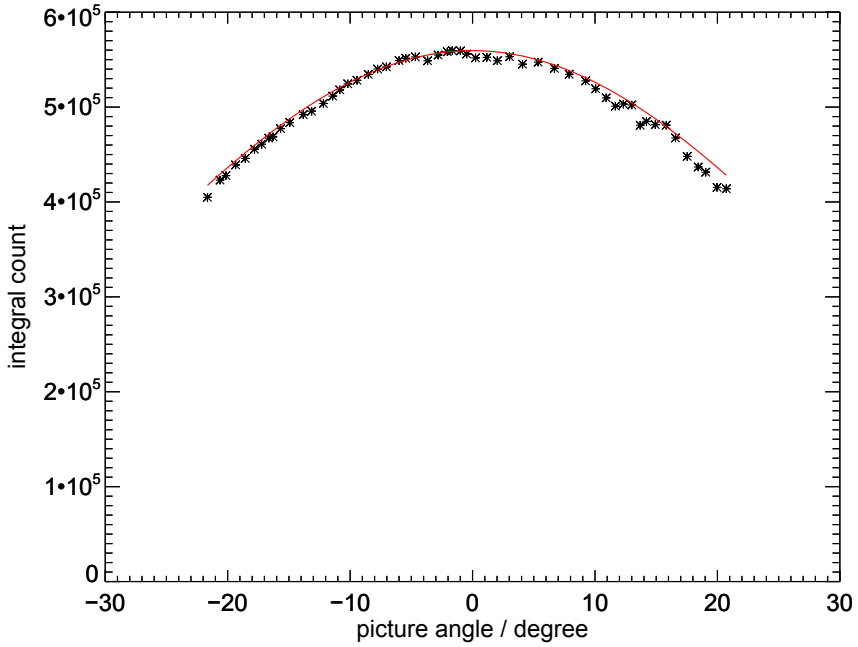

Figure 6.1: Measured integral count of a tritium dot at different position on the screen. The illumination falloff follows a $\cos^4$ of the observation angle as fitted in red.

magnet on a defined axis I can calculate trajectories of that particle depending on the particles energy and charge. With a sufficient number of trajectories, I can interpolate at which position trajectories, with a given particle energy and offset, will cross the scintillating. In order to calculate an energy resolution of the magnet spectrometer, one has to compare the effects of an initial offset with the dispersion due to the difference in energy. The trajectories were calculated using the program General Particle Tracer (GPT [67]). Magnetic fields are capable to focus collimated beams of charged particles in one plane. Typically this is only achieved in one plane, while the beam gets defocused in the plane perpendicular to the focusing plane. Only in very specific configurations, like multiple quadrupoles separated by drifts, a focusing in both planes can be achieved for specific particle energies. When designing a magnet spectrometer it is desirable to achieve focusing in the dispersive plane and detect particles of different momenta at their respective focus. In this focal plane the dependence of detection position to initial trajectory offset is minimized and thus the energy resolution maximized. For the simulated field distribution I have calculated the trajectories of divergent electron beams with different momenta as shown figure 6.3. For most of the trajectory bundles of

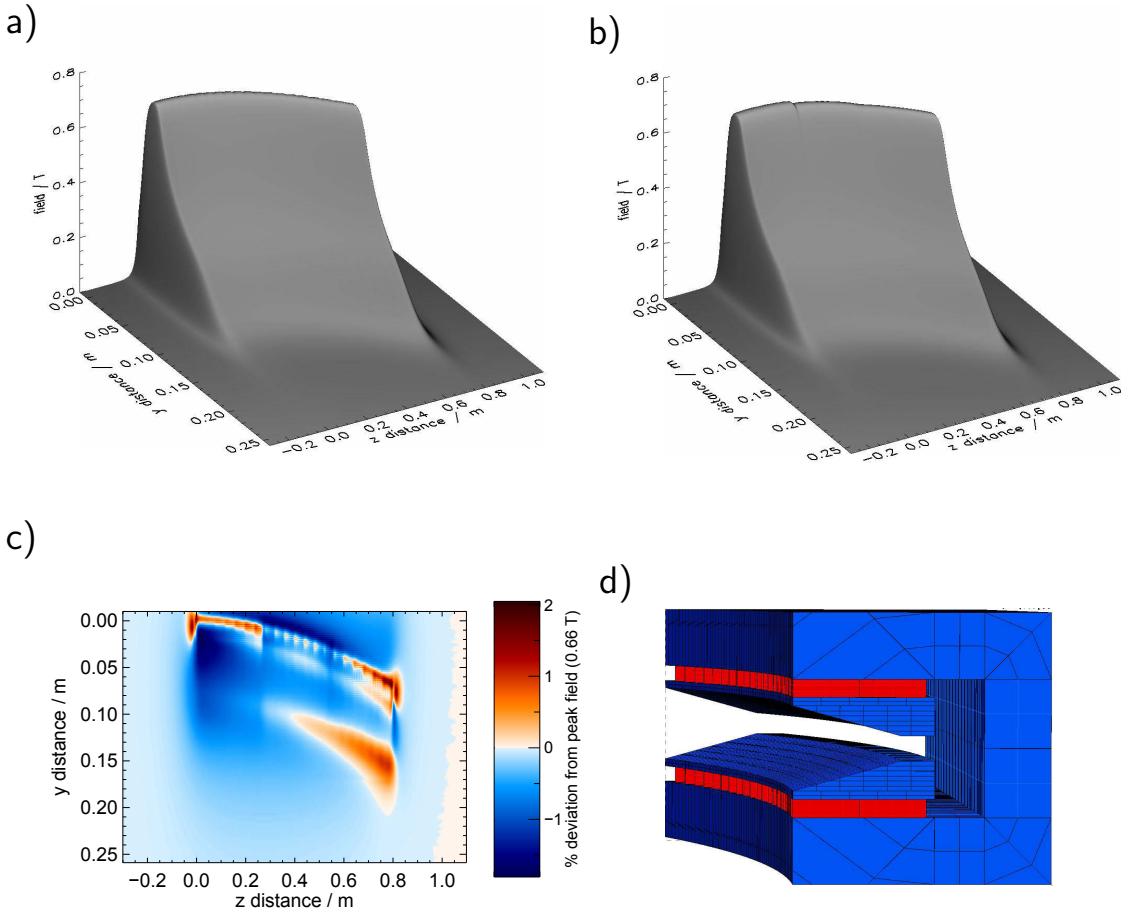

Figure 6.2: The simulated **a)** and the measured **b)** field in the plane centered between the gap of the electron spectrometer. A comparison of simulation and measurement is plotted in **c)** with positive deviation (measured greater than simulated) in red and negative deviations in blue. **d)** shows the model of spectrometer used in the simulation with the permanent magnet in red and steel components in blue.

identical particle energy I find the focus inside the magnet as denoted by diamond symbols in figure 6.3. For technical reasons our scintillating screens are mounted on top of the yoke, represented by the black solid line, typically a few centimeter behind the focal plane. Each of the trajectory bundles contains one trajectory, which enters the magnet with zero offset. For the crossing of one particle bundle with the screen I can obtain a scaling factor on how much the initial offset will have evolved through linear regression. Interpolating between the crossing of the ideal trajectories with the screen, I can obtain the energy calibration of the magnet spectrometer $E(s)$ for a screen location s. If the scaling factor for initial offset to offset on the screen is then compared with the energy calibration I can obtain a

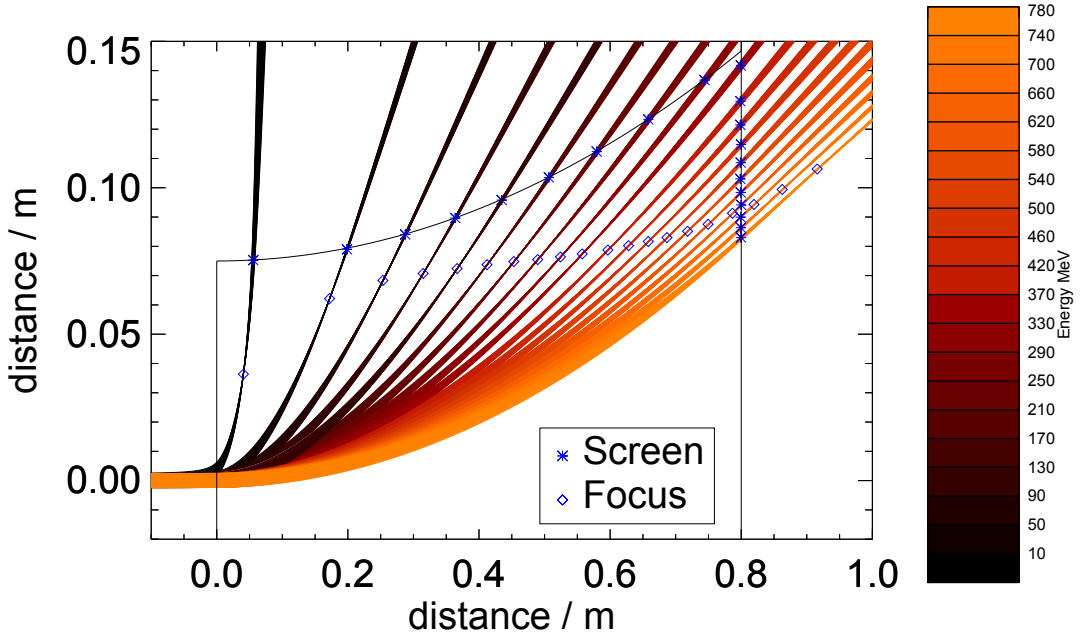

Figure 6.3: Trajectories of beams with different energy in the magnet spectrometer. The black box denotes the magnet yoke.

type of energy resolution, that is independent of the magnet spectrometers aperture as plotted in figure 6.4 with the unit MeV mrad^{-1}. The electron beam source of a few micron at the exit of the laser plasma interaction can be considered as a point source and I refer to offsets in terms of angular offset. The vertical size of the mostly used entrance aperture of 5 mm located at 1230±5 mm behind the laser plasma interaction thus yields an acceptance angle of 4 mrad. If the electron beam divergence is larger than this aperture one can obtain the energy resolution by multiplying the aperture size with the values given in figure 6.4. For example the aperture independent resolution of 1.3 MeV mrad^{-1} at 200 MeV corresponds to an energy resolution of 5.2 MeV or 2.5% relative resolution for large beams. Smaller divergences of electron beams have been measured and the corresponding energy resolution for those beams can be extracted from figure 6.4 in a similar fashion using their respective divergence. I also need the incidence angle of the trajectory into the screen in order to calibrate the light yield from the screen as discussed in section 6.1. How this affects the measured spectra will be demonstrated in the next section.

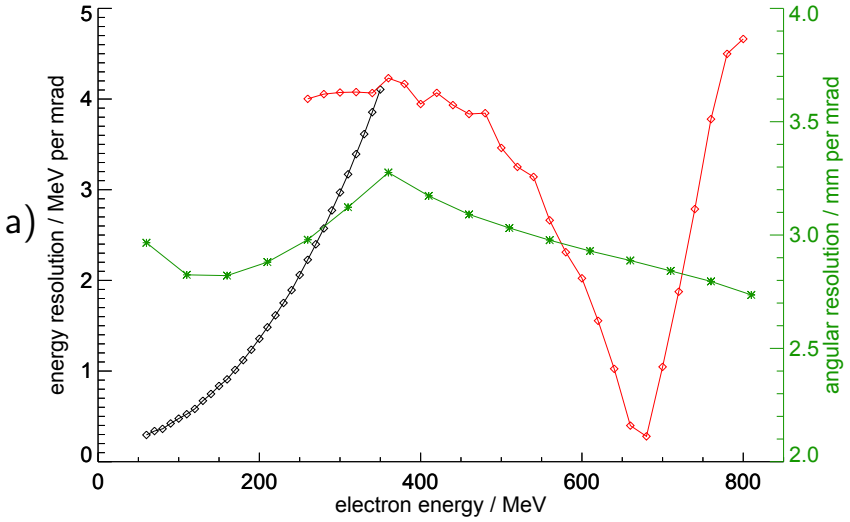

Figure 6.4: Resolution limit of the electron spectrometer for the screen mounted on the long side (black) and the front (red) as seen in figure 6.3 . Angular resolution (green).

6.2.1 Reconstruction of electron energy spectra

On the 80 cm long side of the electron spectrometer I have mounted 2 strips of LANEX Fast Front scintillating screen 40 cm by 5 cm directly on the yoke of the electron spectrometer. This side of the spectrometer is imaged by two cameras with some overlap. The first camera labeled MS1 in table 6.1 images the part of the screen corresponding to electron energies from 17 MeV to 220 MeV. The second camera images an area corresponding to electron energies from 135 MeV to 350 MeV. Another scintillating screen is mounted at the far side of the electron spectrometer, which can detect all remaining particles that are only weakly or not deflected by the magnetic field. This screen is reaching far enough, so that particles between 270 MeV and 350 MeV that have crossed the first screen, can leave a second trace on the far end screen. The camera imaging that screen is labeled MS3. Typically, electron energies in our experiments do not exceed 300 MeV and I thus focus on the evaluation of the data from camera MS1 and MS2. In figure 6.5 the charge per pixel column is plotted for MS1 (black) and MS2 (red) for the 4 steps of charge measurement correction. The first picture shows the charge per pixel column plotted as a function of their respective electron energy. The signals of the two cameras differ in a way that can not be described by an offset or factor constant with respect to energy. After applying the $\cos^4$ law as discussed in section 6.1 the signals

of the cameras only differ by a factor due to the difference in distance and thus solid angle of detection. This has been taken into account with the calibration factor given in table 6.1. Thus in the next step the cameras show reasonable agreement about the measured charge per pixel column. The total measured charge in this step adds up to 54 pC. The electron beam in this case was also detected on the forward screen, where its total charge measured adds up to 176 pC. Its divergence was measured as 10.5 mrad (standard deviation). After the beam scatters on the forward screen and its shielding aluminum sheet, I expect a significantly smaller fraction of the beam to be detected in the electron spectrometer. I thus take the incidence angle into the screen into account, which is obtained from the simulated trajectories. After this step I obtain a more even distribution of the charge as a function of electron energy , which is what I expect from the underlying physics of this type of electron beam produced by ionization injection (see section 8.2). The total charge in the last case adds up to 12 pC. It may be questionable to

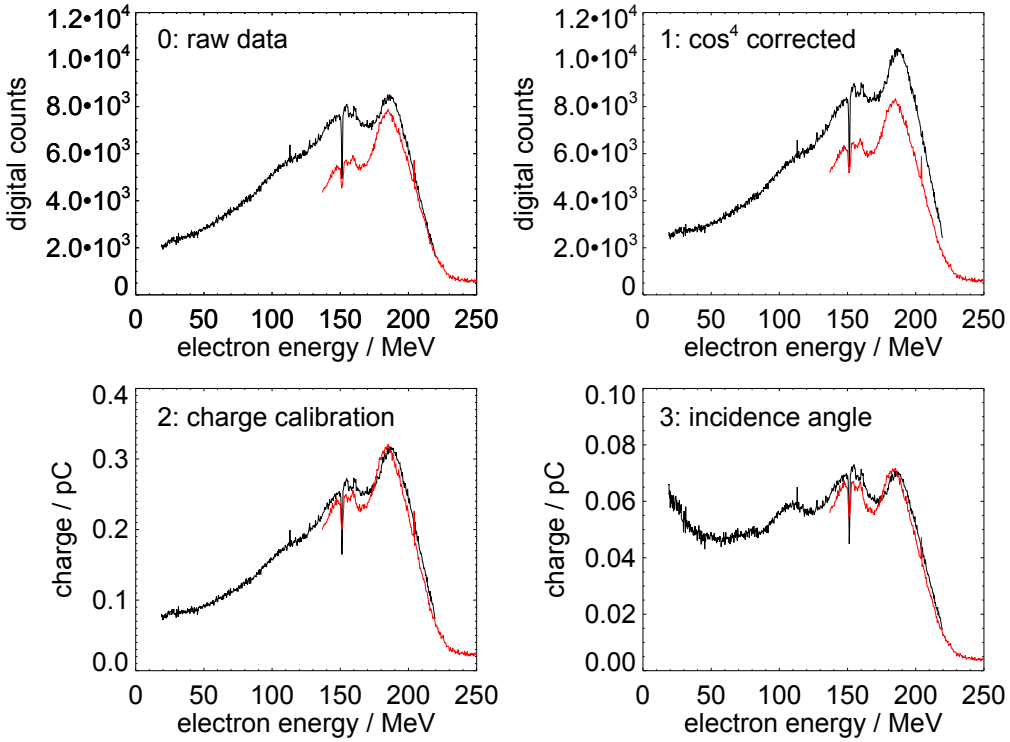

Figure 6.5: Line averages in non dispersive direction for the electron spectrometer screen. Shown are the correction steps from raw data (o), $\cos^4$ correction (1), charge calibration from table 6.1 (2) and the correction of incidence angle to the final result (3). Note the different axis scaling.

which extend the light yield from the scintillating screens corresponds linearly to the path length, but no published measurements are available right now. As I see that electrons are not stopped significantly by a single screen it should be possible, to device an experiment, where multiple screens are penetrated by a single electron bunch. A two screen setup with a second screen mounted on a rotation stage would possibly be sufficient to compare the screens. As charge stability is not required due to the direct comparison of the screens, this experiment could be performed on an LWFA setup. In general it should probably be avoided, to cross scintillating screens at too small angles in order to properly compare the measured charge.

Part III

Electron beams

7 Beam stability and steering

After the issues regarding the phase distortions created by the main amplifier (see section 5.3.1) were successfully resolved, electron beams with some pC charge could be produced routinely, using either ionization injection or shock-front injection at densities of $2 - 5 \times 10^{18}\, e^-\,\mathrm{cm}^{-3}$. I will discuss the specific properties of these injection methods in the next chapter 8. However, only to generate electron beams with detectable charge is not sufficient in order to study the parameter dependence of the laser wakefield acceleration. The accelerator setup needs to provide a certain electron beam stability in order to compare different parameter sets and experimental setups. As an example 150 consecutive shots taken at an effective laser energy of $\alpha E = 0.23\,\mathrm{J}$ are discussed as shown in figure 7.1. The plasma target was the type I nozzle with 2 mm exit diameter and 0.52 mm throat. The laser passed the nozzle 3.2 mm above the nozzle exit and the backing pressure was 12 bar with helium nitrogen mix of 2% nitrogen. In figure 7.1 **a)** an electron beam on the forward screen is shown that would miss the entrance aperture of the magnet spectrometer entirely, which was aligned to the laser axis. In figure 7.1 **b)** the centroids for all 150 consecutive shots are plotted and one can identify two reasons why electron beams would miss the electron spectrometer. On the one hand there is a pointing fluctuation with a standard deviation of 3.5 mrad in both directions. But on top of that it is observed, that the average of the centroids has a deviation from the assumed laser axis by 4.2 mrad horizontal and 2.7 mrad vertical. In the scenario shown in figure 7.1 **b)** less than 20% of the electron beam centroids lie within the electron spectrometer aperture. In this scenario one actually benefits from the large pointing, as the hit rate would decrease if a better pointing is achieved. The beams in this scenario have an average divergence of 4 mrad horizontal and 3 mrad vertical, which means a lot more beams than the 20% would lie at least partially within the spectrometers aperture. But again the hit ratio would decrease if a small divergence is achieved. As one would consider small divergence and small pointing a desirable performance to achieve, it must thus be a high priority to investigate and eliminate beam steering. In the above scenario the hit rate would increase to 50% if no steering would be present and only pointing would be considered.

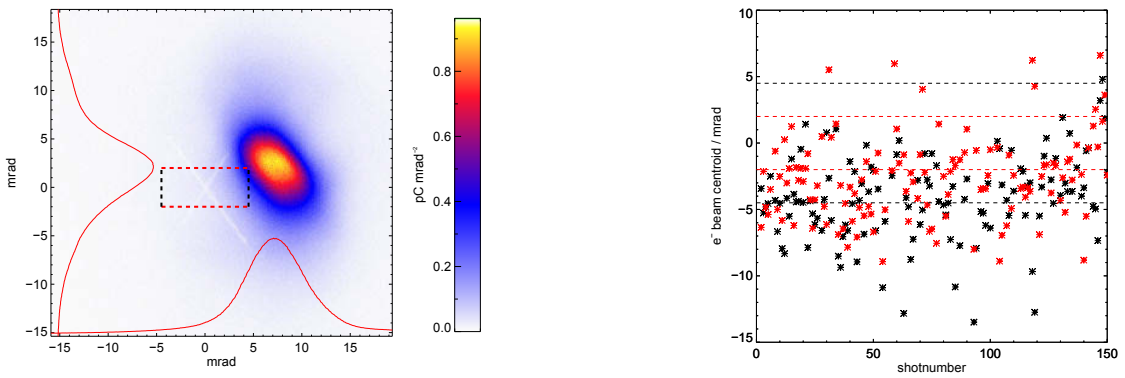

Figure 7.1: a) Electron beam on forward screen that misses the entrance aperture of the magnet spectrometer (box). **b)** Centroids of consecutive shots for horizontal (black) and vertical (red) direction. The entrance aperture of the magnet spectrometer is shown in dashed lines in both graphics.

7.1 Steering with an aperture

Above I introduced the phenomena, that electrons appear to be accelerated at an angle with respect to the aligned laser axis. As a starting point of an investigation I may thus first elaborate on the term laser axis. In order to align the laser beam through the laser setup and the experiment I typically close an aperture around the center of the beam. This allows to align the propagation direction of the collimated laser with good precision, but not necessarily the position. As the laser profile is typically not a flat top circle with a defined center, the question arises on how to define the position of a $\approx 80\,\mathrm{mm}$ diameter beam. The reduced beam produces a rotational symmetric diffraction pattern of the aperture, which I can position onto our alignment crosses with less than one millimeter precision, but the beam center might be offset by a few millimeter. When the beam gets focused, this parallel offset gets converted into an angular offset as shown in figure 7.2 **b)**. In order to investigate this more closely I designed the following experiment. A diaphragm on a motorized linear stage is placed in the beam path and its center is aligned to the reduced laser beam center. A camera was installed on the laser diagnostic table, after the large aperture lens and into the convergent beam, so that the laser profile behind the diaphragm is obtained. Electrons were accelerated in a gas cell with mixed gas (see section 8.2.2). The aperture is then closed to an opening of 75 mm, cutting the laser beam profile by at least 2.5 mm on all sides. I then moved the aperture 2.5 mm up and down and measured electron beams on the forward screen. The laser profile was measured simultaneously. I applied a centroid fit to electron beam and laser profile and the result is shown in figure 7.2 **a)**. In this graph the centroid of the laser profile is given in the resulting angular change due to the

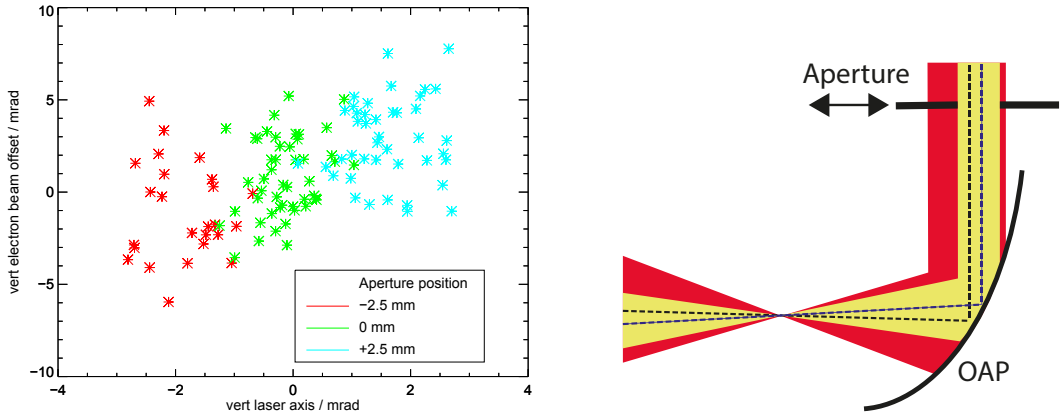

Figure 7.2: **a)** Electron beam steering as function of expected beam steering from shifted laser centroid for 3 different aperture positions. **b)** Schematic of aperture induced steering

parabola focal length. Hence a centroid offset of 2.5 mm would yield an angular change of 1.7 mrad with the focal length f =1.5 m, which is in reasonable agreement with the observed electron steering. The averages and standard deviations for the three sets of data are listed in table 7.1. Fluctuations in the laser profile

Acceleration performance				
Target type	3.5 mm gas cell with mixed gas			
Density	3×10^{18}			$e^{-}\mathrm{cm}^{-3}$
e^- centroid	$1.6(h) \times 0.7(v)$			mrad
e^- pointing	$1.9(h) \times 2.3(v)$			mrad
e^- divergence	$2.6(h) \times 2.6(v)$			mrad
Aperture experiment				
Ap. offset	-2.5	0	2.5	mm
$\Delta\phi_{laser}$	-1.7 ± 0.1	0 ± 0.1	1.7 ± 0.1	mrad
St. Dev. $\Delta\phi_{laser}$	0.5	0.3	0.3	mrad
Δe^- centroid	-1.9 ± 0.5	-0.2 ± 0.3	1.9 ± 0.4	mrad

Table 7.1: Results of the aperture experiment as shown in figure 7.2

are measurable and affect the centroid, such that a pointing fluctuation of the resulting laser axis and the accelerated electron beams of 0.5 mrad may be caused. The electron beam pointing has been measured to ≈2 mrad and there is no direct correlation between the intensity fluctuations and electron beam pointing. One can assume that the diaphragm used to reduce the laser beam size for alignment, is centered to the beam better than ±3 mm and thus the here described effect should

contribute to the deviation of the average electron beam centroid with less than 2 mrad.

7.2 Plasma gradient steering

At an experiment with mixed gas and a nozzle with 0.52 mm throat and 2 mm exit diameter, I encountered an electron beam steering of 8 mrad horizontally. The laser passed 1.6 mm above the nozzle exit. It is known that a plasma gradient can cause beam steering and I changed the horizontal position of the gas jet with respect to the focus. This had little effect until the offset was as big as 800 μm, where I did achieve a steering of the electron beam by said 8 mrad with a pointing stability of 1 mrad (standard deviation). The main amplifier was turned off and a picture of the plasma trace with the preamplified beam was taken as shown in figure 7.3. The laser is steered towards the higher index of refraction and thus hitting the left side jet gradient the laser and the electron bunch is steered to the right side. This way I could measure the energy while varying the jet backing pressure as shown in section 8.2.1. While plasma gradient steering can provide sufficient angular offset, it was most certainly not the cause for the initial offset. Thus I continued with

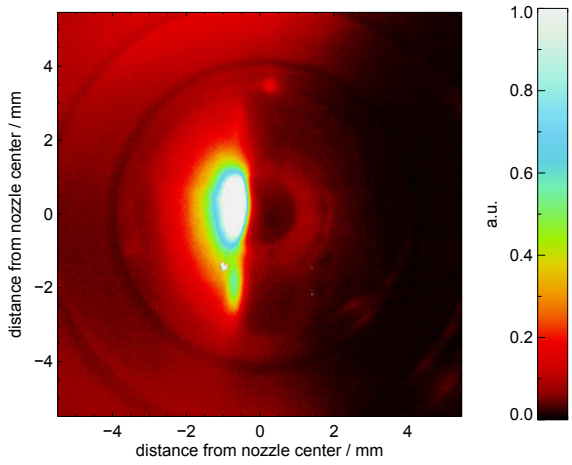

Figure 7.3: Direct imaging of the plasma trace over the nozzle after strong gradient steering was applied.

the experiment described in the next section 7.3. I can't provide sufficient data for a comprehensive analysis of gradient induced steering. Small samples however, indicate no variation of the average electron beam centroid if the laser is centered above the gas nozzle with a typical precision of ±100 µm using the direct imaging

system. This is consistent with the observations in section 4.1 where I have shown, that at a height of 1.6 mm the gas jet profile is close to a flat top distribution.

7.3 Steering with angular chirp

This experiment was performed with the condition described in the above section 7.2, where an offset of 8 mrad of the average electron beam centroid was observed after regular alignment procedure. Another possible way to steer the electron beam away from the laser axis has been described by A. Popp *et al.* [68]. She stated that angular chirp (AC) in the laser pulse produces an asymmetric wakefield that accelerates electron beams at an angle with respect to the laser axis. The necessary theory on angular chirp and how it is manipulated is shown in section 5.4. The quickest way is to rotate one compressor grating around the direction of the grooves. This also changes the direction of the laser beam and the beamline has to be realigned. The electron beam profile was measured on the forward screen for 5 different grating positions and I took 50 shots on each position.

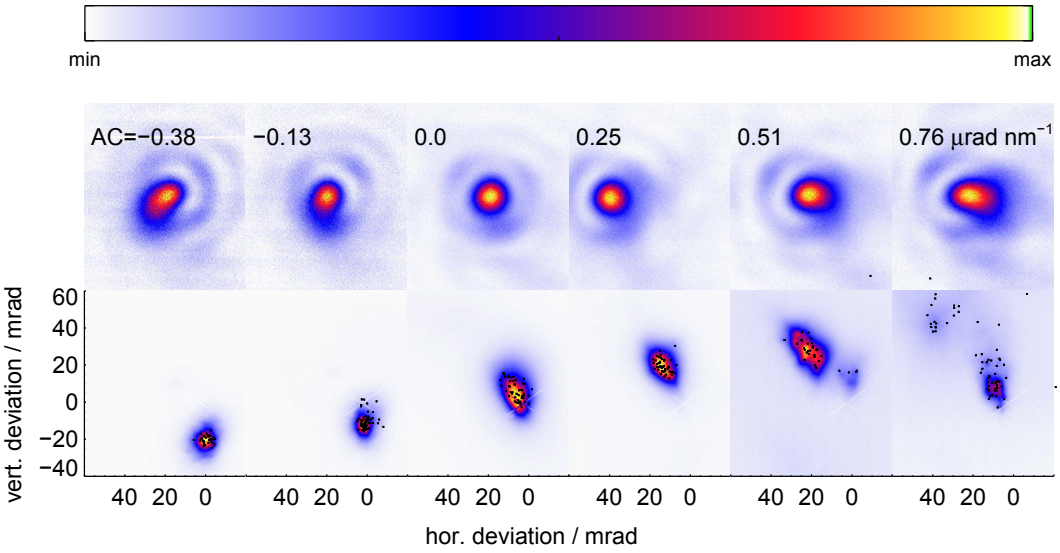

Figure 7.4: Foci (top row) and average angular electron distribution (bottow row) for different angular chirps (column). Centroids of individual shots are marked with black dots. Each image is scaled between its respective minimum and maximum.

Figure 7.4 shows the averaged beam profiles for different grating rotations. AC also causes a spatial chirp in the focus, which then appears elongated. Thus I measured the reference focus in parallel. The reference focus is the full beam leakage focused by a spherical lens with f =1.2 m. In figure 7.4 I have plotted selected pic-

tures of the focus for each series and I do observe the predicted asymmetry. Also I observed that the minimal focal distortion coincided with the least offset of the average electron beam centroid. The relative change of the AC can be derived from the rotation angle of the compressor grating using equation 5.4, but an absolute measurement of the AC is not available. Thus I refer to the third measurement with the minimal electron beam steering and focal spot distortion as Zero AC and write the other measured values of AC with respect to that scan. The average electron beam centroids as a function of AC are plotted in figure 7.5. A linear regression through the first 4 datasets yields a dependence of the beam steering on AC as (45 ± 7) mrad per $\mu\text{rad}\,\text{nm}^{-1}$. Thus if electron beam steering with less than 2 mrad is required, the AC needs to be controlled with a precision of less than $0.05\,\mu\text{rad}\,\text{nm}^{-1}$. One can see that the dataset at $0.25\,\mu\text{rad}\,\text{nm}^{-1}$ shows little distortions of the focal spot, while the beam is steered by more than 10 mrad. Thus a correction of the AC based on focal spot measurements will not yield a sufficient precision. An optical method for absolute measurement of AC will be demonstrated in attachment A.3, but it also did not yield sufficient precision. However, as the minimal electron beam steering coincided with the most symmetric focus, I can conclude that the initial beam steering of 8 mrad was dominantly caused by angular chirp of the laser beam. The measurement presented in section 7.1 has been performed a few days earlier, where only little electron beam steering was observed. Supposedly the compressor gratings were not moved in the meantime. In general I can state that AC can easily cause electron beam steering up to 10 mrad and apparently changes on the order of $0.1\,\mu\text{rad}\,\text{nm}^{-1}$ may occur spontaneously. Such a change corresponds to a rotation of one compressor grating by 50 µrad. As the gratings are placed 1 m apart such a change may be introduced by asymmetric thermal expansion. Generally I can conclude that AC is most likely the dominant physical effect for electron beam steering in excess of 3 mrad, but the actual laser component that causes frequent changes in the AC is not clearly identified. In the work of A. Popp *et al.* [68] a much weaker dependence of the electron beam steering with AC was observed. For values of less than $0.5\,\mu\text{rad}\,\text{nm}^{-1}$ only very little steering was observed. For values of $1\,\mu\text{rad}\,\text{nm}^{-1}$ they observed a beam steering on the order of 10 mrad, coinciding with large pointing fluctuations. Plasma density, focal length and laser energy were similar to the conditions in our experiment, but the target was a steady state gas cell instead of a super sonic jet nozzle. Also they relied on self injection instead of stimulated injection. They stated, that the increased laser focal spot size decreased the laser intensity and that they had to increase the plasma density at higher AC values in order to achieve injection. This might have also been the reason why they observed significantly increased pointing fluctuations of the electron beams at higher AC values. In this case it was possible to maintain reasonable pointing stability of 3 mrad, while steering the electron beam up to 20 mrad away from the laser axis. Another difference between the two experiments was the longer pulse duration of $\tau = 37$ fs in their experiment, compared to 25 fs in our case. Although no value is explicitly stated, this implies

a narrower laser spectrum (see section 5.2). As the AC is the gradient of wavefront angle over wavelength a wider spectrum introduces larger wavefront angles at the same AC. This could also be a reason, for the increased sensitivity to AC in our case. At higher AC values I observed a high pointing fluctuation, but fre-

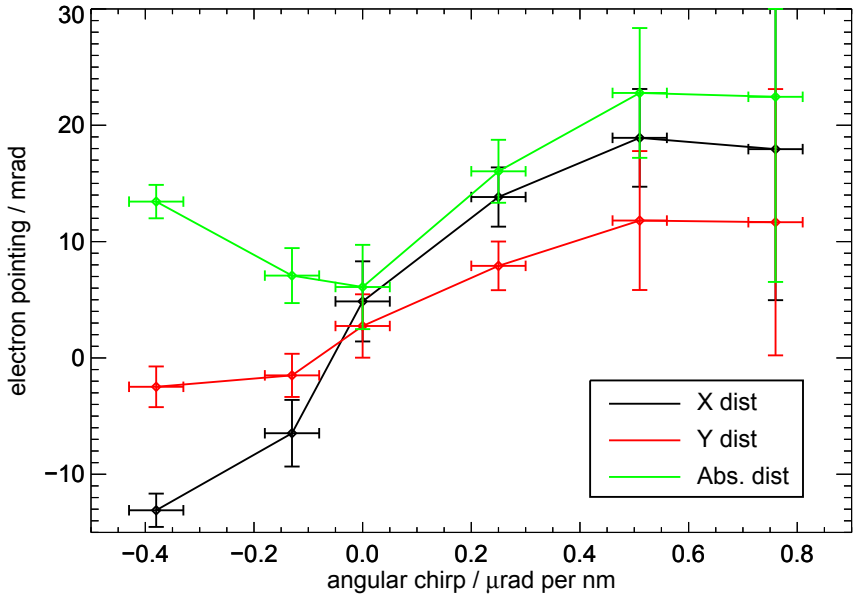

Figure 7.5: Plotted are horizontal (black), vertical (red) and absolute deviation of the average electron beam centroid from the laser axis as a function of angular chirp.

quently electron beams with low charge appeared close to the laser axis. In his work Mangles *et al.* [9] stated that laser energy not contained in the focal spot will diffract away as the focal spot self modulates and compresses while forming the wake. Following this argument I assume that the tail in the focal picture at the AC of $0.75\mu\text{rad}\,\text{nm}^{-1}$ will start to diffract away and the wake dynamics are driven by a laser pulse with less energy and less spectral bandwidth, causing acceleration of low charge electron bunches that are steered significantly less. Lastly I noted that the electron beam was also steered vertically. This emphasizes that the mount of the compressor gratings may not be suitable for the required adjustment precisions and the grating may also have rotated around the axis perpendicular to the groove direction. This is the axis that could cause an AC in vertical direction, but it is not remotely adjustable. With the presented measurement I obtain a scaling, which would allow for a quick compensation of horizontal electron beam steering. As this

was one of the last experiments performed, this solution was never applied other than in the shown case.

7.4 Raman scattering and pulse duration

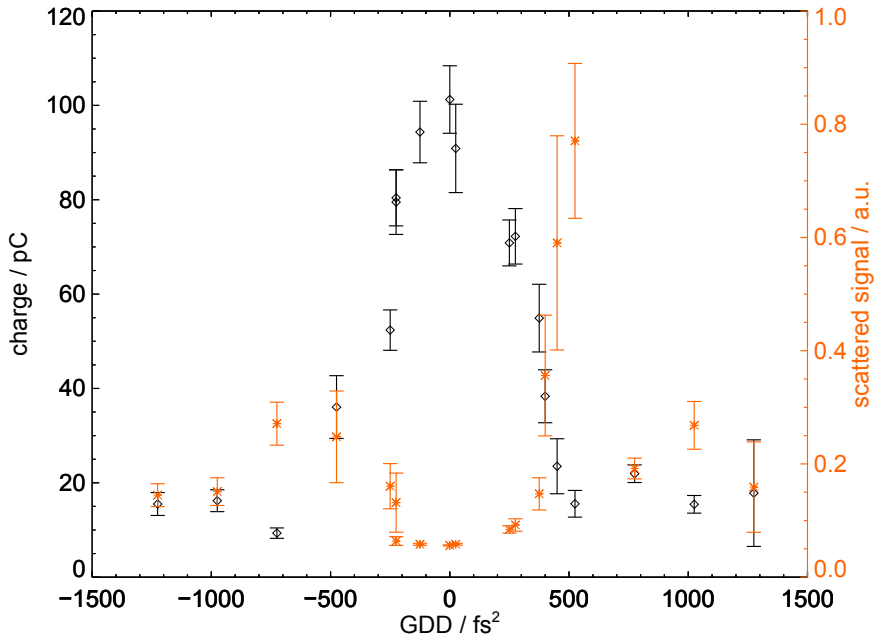

Figure 7.6: Measured charge on forward screen and scattered light in direct plasma source imaging as function of GDD

At several occasions I observed that the accelerated charge drops, at seemingly unchanged experimental conditions. The direct plasma imaging camera is not fully blocked during high power operation, but strongly filtered. I used neutral density filters and two near infrared interference filter with low transmission above 730 nm and less than 1% above 780 nm. The image is obscured due to multiple reflections, but I observed a correlation of the amount of laser light scattered into the camera and the integral charge accelerated. Furthermore I scanned the compressor translation and measured both signals as depicted in figure 7.6. The experiment shown used a nozzle with 0.52 mm throat and 2 mm exit diameter at 1.3 mm above the nozzle exit, yielding a plasma density of $(5 \pm 0.5) \times 10^{18}\, e^- \,\mathrm{cm}^{-3}$. The effective pulse energy was $\alpha E = 0.27$ J and injection was stimulated with a shock-front. As the pulse duration was changed I observed the total charge declining for positive and negative GDD. Using the SPIDER we found that 100 µm compressor translation corresponds to approximately 250 fs^2 GDD. The signal of the scattered light vanishes at optimized pulse duration, but peaks for small deviations from that. In order to determine the mechanism, which leads to the scattering of light in the plasma, the signal needs to be spectrally resolved. Most likely sources are Raman scattering of the laser on the wake structure or nonlinear Thomson scattering on the

plasma electrons. In either case the vanishing of the signal, coincidental with peak electron signal, may be caused by wake cavitation. If the pulse is fully compressed and a wake is formed, a large fraction of the laser pulse propagates in the plasma cavity and no scattering occurs. The scattering occurs frequently in different experiments and I typically used the same filter setting for the camera. That the signal does not vary by orders of magnitude throughout the experimental campaign, hints more towards a scattering on the wake structure rather than a nonlinear scattering on the plasma electrons, because it implies a more linear correlation between input laser energy and scattered signal. I only used this effect to monitor if the laser pulse compression is correct and, if necessary, optimized the compressor translation for minimum scattered signal. However this was so frequently necessary, that we monitored the pulse duration for full day using a SPIDER. We indeed observed a slow drift of the GDD with a maximum GDD difference of $800\,\mathrm{fs}^2$ after 5 hours in one of the worst scenarios.

8 Injection mechanisms

In order to study the acceleration of electron beams in the LWFA regime, one needs to provide detectable amounts of electrons that undergo acceleration, in order to obtain information about their evolution. Necessarily one has to decide between the different options at hand and in this chapter I will thus compare three different options for injection of electrons from the plasma background. The first option is to work at sufficiently high plasma densities in order to achieve wavebreaking or self injection as shown in section 8.1. Our primary interest is to avoid such an injection, as the focus of this thesis are stimulated injection types with additional tuning parameters. Typically the tuning parameters are the respective position of the supersonic nozzle and the laser focus, the backing pressure of the jet nozzle, the nozzle shape and the laser pulse energy. The dependence on the laser parameters pulse duration and angular chirp (AC) have been discussed in the previous chapter, where it was shown that deviations from minimized AC and shortest pulse duration will reduce the injected charge and steer the electron beam away from the laser axis. When operating at plasma densities below the self injection threshold, the simplest method to obtain electron beams is the use of nitrogen enriched helium gas. This does not provide additional tuning parameters other than the mix ratio, which was fixed at 2% nitrogen in the presented experiments. But it allows to study the LWFA performance at densities below the self injection threshold (see section 8.2). This performance can then be compared to the third injection method of shock-front injection, which introduces the penetration depth of a razor blade as an additional tuning parameter. (see section 8.3).

8.1 Self injection

In section 2.6 I have outlaid a density threshold for self injection for a certain laser pulse and target length. The same publication [9] emphasizes the importance of focal quality, which I have discussed in section 5.3. Evaluating equation 2.23 for a pulse duration of 25 fs, a target length of 2.5 mm, considering α =25% of laser energy contained in the focus and an effective laser energy of αE =0.45 J one obtains a threshold density of $6.3\times10^{18}e^{-}\mathrm{cm}^{-3}$. Using a nozzle with 0.27 mm throat and a 2 mm exit diameter, I observed a threshold type behavior at approximately

25 bar backing pressure, 2 mm above the nozzle (figure 8.1 **b)**). The gas jet model

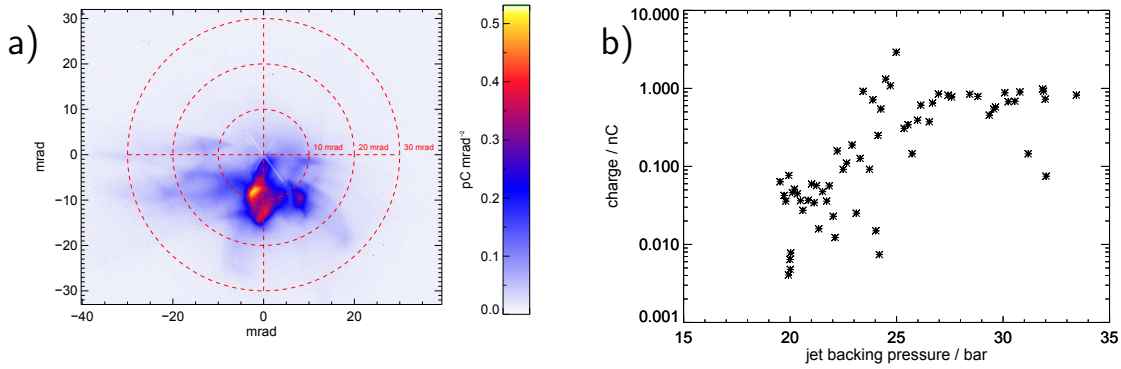

Figure 8.1: a) Typical self injected beam on forward screen. **b)** Charge as function of backing pressure for self injected beams

shown in section 4.1 yields a density of $4.9 \times 10^{18} e^{-}\mathrm{cm}^{-3}$ for these parameters. Another nozzle with a throat diameter of 0.52 mm and an exit diameter of 2 mm showed a similar behavior around 9 bar. This is the nozzle characterized in section 4.1 and the calibration yields a density of $6.5 \times 10^{18} e^{-}\mathrm{cm}^{-3}$ at 2 mm above the nozzle for this parameter set. This is a reasonable agreement with the theory, but the accelerated electron beams have a large divergence in excess of 15 mrad. For the remainder of the presented measurements I typically operated at densities below this threshold and used a gas mix of 2% nitrogen and 98 % helium to stimulate ionization injection or applied the shock-front method and used pure helium. These measurements show, that the beam divergence will decrease with decreasing plasma density and that the large divergence I observe with self injection at high densities is very similar to what one expects from extrapolation of this behavior.

8.2 Ionisation injection

The laser intensity thresholds required to reach certain ionization states of nitrogen and helium have been discussed in section 1.1. It was reasoned that nitrogen does not reach full ionization before the peak of the laser pulse is reached and some electrons may only become ionized in the laser peak. As the front edge of the laser pulse expels the plasma electrons and thus forms the plasma wave, the inner electrons of nitrogen can become ionized inside the bubble. As they become ionized in the decelerating part of the bubble, i.e. the first half of the bubble or the first quarter of a plasma wavelength behind the laser pulse respectively, they can slip into the accelerating part and become trapped. A continuous injection is expected, as long as a wake is formed and the laser intensity is high enough. Thus I can predict

that electron beams produced with ionization injection, will typically exhibit wide energy spread. As their initial position at ionization is undetermined within the volume of sufficient laser intensity, a uniform initial distribution throughout possible trapped phase space orbits is expected. In particular there will be no collective phase relation of the betatron oscillations, which determines the divergence of the accelerated electron beams. The divergence is thus expected to be smooth and represent the average momentum distribution of the betatron oscillations. Collective betatron phase effects will be presented in section 8.3.1 as observed in shock-front injected beams. As opposed to the shock-front method, the ionization injection method does not require the presence of super sonic gas flows. Hence I will present some electron beam measurements using a supersonic nozzle in section 8.2.1 as well as measurements using a subsonic gas cell type target in section 8.2.2. Results are compared in section 8.2.3.

8.2.1 Experiment: mixed gas with 2 mm jet

For this experiment I used the well characterized 2 mm jet nozzle with a 0.52 mm throat (type I) and a mixed gas of helium with a 2% addition of nitrogen. Only three pump lasers of the main amplifier were available and thus the pulse energy was $\alpha E = 0.30\,\mathrm{J}$. Parameters are listed in table 8.1. Starting at an electron density of $6 \times 10^{18} e^{-}\mathrm{cm}^{-3}$ I first observed scattered multiple beams on the forward screen. Shadowgraphy observations in Jena [69] indicated that multiple plasma waves are frequently created, but not necessarily have charge injected into them. It was expected that with lowered density or laser power, filaments will disappear. A lowered backing pressure will eventually cause dramatic boundary layer effects in the nozzle and I wanted to cover a wide density range. Thus the laser power was reduced and the high power attenuator was set to 75%, so that only single beams were observed 8.2 **a) - b)**. The pressure scan was performed by closing the connection between jet reservoir and gas bottle and then continuously shoot while the gas reservoir depleted. The data shown in figure 8.2 **c) - d)** is a binned representation from 143 shots, where standard deviations from each bin are plotted as error bars. I observed charge, divergence and beam peak energy decreasing with decreasing density. As the charge per solid angle on the forward screen reached a level close to the background noise, I increased the laser energy and continued to lower the backing pressure. For this measurement the forward screen was positioned in the beam path. Thus electron beam scattered on the components of the forward screen, but as it is shown in section 8.3.2 the beam does not loose significant energy in the process and the beams peak energy could still be obtained. The scattering on the forward screen increases the beam divergence and thus actually helps to obtain a reading from the electron spectrometer as the average electron beam centroid was 3 mrad above the laser axis. Thus I obtained the electron beam divergence, total charge and peak energy simultaneously as shown in figure 8.2. Charge, divergence and energy increase with increasing plasma density until

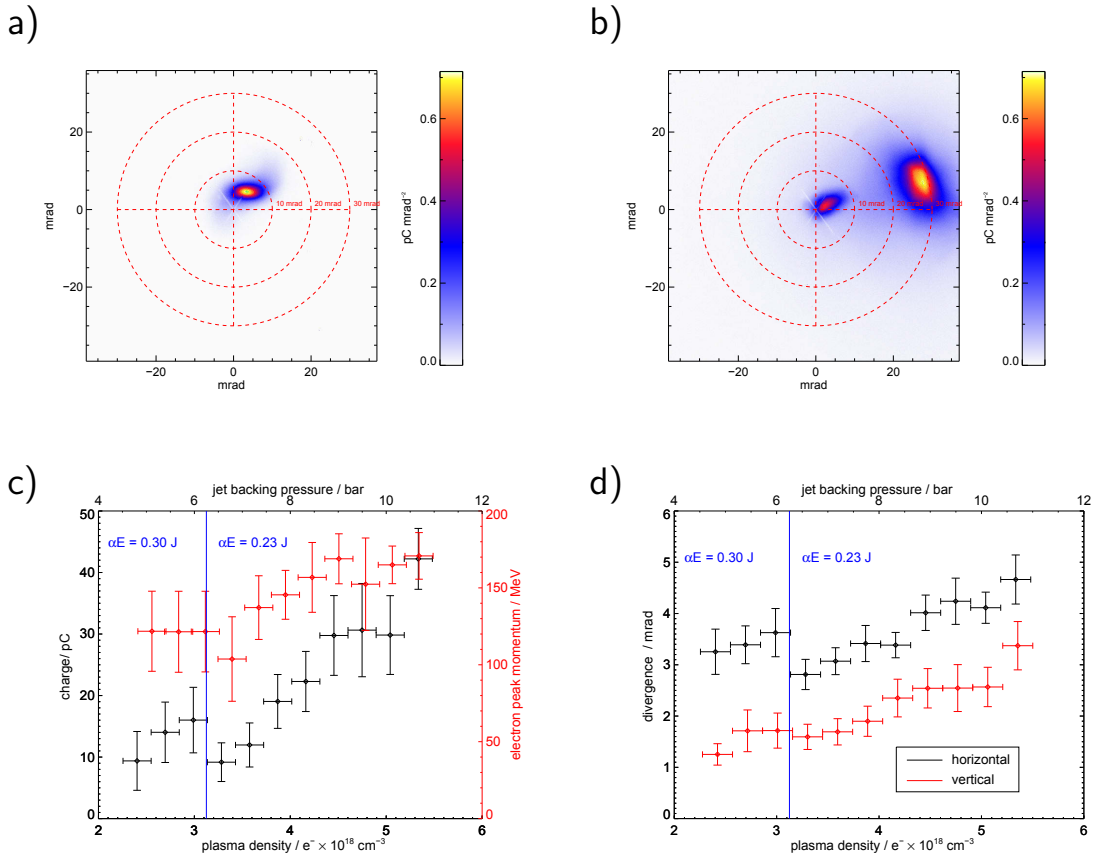

Figure 8.2: **a)** Typical ionization injected beam on forward screen. **b)** Multiple beams on forward screen at high plasma densities. **c)** Electron beam charge, peak energy and **d)** horizontal and vertical divergence as function of plasma density.

9 bar backing pressure, which corresponds to a plasma density of $4.5 \times 10^{18} e^{-}\mathrm{cm}^{-3}$. When at $3 \times 10^{18} e^{-}\mathrm{cm}^{-3}$ the laser pulse energy was increased by 25% the obtained divergence and charge became comparable to the situation at the lower laser pulse energy, but 25% higher plasma density. This indicates that ionization injected charge is $\propto I * N$, where I is the laser intensity and N the plasma density. The accelerated charge decreases approximately linear with density, but injection stops at a non zero density. Another density scan was performed after a large electron beam steering was compensated with gradient steering (see section 7.2). In this condition most of the electron beams were detectable with electron spectrometer and the density was scanned without the forward screen inserted. The electron energy as a function of density is plotted in figure 8.3. In this case the divergence and total charge were not measured. I see a similar effect compared to figure 8.2 as the electron energy peaks at a density $4.5 \times 10^{18} e^{-}\mathrm{cm}^{-3}$ and is proportional to the density below that.

Plasma		
Target type	super sonic CD nozzle jet	
Exit diameter	2 (1.7 eff.)	mm
Throat diameter	0.52	mm
Mach # (exit)	5.2	
Height over target	3.2 ± 0.2	mm
Gas	98 % Helium 2 % Nitrogen	
Laser		
Pump Lasers	3	
Laser energy	2.2 (max)	J
Pulse duration	25	fs
Parabola	f / 15	

Table 8.1: Parameters of the experiment presented in figure 8.2

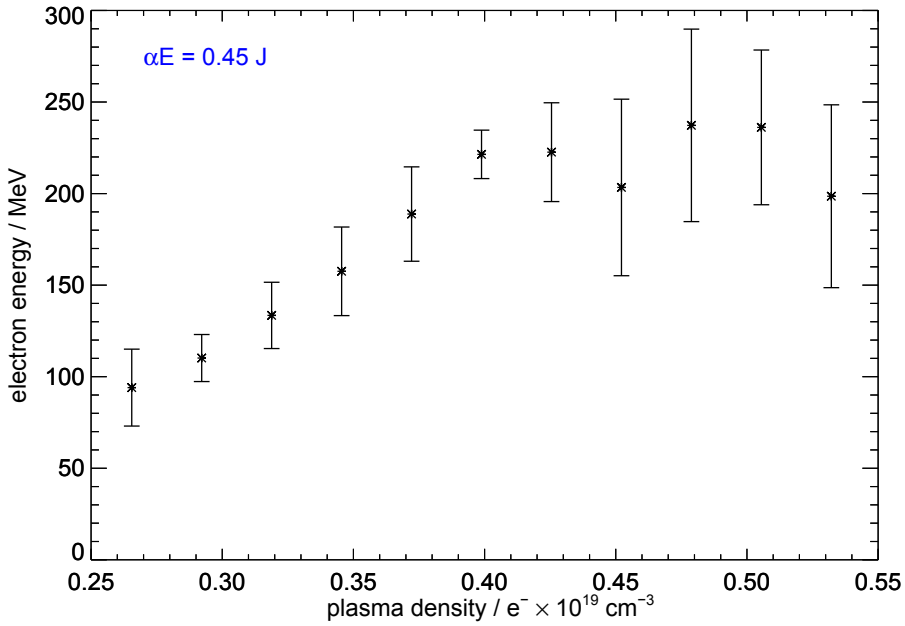

Figure 8.3: Electron peak energy as function of plasma density. Beam steering was corrected with strong gradient steering as shown in section 7.2.

8.2.2 Experiment: mixed gas in a gas cell

A gas cell target is essentially a gas container with two pinholes for the laser on opposing sites. The used design was inspired by S. Kuschel [7] and has observation

windows on top, left and right side of the container. The gas cell is mounted on top of the pulsed valve and the pinholes are mounted in a threaded plunger, so that the position of entrance and exit pinhole can be adjusted. The pinholes are 500 µm diameter channels drilled into a 500 µm thick ceramic disk. I found that, in order to achieve reasonable performance, the gas cell had to be aligned, such that the laser focus was located in front of the gas cell and partially in the pinhole channel. This implies that the gas extends to outside of the gas cell and a gas cone similar to that of the CD-nozzle is formed in front of the pinholes. This region is not accessible to interferometric observation and I don't have a model to analytically calculate the density in that region or the density in the gas cell. My analytical model for gas cones needs to assume an equilibrium state of the gas container. Variation of the delay of the pulsed valve and the laser showed, that even at the maximum delay of 5 ms the gas container did not reach such an equilibrium. The laser was then focused back to the center of the gas cell, where the observation windows allowed for an interferometric analysis of the plasma trace yielding an electron density of $(8 \pm 3) \times 10^{18} e^- cm^{-3}$ inside the gas cell at 1.36 bar backing pressure. The effective density at the interaction outside the gas cell is unknown, but probably less than $5 \times 10^{18} e^- cm^{-3}$. One may however assume, that the density scales linearly with the backing pressure. The measured charge and divergence on the forward screen as a function of backing pressure are plotted in figure 8.4 and reproduce what has been observed with the nozzle. Charge and

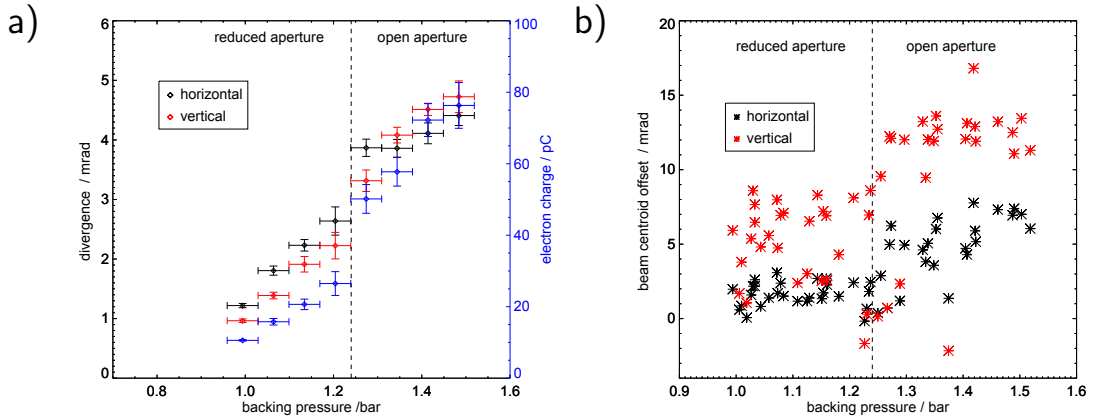

Figure 8.4: Charge and divergence as function of backing pressure for ionisation injected beams in a gas cell

divergence decrease with decreasing density. The forward screen measurements also revealed a strong beam steering of more than 10 mrad in vertical direction, possibly caused by vertical angular chirp. As it has been argued in section 7.3, the compressor gratings are not remotely tunable, such that vertical angular chirp could be compensated or introduced. In order to apply vertical electron beam

steering I used the aperture method as shown in section 7.1, with partial success (figure 8.4 **b)**). The reduction of laser energy caused a further reduction of charge, but also in divergence. This is in agreement with what has been observed in the case of the supersonic nozzle. At the lowest backing pressures I observed beams with less than 1 mrad standard deviation divergence and occasionally the electron beam pointing allowed for a measurement of the electron energy in the electron spectrometer. The forward screen was then moved out of the beam path and the spectra shown in 8.5 were observed. While taking these spectra I reduced the

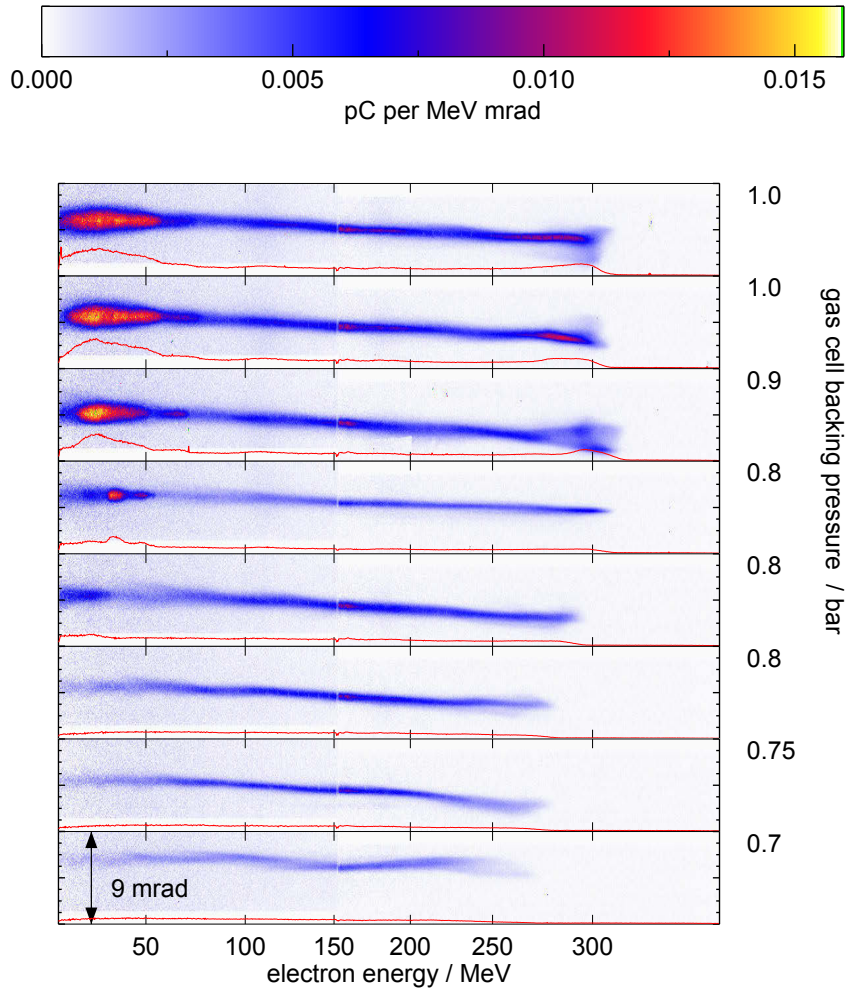

Figure 8.5: Spectra from the gas cell with decreasing density from top to bottom

backing pressure further until injection stopped. After restoring a higher backing pressure the beams reappeared. Notably are the parts at lowest and highest energy, which are more divergent and have a higher charge per MeV than at intermediate energies. Peak electron energies of 300 MeV are obtained. During the scan with the forward screen inserted, some shots created a signal in the electron spectrometer, non of which exceed 300 MeV. These spectra are too few, but indicate the peak energy increased, while the backing pressure was lowered. While the experimental conditions were not optimal in this case, some remarkable distinctions to the jet experiments could be demonstrated. The 300 MeV peak electron energy is the highest demonstrated peak electron energy, achieved with ionization injection. It was demonstrated close to a density threshold for ionization injection, which seems to depend on the laser energy. For the highest laser pulse energies the necessary low density could not be reached with the supersonic nozzle due to boundary layer effects.

8.2.3 Summary ionization injection

In both of the above presented scans, I observed that charge and divergence react in a similar fashion to changes in density and laser energy. Other experiments have seen a similar behavior as for example the publication by Pak *et.al.* [70] where the charge is presented as function of laser intensity. They only varied the laser pulse energy and found an intensity threshold for ionization injection and also a decrease in electron beam divergence with decreasing laser intensity. I have focused on a variation of the electron density and also found a threshold for ionization injection, where the threshold depended on the laser intensity. An interpretation of this behavior must necessarily include the product of laser intensity and plasma electron density. In equation 1.48 I introduced the critical power for self-focusing P_{crit}, which reappears as dimensionless scaling parameter P/P_{crit} in the LWFA theory. For a given pulse duration the parameter P/P_{crit} is proportional to electron density and laser pulse intensity. The work done by Sun et al. [71] shows that particularly the value of $P/P_{crit} = 1$ sensitively marks the onset of the formation of a cavitated ion column. Also in the work of W. Lu it is mentioned that $P/P_{crit} = 1$ marks the lower limit for wakefield acceleration as his model is based around the assumption of an electron void ion column. Extrapolating the data in figure 8.2 **a)** to the density where injection stops, we get $1.8 \times 10^{18} e^{-}\mathrm{cm}^{-3}$ for $\alpha E = 0.36\,\mathrm{J}$. Thus yielding that injection stops at $P/P_{crit} \approx 0.85$. Linearly extrapolating the behavior for $\alpha E = 0.28\,\mathrm{J}$ yields a density of $2.6 \times 10^{18} e^{-}\mathrm{cm}^{-3}$, at which injection would stop or $P/P_{crit} \approx 0.94$. In the work of Pak*et.al.* [70] the threshold is also to $P/P_{crit} = 1$. Their interpretation focuses on the abundance of delayed ionized electrons. With my findings it may be assumed that for the presented measurements the abundance of delayed ionized electrons exceeds the capacity of the wake to trap these electrons. The capacity of the wake structure would thus scale with P/P_{crit}, where electrons with increasing initial offset can be trapped as P/P_{crit} grows. If

the amount of charge trapped is only proportional to a volume from which particles can get trapped, than a maximum charge density in that region, possibly limited by space charge effects, is also implied. This hypothesis is further supported by the finding, that the maximum charge per solid angle seems to depend on the peak energy, which for ionization injection typically coincides with the energy spread. I used the data shown in figure 8.2 and plotted the total charge as a function of peak energy times horizontal times vertical divergence in figure 8.6. I see an approximately linear behavior with $0.021 \pm 0.003\,\mathrm{pC\,MeV^{-1}\,mrad^{-2}}$. As ionization injection occurs continuously this could imply that the rate at which electrons are injected is proportional to maximum initial offset, at which electrons can get trapped. In this context, it is useful to compare a non continuous injection method, which I will do in the next section 8.3. But first I want to draw some conclusions

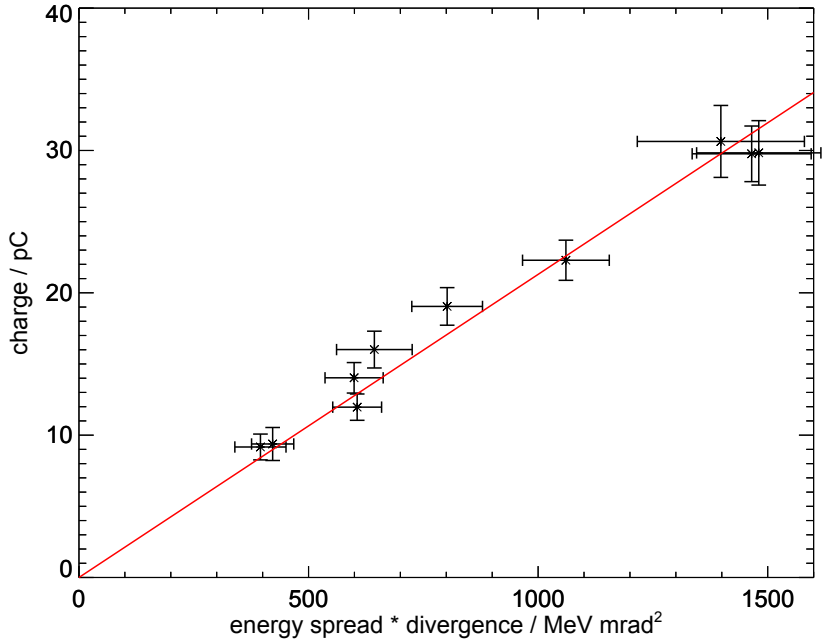

Figure 8.6: Charge as a function of peak electron energy times horizontal times vertical divergence from data of ionization injection.

regarding acceleration gradients and acceleration length. In the gas jet experiments with a 2 mm diameter gas cone it was found that the peak electron energy decreased with decreasing density and peak electron energies of $\approx 250\,\mathrm{MeV}$ were reached at $4 \times 10^{18} e^{-}\mathrm{cm}^{-3}$ plasma electron density. In the gas cell a plasma with more than 4 mm length was provided and after optimization a peak electron energy

of 300 MeV was reached. This indicates that the maximum acceleration length is close to 2 mm, which fits well with the Rayleigh length of $l_R = 1.13$ mm in our case and the acceleration length is likely $L_{acc} \approx 2l_R$. The peak acceleration gradient is approximately $\propto \sqrt{N\sqrt{I}}$ and does not introduce a strong variation of the peak electron energy. The dephasing length is $\propto 1/N^{3/2}$ and has much stronger influence on the peak electron energy, even at a fixed acceleration distance, as it determines the average acceleration gradient. The peak electron energy is plotted for an effective laser energy of $\alpha E = 0.54$ J and fixed acceleration distance or fixed electron density respectively in figure 8.7. In figure 8.7 **b)** the dephasing length is the point at which the peak electron energy as a function of acceleration length reaches a maximum for a given density. It can be seen that for an electron density of $4 \times 10^{18} e^- \mathrm{cm}^{-3}$ the peak electron energy is reached at ≈ 2 mm which coincides with our target length and $2l_R$. But figure 8.7 **a)** shows that the observed decrease of peak electron energy can not be explained assuming a fixed acceleration distance limited by diffraction. Thus I have to assume, that a decrease in plasma density reduces the acceleration length. All the presented measurements have not been performed with good flat top density distributions. The laser passed the nozzle either very high above the nozzle or on the edge of the gas cone. As I reasoned the existence of a lower density threshold for ionization injection above, it is reasonable to assume that the point of the first injection shifts towards the center of the density distribution as the overall density is lowered. Thus the maximum acceleration length is reduced with reduced density. For the maximum achieved peak electron energy the theoretical model fits reasonably well.

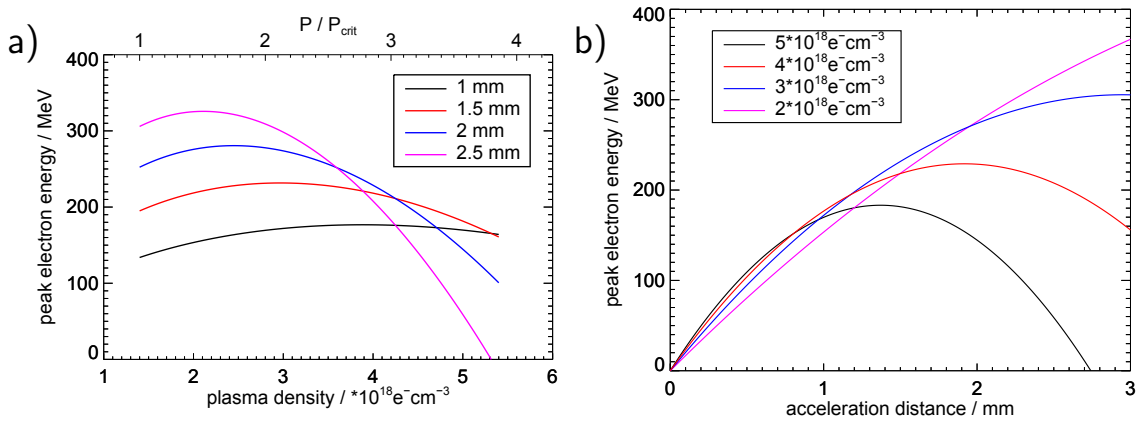

Figure 8.7: Theoretical prediction of the electron peak energy for varying plasma density (a) and varying acceleration distance (b) at a laser energy of $\alpha E = 0.54$ J

8.3 Shock-front injection

The method of shock-front injection adds an additional tuning parameter to the experiment. The work done by Schmid *et al.* [11] and Buck *et al.* [15] suggests that with this method a singular injection event can be produced at the crossing of the laser with the shock front. By varying the shock-front position within the jet, the remaining target length can be adjusted and thus the evolution of the injected electron may be studied. Two nozzle are compared in order to study the influence of the Mach number. The first is a type I nozzle of 2 mm exit diameter and a 0.52 mm throat, identical to the one used in section 8.2.1. For this nozzle the shock angle as function of razor blade penetration depth was measured in section 4.3. This nozzle has a Mach number of 5 at the nozzle exit. The second nozzle (type II) has and identical exit diameter of 2 mm, but a throat diameter of 0.27 mm, yielding a Mach number of 9 at the nozzle exit. At accordingly adjusted backing pressure it produces a similar density profile to the first nozzle. During the experiment the position of the shock front was visible in the plasma trace obtained by interferometric imaging. I chose to pass the laser beam at only 1.4 mm above the nozzle exit in order to obtain a density distribution close to a flat top. The backing pressure was then reduced to the point where a shortening of the plasma trace was observed, indicating the presence of boundary layer effects. Thus the obtained density of $(4.0 \pm 0.5) \times 10^{18}\,\mathrm{e^-\,cm^{-3}}$ for the type I nozzle and $(3 \pm 1) \times 10^{18}\,\mathrm{e^-\,cm^{-3}}$ for the type II nozzle were the lowest reasonably possible densities close to the nozzle exit. A summary of the nozzle and laser parameters is listed in table 8.2.

For neither of the nozzles an electron signal was detected, when no shock front

Plasma			
Target type	super sonic CD nozzle jet		
Exit diameter	2	2	mm
Throat diameter	0.52	0.27	mm
Mach # (exit)	5.0 ± 0.5	9.0 ± 1	
Height over target	1.4 ± 0.1	1.6 ± 0.1	mm
Plasma density	4.0 ± 0.5	3 ± 1	$\times 10^{18} e^- cm^{-3}$
Gas	100 % Helium		
Laser			
Pump Lasers	4		
Laser energy	3.0 (max)		J
Pulse duration	25		fs
Parabola	f / 17.5		

Table 8.2: Parameters of the shock-front experiments

was created. Then electron spectra were measured, while the penetration depth

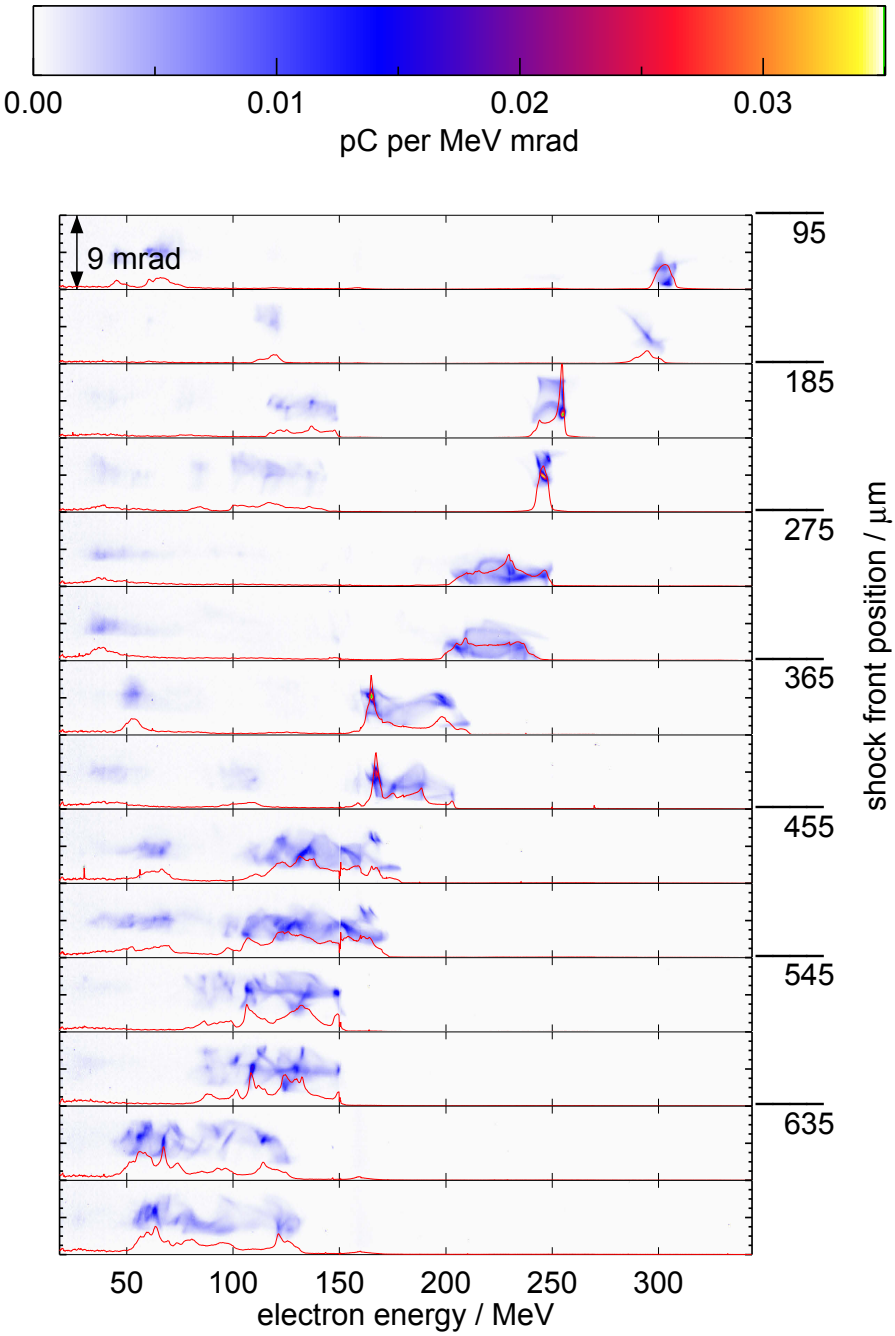

Figure 8.8: Selection of spectra from a razor blade scan as summarized in figure 8.9 **a)**

of the razor blade was changed. A selection of spectra from the type I nozzle at different shock positions is shown in figure 8.8. For a small razor penetration these spectra show narrow energy spread at high electron energies. As I increased the razor blade penetration these spectra became increasingly broader, while the peak energy decreased. The decrease in peak energy is expected, as the distance between the point of injection and the end of the plasma target is reduced, which reduces the acceleration distance. The increasing energy spread was not predicted by the earlier work. The widened spectra exhibit sharp cut offs at the higher and the lower end. The average high and low energy cut offs as function of the razor blade position are plotted in figure 8.9 **a)** for the type I nozzle. Within that energy range the spectra show some variations of higher and lower charge per solid angle and energy interval. If the longest acceleration length is on the order of the dephasing length I expect that electron peak energy changes only little with the acceleration length, because the acceleration gradient should be small near the dephasing limit. What I observe is the opposite as the observed maximum electron energy reacts sensitively to changes in shock-front position, when the acceleration length is still long. The

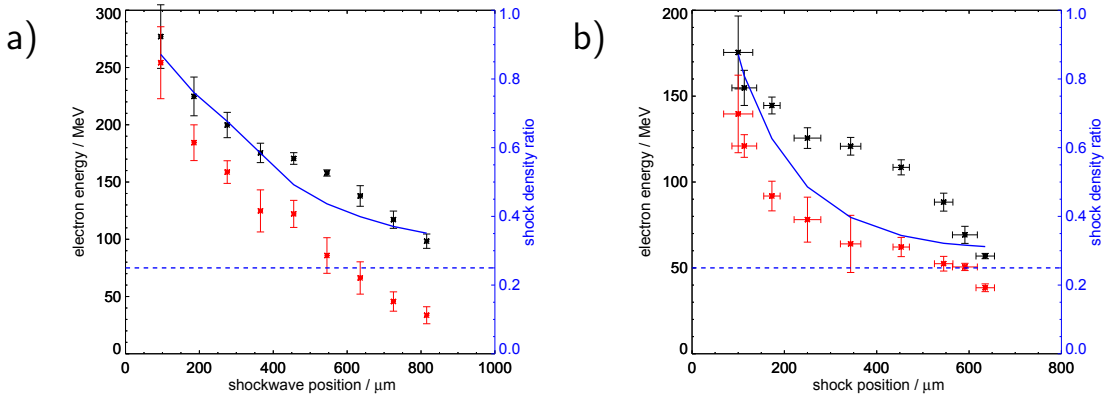

Figure 8.9: Scan of electron beam energy high cut off (black) and low energy cut off (red) as a function of shock-front position over a 2 mm jet nozzle. **a)** Type I nozzle **b)** Type II nozzle. The approximate shock density ratio is illustrated in blue.

increase in energy spread and the reduction of peak energy with an increased razor blade penetration is also observed with the type II nozzle in even exaggerated form (see figure 8.9 **b)**). The energy spread reacted so sensitive to small changes of the penetration depth, that it was not possible to reproduce the very narrow energy spectra obtained with the type I nozzle. On the other hand I observed very little variations in the electron spectra, when the shock-front position reaches $\approx 300\,\mu m$ distance towards the nozzle center measured from the nozzle edge. As the density distribution was similar and only the Mach number was changed, it must be concluded that the shock-front is formed differently in the two cases. The Mach

number can not affect the LWFA other than by introducing a change in the created shock front. The density transition ratio has been introduced in equation 4.12 and asymptotically converges towards 1:4 for high Mach numbers in Helium. Combined with the fact that the effective Mach number $M_\phi = M \sin \phi_M$ is given by the shock angle ϕ_M, one can estimate the density transition as shown in blue in figure 8.9 (dashed blue line). For low Mach numbers at nozzle exit the density transition ratio is approximately $\propto \sin \phi_M$, while for high Mach numbers the asymptotic limit is quickly reached at small shock angles and small razor penetration depth. The qualitative behavior of the transition ratio in high and low Mach number gas jets matches the qualitative difference, at which the energy spread increases and peak energy decreases in the high and low Mach number case. The experiment with the type I nozzle was repeated with the forward screen inserted into the beam path. Thus I could observe the beam divergence, total charge and width of the energy spectrum simultaneously. The result is plotted in figure 8.10. The first observation is, that the total charge increases with increasing razor blade penetration or shock transition ratio respectively. The sensitive decrease in peak electron energy may thus be caused by beamloading due to the increase in total charge .This effect has been shown by Rechatin *et. al.* [48] where they used colliding laser pulse injection to control the amount of injected charge. What they observed was a reduction from 200 MeV to 170 MeV peak electron energy as they varied the charge from 8 pC to 38 pC. They also observed a significant widening of their energy spread, despite the injection being strongly localized. There is a chance that the highly localized laser pulse collision as well the highly localized density transition may trigger injection, such that a continuous injection over a certain distance behind the location of the trigger is caused. However, I am not aware of any reported evidence for such a process. It will thus be assumed that all detected charge was injected quasi-instantaneous. In this case there are two distinctive scenarios, in which a widening of the energy spread can be explained. For once, the injection may change such that the initial distribution of electrons leads to different energy gains. For example, a fraction of the injected electrons may be injected closer to the bubble center (dephased) and thus experience a different average acceleration gradient than electrons injected closer to the back of the bubble. The second scenario is that the interaction of accelerated electrons with each other is the dominant factor, such that some electrons shield other parts of the bunch from the accelerating fields of the wake. This is the same as beamloading and Rechatin *et. al.* [48] have performed PIC simulations to identify the dominant effect, but could not conclusively demonstrate a dominance of one effect over the other. In the previous section I have already demonstrated that the charge emitted per energy interval is not independent of the charge emitted per solid angle. What has been observed is, that for little razor blade penetration the beam divergence does not change and the total charge is proportional to the absolute energy spread. At a shock-front position of more than 300 µm the accelerated charge increases strongly, coincidentally with the electron beam divergence. Thus I plotted the

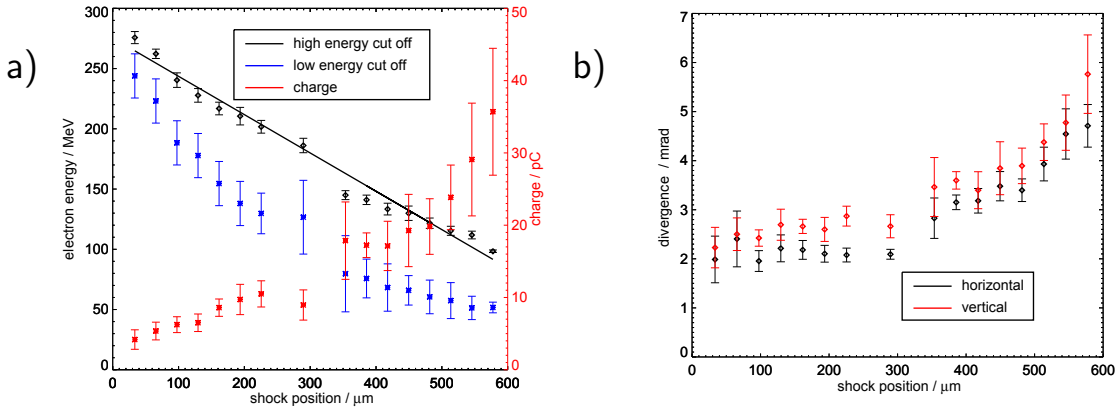

Figure 8.10: Scan of electron beam energy and charge **a)** and horizontal and vertical divergence **b)** as function of shock-front position over the jet

total charge as a function of absolute energy spread and electron beam divergence as shown in figure 8.11. In section 8.2.3 we have shown the same plot for ionization injection in figure 8.6. For the shock injection I obtain a linear behavior with a nearly identical slope of $0.024 \pm 0.002\,\mathrm{MeV}^{-1}\,\mathrm{mrad}^{-2}$ compared to the $0.021 \pm 0.003\,\mathrm{MeV}^{-1}\,\mathrm{mrad}^{-2}$ for ionization injection. Since both injection types have a very different underlying mechanism, it seems that the amount of charge accelerated into a solid angle within an energy interval is limited by the capacity of the wake structure. It must be noted that the comparable values for both injection types may largely depend on the fact, that the plasma-vacuum interface was identical in both cases. Golovin *et al.* [72] has shown that the normalized transverse emittance and thus the divergence of the emitted electron beam strongly depends on the particular shape of the plasma-vacuum interface. Generally a weaker gradient at the exit of the plasma causes less increase of the electron beam emittance. This is also likely the reason for the very small electron beam divergence that has been observed in the gas cell experiment. With comparable extraction the shock-front method does not show an advantage over ionization injection in terms of charge per energy interval and solid angle. For a possible application of the electron beam this is typically the most important parameter. One may use ionization injected beams and a combination of magnets and apertures in a filtering configuration to obtain the desired divergence and energy spread by filtering from a broad band electron beam with large divergence. From what I have measured the usable charge for the application would remain the same. But the razor blade injection can offer a controlled way to adjust the total charge injected. In the current setup the transition ratio always changes simultaneously with the acceleration length. It might be possible to build a plasma target, where the acceleration length behind the shock front can be varied independently from the razor blade penetration depth.

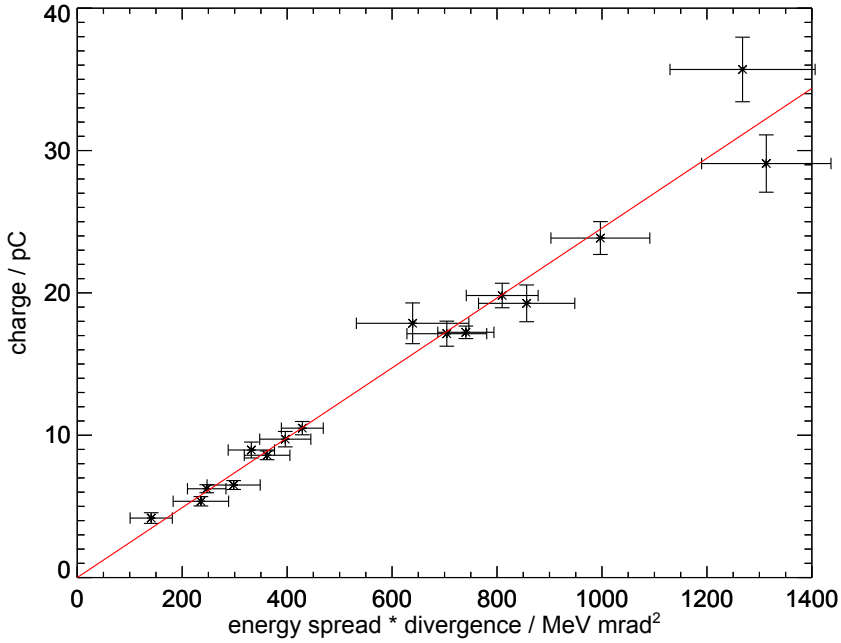

Figure 8.11: Charge as a function of energy spread (foot width) times horizontal times vertical divergence from data of shock-front injection.

Thus the acceleration of high charge electron bunches may be compared to those of low charge electron bunches at a varying acceleration length.

8.3.1 Oscillatory modulations in the electron spectra

The electron spectrometer measures electron dispersion due to their energy in one direction and their divergence in the other direction. Thus it was possible to observe angular modulations as a function of electron energy. One expected type of modulation is the betatron oscillation. As electrons can get injected with an initial transverse momentum or at an offset with respect to the bubble center they undergo oscillations with the plasma frequency. As electrons get accelerated, the relativistic mass gain influences the frequency and thus I expect from equation 1.13 modulations with a betatron frequency $\omega_\beta \propto \omega_{pl}\sqrt{\gamma}$. And indeed I observe modulations in our spectra with increasing periodicity. A selection of spectra are shown in figure 8.12. We observe that the charge is often divided into two different streams, likely caused by injection from two opposing sides into the bubble. Frequently I observe one full period of oscillation at an interval of 40 MeV between 50 MeV and 100 MeV. Assuming an acceleration gradient of 200 GeV per meter this yields a betatron period $\lambda_\beta \approx 200\mu m$. With an average $\gamma \approx 150$ around an electron energy of

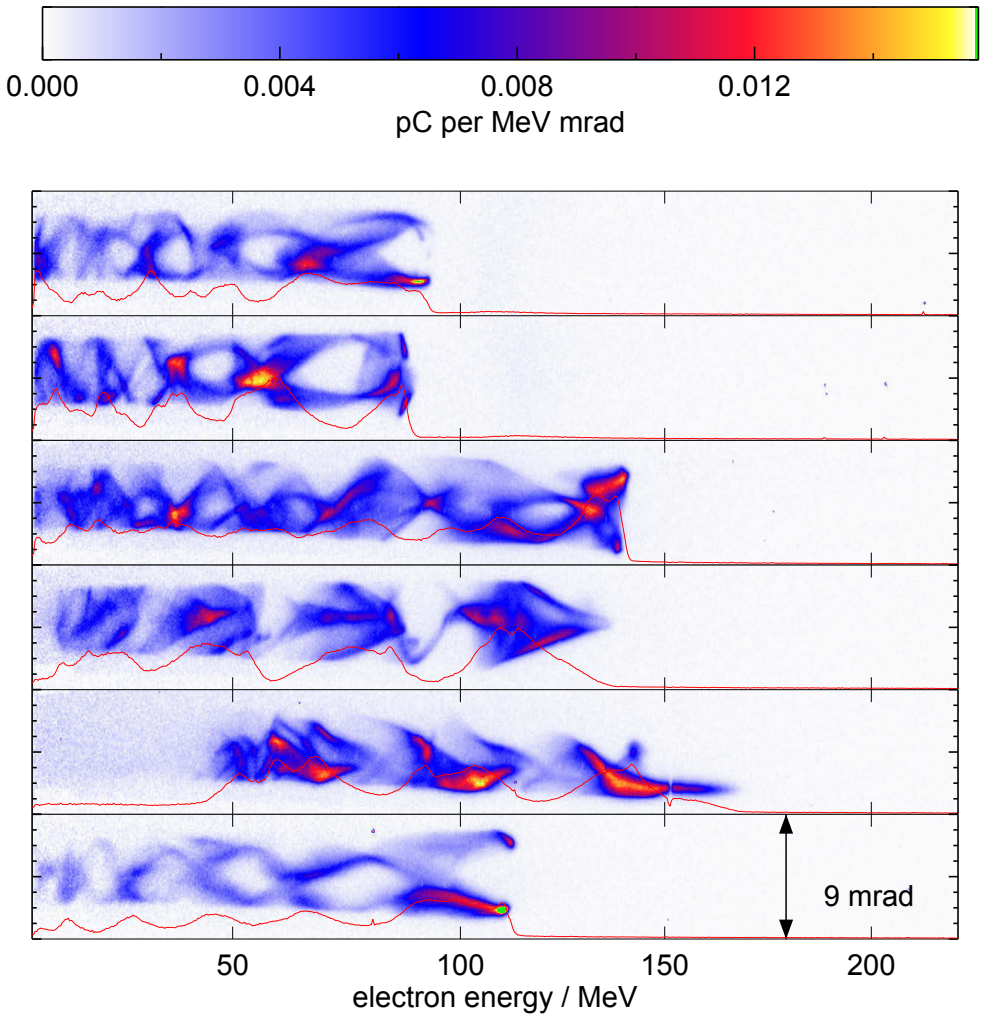

Figure 8.12: Selection of modulated spectra from different razor blade experiments.

75 MeV this yields via $\lambda_\beta = \sqrt{2\gamma}\lambda_{pl}$ a plasma wavelength of 12 μm corresponding to $7.8 \times 10^{18} e^- cm^{-3}$ plasma density. As I argued above the peak acceleration gradient is up to a factor of 2 higher than the average acceleration gradient. Because the density $N \propto 1/\lambda_{pl}^2$ this method is very sensitive to the measured acceleration gradient and thus the result is within a reasonable range. High amplitude betatron oscillations typically also imply an increase of emitted betatron radiation [28]. The use of betatron radiation is one of possible applications for LWFA as shown by Cole *et al.* [73].

8.3.2 Small energy spread and injection rate

In figure 8.10 **a)** an in figure 8.9 it was shown that at a small penetration depth of the razor blade narrow electron energy spreads at high electron energies can be observed. I carefully adjusted the razor blade to the minimum penetration depth at which electrons were still injected and obtained spectra as shown in figure 8.13. The first spectrum was taken, while the forward screen was inserted. The corresponding image of the forward screen is shown in figure 8.14. I achieved an electron energy

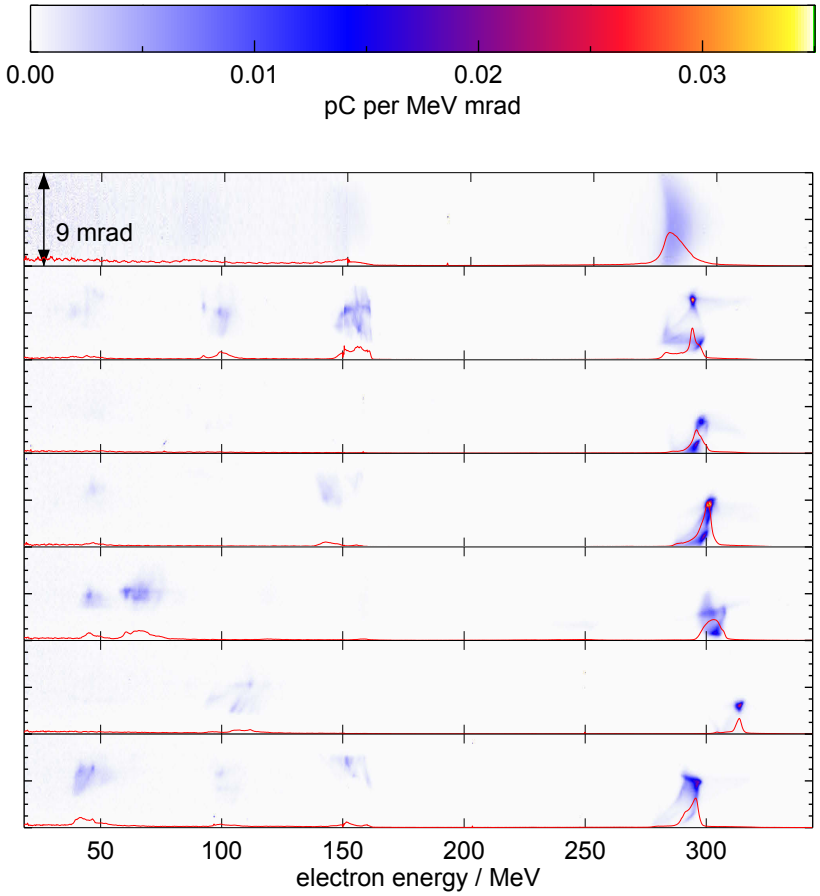

Figure 8.13: Selection of narrowest energy spectra. The first shot is taken with inserted forward screen.

of ≈300 MeV which is the same peak energy obtained from ionization injection in the gas cell (see section 8.2.2). For the case of the inserted forward screen the measured energy spread is consistent with the calculated resolution limited by

the entrance aperture of 12 MeV. When the forward screen is removed the energy spreads vary from 10 MeV down to 3 MeV. Those are likely limited by the electron beams divergence, which was 2 mrad on average and thus smaller than the 4 mrad acceptance angle of the electron spectrometer. I also observed that these high energy electron bunches typically occur in pairs. That the shock-front injection produces this kind of symmetric injection was already shown in the last section, where in figure 8.12 two oscillating streams of electrons were shown. The occurrence of two electron bunches at small energy spreads, would be expected if one took a narrow energy interval slice from these spectra. Dominantly the energy spread is given by the separation of these two bunches, where angular and energy separation could not be distinguished. The measured spectra with the lowest energy spread of 3 MeV show only one bunch (second to last spectrum in figure 8.14), where I have to assume that the second electron bunch did not pass the spectrometer aperture. In conclusion I can state that energy spread is resolution limited and that two bunches with less than 1% energy spread are demonstrated. The overall energy spread may also be at less than 1%, but can not be resolved. The publication by Buck *et.al.* [15] indicated, that a small absolute energy spread 3 MeV can be preserved during the acceleration in LWFA and thus that relative energy spreads of less than 1% can be expected, if the electron beam is accelerated in excess of 300 MeV. As I have demonstrated their method of studying the evolution of small energy spread beams, is not an independent variation of the acceleration length at constant injection condition. But it is not very likely that a small energy spread evolves from a wide energy spread during the acceleration. If a continuously injected bunch reaches the dephasing limit, the front of the electron bunch can be decelerated, while the trailing end is still accelerated. If the acceleration is stopped at this point by the end of the plasma target, this effect may compress the energy spread by a factor of two. My finding that the charge density of the emitted electron beams in terms of charge per energy interval and solid angle is constant is one indication, that such a compression is not how small energy spreads occur. I can thus confirm the statement by Buck *et.al.* that an LWFA is capable of maintaining energy spreads as small as 3 MeV. To the best of my knowledge, the here presented electron bunches have the highest currently achieved mean energy of such narrow bandwidth electron bunches. At 300 MeV this is twice as high as the previously demonstrated energy of 150 MeV [15].

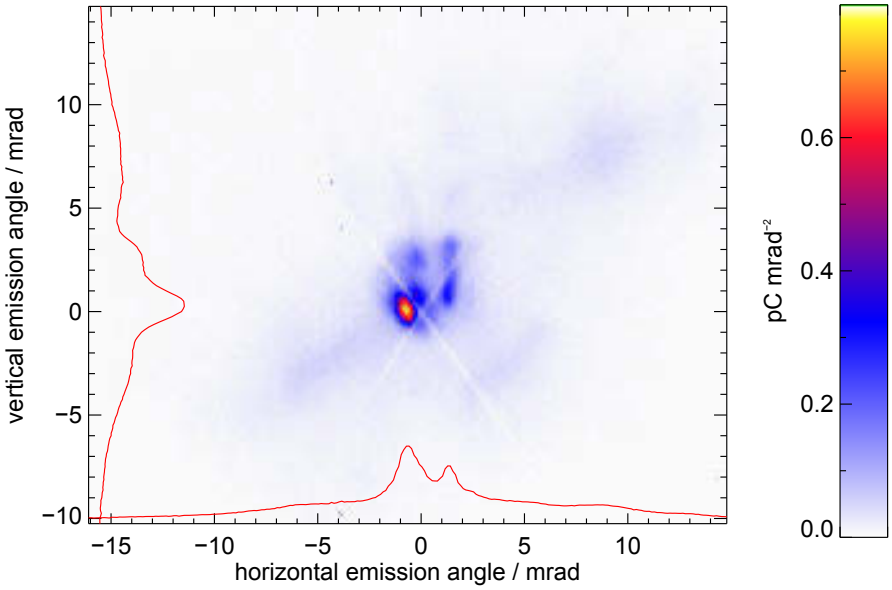

Figure 8.14: Image from the forward screen corresponding to the first shot in figure 8.13

Conclusion

A setup for electron acceleration using laser wakefield acceleration in the blowout regime was demonstrated. The accelerator was typically operated at densities above $2 \times 10^{18} e^- \mathrm{cm}^{-3}$, in order to fulfill the criteria $P/P_{crit} > 1$ and below $6 \times 10^{18} e^- \mathrm{cm}^{-3}$ to avoid self injection. In the absence of self injection, it was possible to study and compare ionization injection and shock-front injection, as two distinctively different mechanisms of electron injection. The injection method determines the energy distribution of the accelerated electron beam. In the course of this work, it was investigated if one injection method gives an advantage over the other regarding the charge per energy interval. The charge per energy interval is one of the key parameters when considering the possible applications of LWFA accelerated electron beams.

The ionization injection method was applied by using a gas mix of 2% nitrogen and 98% helium to form the plasma. The inner electrons of nitrogen can become ionized inside the wake and potentially become trapped. A peak electron energy of 300 MeV was reached and the charge was typically uniformly distributed from the peak energy to the lowest detectable electron energy. An electron beam pointing of 2 mrad was demonstrated. The beam divergence and charge increased with the laser energy and the plasma density, starting at a threshold of $P/P_{crit} \approx 1$. The highest demonstrated charge with stimulated injection in a single electron bunch of 80 pC coincided with an electron beam divergence of 4.5 mrad standard deviation. At the smallest demonstrated electron beam divergence of 1 mrad standard deviation, the electron bunches contained less than 10 pC of charge. It was furthermore shown, that the charge per solid angle is correlated to the electron peak energy, which for the observed ionization injected beams coincided with the energy spread. It was found, that for the observed beams, produced with one particular nozzle, the electron beams exhibit a constant charge per solid angle and energy interval of $(0.021 \pm 0.003)\,\mathrm{pC\,MeV^{-1}\,mrad^{-2}}$. The threshold of $P/P_{crit} = 1$ coincides with the threshold for the blowout regime [71], i.e. the point at which an electron void ion column is formed behind the laser pulse. It was concluded that a blowout region is necessary in order to trap electrons from delayed ionization. The correlation between P/P_{crit} and the total injected charge above the threshold also indicates, that the capacity to trap electrons depends primarily on the formed wakefield and to a lesser degree on the abundance of delayed ionized electrons in the presented

case. The method was then used to investigate the frequently occurring steering of electron beams, which occasionally reached values in excess of 20 mrad for the electron beam centroid with respect to the laser axis. It was demonstrated that this effect was dominantly caused by angular chirp of the laser beam.

The second studied method was shock-front injection, which is expected to cause a quasi instantaneous injection of electrons. A sharp razor blade edge was used to disturb the flow of a super sonic nozzle. Such a disturbance of a supersonic flow causes a density transition region called a shock-front. In this narrow transition region the structure of the wakefield is expanding quickly, trapping electrons inside the wake in the process. The density ratio in the transition region depends on the Mach number at the shock front and the angle of the shock front with respect to the flow. With the low Mach number nozzle electron beams with less than 5 MeV energy spread and a peak energy of 300 MeV have been demonstrated, which coincides with the resolution limit of the electron spectrometer at this electron energy. To the best of my knowledge this was the highest peak energy demonstrated, where the shock-front injection produced electron bunches with low energy spread. As the penetration depth was increased to vary the shock-front position an increase in total charge was observed, but also a wider energy spread. At small razor blade penetration the induced decrease of the electron peak energy, was higher than what was expected from the change of acceleration length or from the theoretically predicted acceleration gradients [2] respectively. The increase in charge and energy spread, as well as the decrease in peak electron energy was more sensitive to small changes in razor blade penetration depth in the case of the high Mach number nozzle. The density at nozzle exit was similar in both cases. The density transition ratio in the shock front does behave such, that for high Mach numbers the density transition ratio increases quickly and saturates at small razor blade penetration, while it increases more gradually for nozzles with a small Mach number at the nozzle exit. As a possible interpretation it was proposed that the injected charge increases with increasing density transition ratio and that the decreased peak electron energy and the increased energy spread are a consequence of the increased charge.

A decrease of electron peak energy with increasing injected charge was observed by Rechatin *et.al.* [48] using colliding pulse injection. It was linked to the collective effects of the injected electrons on the wakefield called beamloading. They also observed that the energy spread of the charge they injected, increased as the total charge increased. They could not conclusively proof, that the increase in energy spread is necessarily a consequence of the increased charge. In case of the razor blade experiment it is possible, that at the shock front a continuous injection up to a certain distance behind the shock may be triggered. For the nozzle with lower Mach number energy spread, total charge, and divergence have been measured simultaneously. The charge accelerated per energy interval and solid angle shows the same relation that was previously obtained for ionization injection. Both measurements rely on entirely different injection mechanism, but an identical nozzle

has been used. The data for both measurements is shown in figure 8.15 and the rate obtained by linear regression is $(0.021 \pm 0.001)\,\mathrm{pC\,MeV^{-1}\,mrad^{-2}}$. This strong correlation indicates, that the capacity of the wakefield to trap or maintain electrons within a certain energy range is indeed limited, but the transverse dynamics have to be taken into account. It must be noted that the beam divergence also strongly depends on the extraction of the electron beam at the plasma vacuum interface after the acceleration [72], hence it was important to only compare results from an identical nozzle. To the best of my knowledge electron beam divergence or emittance respectively have thus far not been considered in the context of a limited charge capacity. Regarding future applications the charge per energy interval and solid angle is similar for both injection methods and a peak electron energy of 300 MeV could be obtained with both methods. But in the case of the ionization injection it was possible to produce large divergence beams, with a higher charge per energy interval. Using active plasma lensing [74] it is possible to deliver the electron beam to the application regardless of divergence [7].

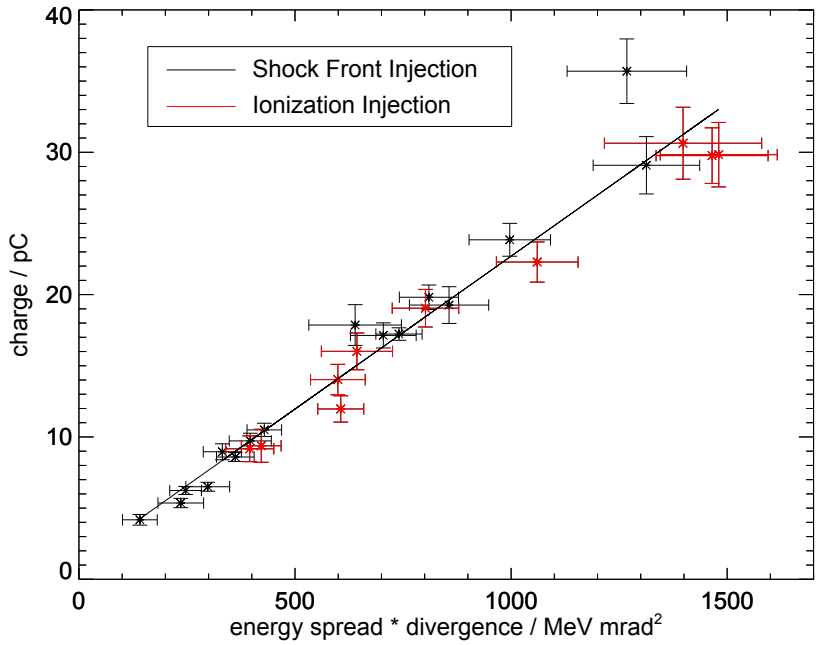

Figure 8.15: Total charge as a function of energy spread times horizontal times vertical divergence. The results from the razor blade experiments are plotted in black and the results from the ionization injection experiments are plotted in red.

The work done by Buck *et al.* suggested that the razor blade experiment can be used to vary the acceleration length, while the injection remains unaffected.

Thus the evolution of the acceleration gradient could be obtained. The presented measurements show that the injection is affected at higher Mach numbers and the experiment can only be used in the suggested way if the Mach number at nozzle exit is small and the shock angle is changed by small amounts. Instead I suggest that the razor blade experiment can be used to control the injected charge. In the case of the low Mach number nozzle the diameter ratio was 1:4 and narrow energy spread and presumably quasi instantaneous injection could be achieved. The second nozzle had a diameter ratio of 1:7.5 and small energy spreads could not be obtained, as the charge and energy spread reacted to sensitively to changes of the penetration depth. An intermediate ratio may be used to control the energy spread and charge with the penetration depth, while the acceleration length would have to be controlled by other means. This probably makes another gas source like a second nozzle or connected gas cell necessary. The challenge with such a target is the coupling of the gas flow in order to avoid significant gradients at the transition between the flow of different sources. Intersecting supersonic flows do also create high gradient phenomena similar to a shock front [54]. Lastly the flow from the second source may disturb the formation of the shock front in the first source. Gonsalves *et.al.* [13] have demonstrated a target configuration, where a super sonic nozzle was incorporated into a discharge waveguide. In this case the injection was stimulated due to an extended down gradient in the super sonic region and a stable production of electron beams with 10% energy spread was demonstrated. The method significantly improved the performance compared to waveguide without stimulated injection. Several other groups have demonstrated plasma target configurations with multiple flow sources. A two chamber gas cell has been demonstrated by Pollock *et al.* [14]. Double jet experiments have been shown by Hansson *et al.* [45] and recently by Golovin *et al.* [72]. All these experiments have either used extended downgradients or ionization injection to stimulate electron trapping. The only other currently available method, that is expected to create a quasi instantaneous injection is the colliding pulse injection as presented by Faure *et al.* [12]. If it is assumed that the shock-front injection occurs quasi instantaneous, even when wide energy spreads are observed, then a combined target with a shock-front injector will reveal a better insight into the underlying physics, than continuous injection methods could. In particular the optical probing techniques demonstrated by Buck *et al.* [75] and A. Sävert *et al.* [69], may be used to determine the length or timescale respectively, over which electrons are injected. I hope that the presented thesis will prove helpful in future investigations of the shock-front method and that the observed correlation between transverse dynamics and charge capacity will lead to a better understanding of the electron beam dynamics in laser wakefield acceleration.

Part IV

Appendix

A Calibrations

A.1 Incidence angle correction for scintillator screens

While measuring electron momenta we observed, that charge accelerated to higher energies typically appears brighter in the raw image data of our magnet spectrometer. The work done by K. Nakamura mentions that incidence angle into the LANEX has to be taken into account by assuming that the light yield increases linearly with the path length through the screen. Thus in order to calibrate the charge correctly we have to divide the light yield at a given position on the screen by $\sin \alpha_{inc}$. From the trajectory simulation used to calibrate the magnet spectrometer 6.3 we can obtain these incidence angles as function of screen position and thus calculate the correction as plotted in figure A.1. At 300 MeV the screen is

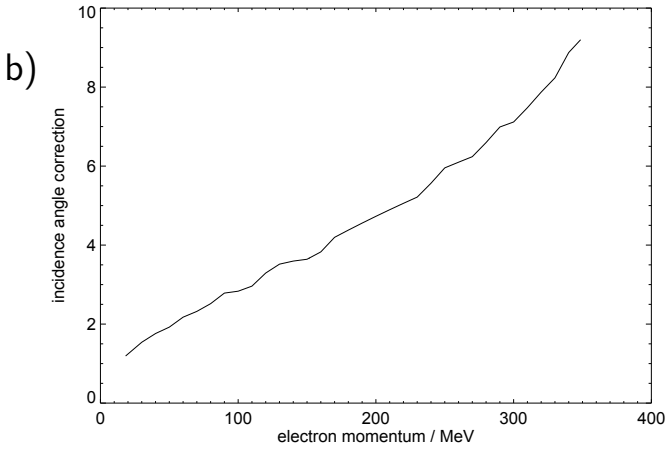

Figure A.1: Correction factor for incidence angle into LANEX screen as a function of electron momenta or position on the screen respectively

hit at incidence angles as low as 10 degrees and it might be questionable if a linear increase of light yield with path length is applicable. But we do obtain a constant injection rate for all energies, which is a reasonable justification for this method. While it may generally not be recommended to place the screen at too little angles

with respect to the electron trajectories, this screen position is typically chosen along the focal plane. For most magnet spectrometer designs this will force small incidence angles at high electron momenta. But if the path length dependence is not taken into account, this might easily lead to an overestimation of accelerated charge by a factor 5 or higher.

A.2 Density map from interferometric measurements

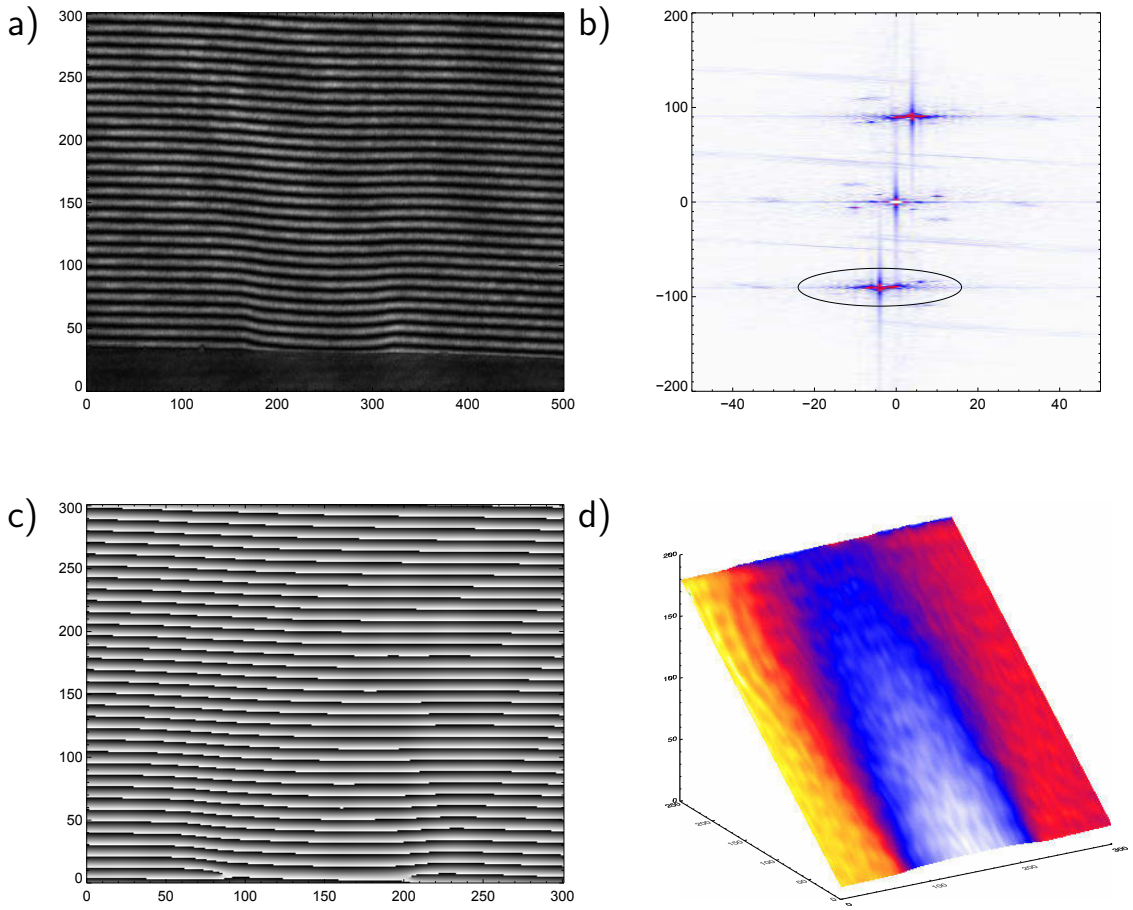

Figure A.2: Step by step illustration of data analysis used to extract the phase shift from interferometric imaging. **a)** original image. **b)** Fourier space with filter (black ellipse). **c)** phase wrapped. **d)** unwrapped phase with signal encoded

Our measurements of gas or plasma density are typically obtained using interferometry. This method measures phase shift introduced by a difference in index

of refraction for different parts of the laser beam. A detailed description of the necessary steps was given in section 4.4 and the analysis of a plasma trace, caused by a high power laser beam in a low density helium plasma, was discussed. The characterization of the type I nozzle was also performed using interferometry and using Argon at higher density. For one of these measurements the analysis steps are illustrated in figure A.2. From the original image **a)** the relevant part is cropped and a filter, marked by the black circle, is applied in Fourier space **b)**. From the back transformed image only the phase information is extracted **a)**. After unwrapping the phase shift, due to changes in index of refraction, is encoded on top of the phase shift, introduced by the tilt angle of the interferometer arms **d)**. The tilted plane must be subtracted using a reference phase or by appropriate fitting of the plane angle.

A.3 Angular chirp measurements

In chapter 7 it was shown how angular chirp in the laser can steer the electron beam. Thus it was attempted to measure the angular chirp of the laser using a method proposed by Varju *et al.* [61]. An interferometer is set up, where in one arm the beam is flipped in the direction, where the two interferometer arms are tilted with respect to each other by an angle ϵ. The resulting fringe pattern is then analyzed with a spectrograph, showing the imaged fringe pattern in one direction and the wavelength in the other direction. The distance between two fringes Δ_f is related to the angle by

$$\epsilon = \frac{\lambda}{\Delta} \tag{A.1}$$

with the laser wavelength λ. For longer wavelength the fringe distance increases as seen in figure A.3 **a)**. For every row the distance of fringes is fitted using the unwrapping method shown in the previous section A.2 as shown for 770 nm to 830 nm in 10 nm steps in A.3 **b)**. The results of the linear regression of the unwrapped rows as function of the wavelength is shown in figure A.3 **c)**. To obtain ϵ for a given wavelength, the result for every row has to be divided by the respective wavelength as shown in figure A.3 **d)**. In this step one can obtain deviations from the introduced tilt angle, which are caused by the different propagation direction of wavelength, due to flipping of the respective interferometer arms. The setup was tested by introducing angular chirp with wedged glass plates. It was found that BK7 introduces $3\,\mu\mathrm{rad\,nm^{-1}}$ per 10° wedge angle. The measurement in figure A.3 is likely dominated by measurement errors. Those could be caused imaging distortions or a nonlinear correlation of wavelength and camera position. As the deviation in figure A.3 **d)** does not show a linear deviation of the propagation angle, the linear regression of the deviation depends highly on the chosen region of the image that is analyzed. For the given setup the measurement precision is approx-

imately $\pm 0.5\,\mu\text{rad}\,\text{nm}^{-1}$, which is significantly too low for the LWFA experiments as shown in section 7.3.

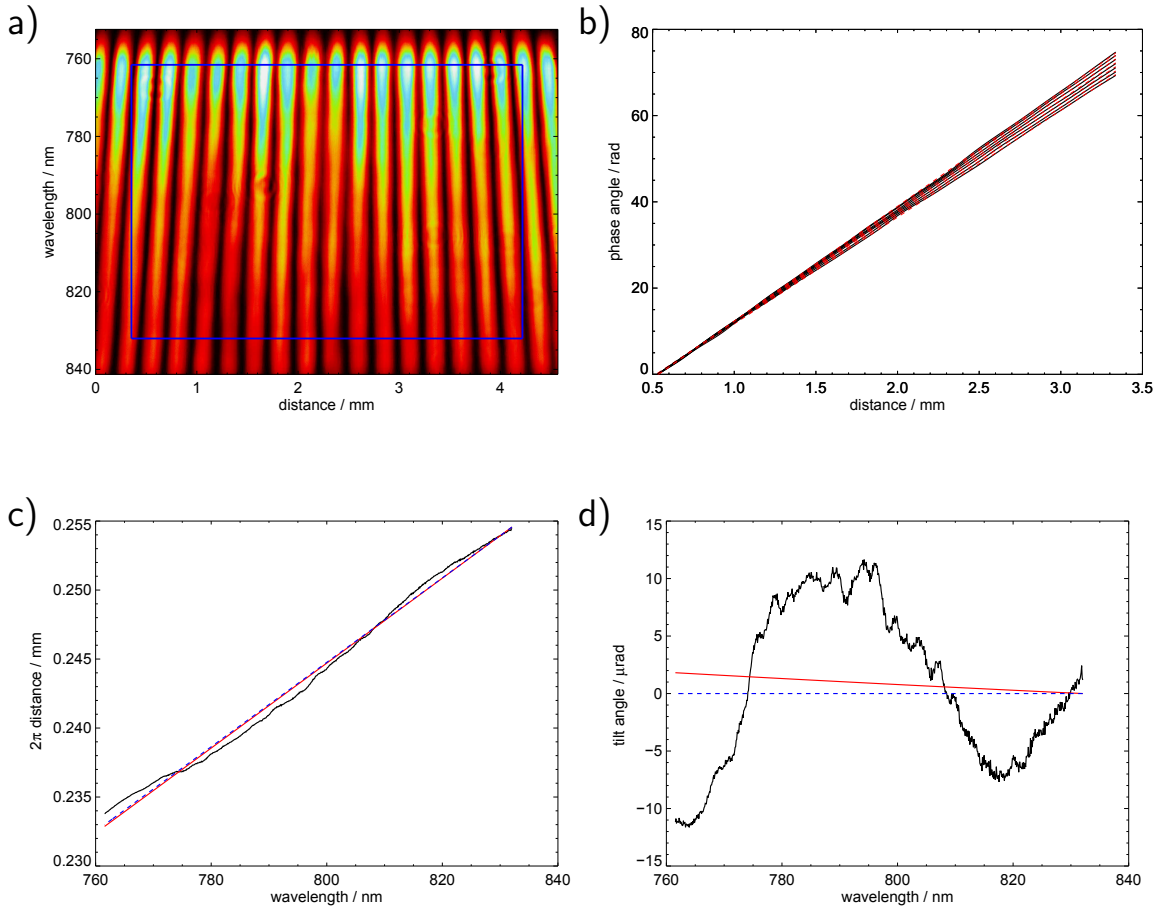

Figure A.3: Step by step illustration of data analysis used to measure angular chirp. **a)** Original image obtained from the spectrograph with ROI (blue box) **b)** Phase angle as function of distance for 770 nm to 830 nm in 10 nm steps. **c)** Fitted average 2π distance as function of wavelength **d)** measured deviation angle as function of wavelength. In **c)** and **d)** the blue dashed line represents no angular chirp and red solid the fitted deviation using linear regression.

List of Figures

List of Tables

Bibliography

[1] T. Tajima and J. M. Dawson, "Laser electron accelerator", Phys. Rev. Lett. **43**, 267–270 (1979) (cit. on pp. 1, 21).

[2] W. Lu, M. Tzoufras, C. Joshi, F. S. Tsung, W. B. Mori, J. Vieira, R. A. Fonseca, and L. O. Silva, "Generating multi-gev electron bunches using single stage laser wakefield acceleration in a 3d nonlinear regime", Phys. Rev. ST Accel. Beams **10**, 061301 (2007) (cit. on pp. 1, 2, 17, 21, 23, 25, 39, 110).

[3] W. P. Leemans, A. J. Gonsalves, H.-S. Mao, K. Nakamura, C. Benedetti, C. B. Schroeder, C. Toth, J. Daniels, D. E. Mittelberger, S. S. Bulanov, J.-L. Vay, C. G. R. Geddes, and E. Esarey, "Multi-gev electron beams from capillary-discharge-guided subpetawatt laser pulses in the self-trapping regime", Phys. Rev. Lett. **113**, 245002 (2014) (cit. on p. 1).

[4] A. Modena, Z. Najmudin, A. Dangor, C. Clayton, K. A. Marsh, C. Joshi, V. Malka, C. Darrow, C. Danson, D. Neely, and F. Walsh, "Electron acceleration from the breaking of relativistic plasma waves", Nature **377**, 606–608 (1995) (cit. on pp. 1, 21).

[5] C. E. Clayton, C. Joshi, C. Darrow, and D. Umstadter, "Relativistic plasma-wave excitation by collinear optical mixing", Phys. Rev. Lett. **54**, 2343–2346 (1985) (cit. on pp. 1, 21).

[6] J. Osterhoff, A. Popp, Z. Major, B. Marx, T. P. Rowlands-Rees, M. Fuchs, M. Geissler, R. Hoerlein, B. Hidding, S. Becker, E. A. Peralta, U. Schramm, F. Gruener, D. Habs, F. Krausz, S. M. Hooker, and S. Karsch, "Generation of stable, low-divergence electron beams by laser-wakefield acceleration in a steady-state-flow gas cell", Phys. Rev. Lett. **101**, 085002 (2008) (cit. on p. 1).

[7] S. Kuschel, D. Hollatz, T. Heinemann, O. Karger, M. B. Schwab, D. Ullmann, A. Knetsch, A. Seidel, C. Roedel, M. Yeung, M. Leier, A. Blinne, H. Ding, T. Kurz, D. J. Corvan, A. Sävert, S. Karsch, M. C. Kaluza, B. Hidding, and M. Zepf, "Demonstration of passive plasma lensing of a laser wakefield accelerated electron bunch", Phys. Rev. Accel. Beams **19**, 071301 (2016) (cit. on pp. 1, 93, 111).

[8] W. P. Leemans, B. Nagler, A. J. Gonsalves, C. Toth, K. Nakamura, C. G. R. Geddes, E. Esarey, C. B. Schroeder, and S. M. Hooker, "Gev electron beams from a centimetre-scale accelerator", Nat Phys **2**, 696–699 (2006) (cit. on pp. 2, 17, 31).

[9] S. P. D. Mangles, G. Genoud, M. S. Bloom, M. Burza, Z. Najmudin, A. Persson, K. Svensson, A. G. R. Thomas, and C.-G. Wahlstroem, "Self-injection threshold in self-guided laser wakefield accelerators", Phys. Rev. ST Accel. Beams **15**, 011302 (2012) (cit. on pp. 2, 25, 28, 32, 85, 89).

[10] C. McGuffey, A. G. R. Thomas, W. Schumaker, T. Matsuoka, V. Chvykov, F. J. Dollar, G. Kalintchenko, V. Yanovsky, A. Maksimchuk, K. Krushelnick, V. Y. Bychenkov, I. V. Glazyrin, and A. V. Karpeev, "Ionization induced trapping in a laser wakefield accelerator", Phys. Rev. Lett. **104**, 025004 (2010) (cit. on p. 2).

[11] K. Schmid, A. Buck, C. M. S. Sears, J. M. Mikhailova, R. Tautz, D. Herrmann, M. Geissler, F. Krausz, and L. Veisz, "Density-transition based electron injector for laser driven wakefield accelerators", Phys. Rev. ST Accel. Beams **13**, 091301 (2010) (cit. on pp. 2, 30, 99).

[12] J. Faure, C. Rechatin, A. Norlin, A. Lifschitz, Y. Glinec, and V. Malka, "Controlled injection and acceleration of electrons in plasma wakefields by colliding laser pulses", Nature **444**, 737–739 (2006) (cit. on pp. 2, 31, 112).

[13] A. J. Gonsalves, K. Nakamura, C. Lin, D. Panasenko, S. Shiraishi, T. Sokollik, C. Benedetti, C. B. Schroeder, C. G. R. Geddes, J. van Tilborg, J. Osterhoff, E. Esarey, C. Toth, and W. P. Leemans, "Tunable laser plasma accelerator based on longitudinal density tailoring", Nat Phys **7**, 862–866 (2011) (cit. on pp. 2, 30, 112).

[14] B. B. Pollock, C. E. Clayton, J. E. Ralph, F. Albert, A. Davidson, L. Divol, C. Filip, S. H. Glenzer, K. Herpoldt, W. Lu, K. A. Marsh, J. Meinecke, W. B. Mori, A. Pak, T. C. Rensink, J. S. Ross, J. Shaw, G. R. Tynan, C. Joshi, and D. H. Froula, "Demonstration of a narrow energy spread, 0.5 gev electron beam from a two-stage laser wakefield accelerator", Phys. Rev. Lett. **107**, 045001 (2011) (cit. on pp. 2, 31, 112).

[15] A. Buck, J. Wenz, J. Xu, K. Khrennikov, K. Schmid, M. Heigoldt, J. M. Mikhailova, M. Geissler, B. Shen, F. Krausz, S. Karsch, and L. Veisz, "Shock-front injector for high-quality laser-plasma acceleration", Phys. Rev. Lett. **110**, 185006 (2013) (cit. on pp. 2, 25, 30, 99, 107).

[16] J. Lawson et al., "Lasers and accelerators", IEEE Trans. Nucl. Sci **26**, 4217–4219 (1979) (cit. on p. 7).

[17] P. Gibbon, *Short pulse laser interactions with matter: an introduction.* (World Scientific Publishing Company, 2005) (cit. on pp. 7, 10–12).

[18] V. K. M.V. Ammosov N.B. Delanov, "Tunnel ionization of complex atoms and of atomic ions in an alternating electromagnetic field", Journal of Experimental and Theoretical Physics **64**, 1191 (1986) (cit. on p. 8).

[19] T. W. B. Kibble, "Mutual refraction of electrons and photons", Phys. Rev. **150**, 1060–1069 (1966) (cit. on p. 13).

[20] B. Quesnel and P. Mora, "Theory and simulation of the interaction of ultraintense laser pulses with electrons in vacuum", Physical Review E **58**, 3719–3732 (1998) (cit. on p. 13).

[21] P. Sprangle, E. Esarey, and A. Ting, "Nonlinear theory of intense laser-plasma interactions", Phys. Rev. Lett. **64**, 2011–2014 (1990) (cit. on p. 17).

[22] C. Delfin, V. Lokhnygin, J. Mauritsson, A. Sjoegren, C.-G. Wahlstroem C.-G.m, A. Pukhov, and G. D. Tsakiris, "Influence of laser pulse duration on relativistic channels", Physics of Plasmas **9**, 937–940 (2002) (cit. on p. 17).

[23] W. Mori, "The physics of the nonlinear optics of plasmas at relativistic intensities for short-pulse lasers", Quantum Electronics, IEEE Journal of **33**, 1942–1953 (1997) (cit. on pp. 18, 19).

[24] Z. Najmudin, K. Krushelnick, M. Tatarakis, E. L. Clark, C. N. Danson, V. Malka, D. Neely, M. I. K. Santala, and A. E. Dangor, "The effect of high intensity laser propagation instabilities on channel formation in underdense plasmas", Physics of Plasmas **10**, 438–442 (2003) (cit. on p. 20).

[25] V. Malka, J. Faure, J. R. Marques, F. Amiranoff, C. Courtois, Z. Najmudin, K. Krushelnick, M. R. Salvati, and A. E. Dangor, "Interaction of ultraintense laser pulses with an underdense, preformed plasma channel", IEEE Transactions on Plasma Science **28**, 1078–1083 (2000) (cit. on p. 20).

[26] D. E. Hinkel, E. A. Williams, R. L. Berger, L. V. Powers, A. B. Langdon, and C. H. Still, "Propagation of realistic beams in underdense plasma", Physics of Plasmas **5**, 1887–1894 (1998) (cit. on p. 20).

[27] F. Vidal and T. W. Johnston, "Electromagnetic beam breakup: multiple filaments, single beam equilibria, and radiation", Phys. Rev. Lett. **77**, 1282–1285 (1996) (cit. on p. 20).

[28] M. Schnell, A. Sävert, I. Uschmann, M. Reuter, M. Nicolai, T. Kämpfer, B. Landgraf, O. Jäckel, O. Jansen, A. Pukhov, M. C. Kaluza, and C. Spielmann, "Optical control of hard x-ray polarization by electron injection in a laser wakefield accelerator", Nat Commun **4** (2013) (cit. on pp. 20, 105).

[29] M. C. Kaluza, S. P. D. Mangles, A. G. R. Thomas, Z. Najmudin, A. E. Dangor, C. D. Murphy, J. L. Collier, E. J. Divall, P. S. Foster, C. J. Hooker, A. J. Langley, J. Smith, and K. Krushelnick, "Observation of a long-wavelength hosing modulation of a high-intensity laser pulse in underdense plasma", Phys. Rev. Lett. **105**, 095003 (2010) (cit. on p. 20).

[30] K. V. Gorbunov L.M., "The excitation of plasma waves by an electromagnetic wave packet", Journal of Experimental and Theoretical Physics **93**, 509–518 (1987) (cit. on p. 22).

[31] P. Sprangle, E. Esarey, A. Ting, and G. Joyce, "Laser wakefield acceleration and relativistic optical guiding", Applied Physics Letters **53**, 2146–2148 (1988) (cit. on p. 22).

[32] E. Esarey, P. Sprangle, J. Krall, and A. Ting, "Overview of plasma-based accelerator concepts", IEEE Transactions on Plasma Science **24**, 252–288 (1996) (cit. on p. 22).

[33] E. A. Jackson, "Nonlinear oscillations in a cold plasma", Physics of Fluids **3**, 831–833 (1960) (cit. on p. 23).

[34] R. P. A. I. Akhiezer, "Theory of wave motion of an electron plasma", Journal of Experimental and Theoretical Physics **3**, 696 (1956) (cit. on pp. 24, 25).

[35] J. M. Dawson, "Nonlinear electron oscillations in a cold plasma", Phys. Rev. **113**, 383–387 (1959) (cit. on p. 25).

[36] R. M. G. M. Trines and P. A. Norreys, "Wave-breaking limits for relativistic electrostatic waves in a one-dimensional warm plasma", Physics of Plasmas **13**, 123102 (2006) (cit. on p. 25).

[37] S. Gordienko and A. Pukhov, "Scalings for ultrarelativistic laser plasmas and quasimonoenergetic electrons", Physics of Plasmas **12**, 043109 (2005) (cit. on pp. 25, 27).

[38] A. G. R. Thomas, "Scalings for radiation from plasma bubblesa)", Physics of Plasmas **17**, 056708 (2010) (cit. on p. 28).

[39] C. D. Decker, W. B. Mori, K. Tzeng, and T. Katsouleas, "The evolution of ultra-intense, shor-pulse lasers in underdense plasmas", Physics of Plasmas **3**, 2047–2056 (1996) (cit. on p. 28).

[40] J. Schreiber, C. Bellei, S. P. D. Mangles, C. Kamperidis, S. Kneip, S. R. Nagel, C. A. J. Palmer, P. P. Rajeev, M. J. V. Streeter, and Z. Najmudin, "Complete temporal characterization of asymmetric pulse compression in a laser wakefield", Phys. Rev. Lett. **105**, 235003 (2010) (cit. on p. 28).

[41] B. Holzer, V.Malka, P. Gibbon, B. Bingham, J. Vieira, Z. Najmudin, P. Muggli, J. Faure, M. Ferrario, A. Pukhov, B. Cros, M. Roth, E. Gschwendtner, S. Mangles, and J. Osterhoff, *Proceedings of the 2014 cas-cern accelerator school: plasma wake acceleration*, edited by B. Holzer, Vol. 1 (CERN, 2016) (cit. on p. 29).

[42] I. Kostyukov, A. Pukhov, and S. Kiselev, "Phenomenological theory of laser-plasma interaction in bubble regime", Physics of Plasmas **11**, 5256–5264 (2004) (cit. on p. 29).

[43] E. Esarey, B. A. Shadwick, P. Catravas, and W. P. Leemans, "Synchrotron radiation from electron beams in plasma-focusing channels", Phys. Rev. E **65**, 056505 (2002) (cit. on p. 29).

[44] S. Corde, K. Ta Phuoc, G. Lambert, R. Fitour, V. Malka, A. Rousse, A. Beck, and E. Lefebvre, "Femtosecond x rays from laser-plasma accelerators", Rev. Mod. Phys. **85**, 1–48 (2013) (cit. on p. 29).

[45] M. Hansson, B. Aurand, X. Davoine, H. Ekerfelt, K. Svensson, A. Persson, C.-G. Wahlstroem, and O. Lundh, "Down-ramp injection and independently controlled acceleration of electrons in a tailored laser wakefield accelerator", Phys. Rev. ST Accel. Beams **18**, 071303 (2015) (cit. on pp. 30, 112).

[46] M. Mirzaie, S. Li, M. Zeng, N. A. M. Hafz, M. Chen, G. Y. Li, Q. J. Zhu, H. Liao, T. Sokollik, F. Liu, Y. Y. Ma, L. Chen, Z. M. Sheng, and J. Zhang, "Demonstration of self-truncated ionization injection for gev electron beams", Scientific Reports **5**, 14659– (2015) (cit. on p. 31).

[47] M. Tzoufras, W. Lu, F. S. Tsung, C. Huang, W. B. Mori, T. Katsouleas, J. Vieira, R. A. Fonseca, and L. O. Silva, "Beam loading in the nonlinear regime of plasma-based acceleration", Phys. Rev. Lett. **101**, 145002 (2008) (cit. on p. 31).

[48] C. Rechatin, X. Davoine, A. Lifschitz, A. B. Ismail, J. Lim, E. Lefebvre, J. Faure, and V. Malka, "Observation of beam loading in a laser-plasma accelerator", Phys. Rev. Lett. **103**, 194804 (2009) (cit. on pp. 31, 102, 110).

[49] S. G. D. Beck H. Brand, "The cs framework - a labview based approach to scada systems", in Proceedings of the icalepcs 2005 (2005) (cit. on p. 39).

[50] A. Ferrari, P. Sala, R. Guaraldi, and F. Padoani, "An improved multiple scattering model for charged particle transport", Nuclear Instruments and Methods in Physics Research Section B: Beam Interactions with Materials and Atoms **71**, 412–426 (1992) (cit. on p. 39).

[51] S. Semushin and V. Malka, "High density gas jet nozzle design for laser target production", Review of Scientific Instruments **72**, 2961–2965 (2001) (cit. on pp. 43, 47).

[52] B. Landgraf, M. Schnell, A. Sävert, M. Kaluza, and C. Spielmann, "High resolution 3d gas-jet characterization", Review of Scientific Instruments **82**, 083106 (2011) (cit. on pp. 43, 45).

[53] K. Schmid and L. Veisz, "Supersonic gas jets for laser-plasma experiments", Review of Scientific Instruments **83**, 053304 (2012) (cit. on pp. 45, 48).

[54] K. Schmid, "Supersonic micro-jets and their application to few-cycle laser-driven electron acceleration", 2009 (cit. on pp. 46, 112).

[55] J. D. Jackson, *Classical electrodynamics third edition* (Wiley, 1998) (cit. on p. 53).

[56] T. Oksenhendler, D. Kaplan, P. Tournois, G. Greetham, and F. Estable, "Intracavity acousto-optic programmable gain control for ultra-wide-band regenerative amplifiers", Applied Physics B **83**, 491–494 (2006) (cit. on pp. 57, 59).

[57] C. Iaconis and I. A. Walmsley, "Spectral phase interferometry for direct electric-field reconstruction of ultrashort optical pulses", Opt. Lett. **23**, 792–794 (1998) (cit. on p. 59).

[58] P. Tournois, "Acousto-optic programmable dispersive filter for adaptive compensation of group delay time dispersion in laser systems", Optics Communications **140**, 245–249 (1997) (cit. on p. 59).

[59] G. S. A. Saevert, *Current status of the jeti 200 laser system*, tech. rep. (Helmholtz Institut Jena, Germany, 2014) (cit. on p. 62).

[60] G. Pretzler, A. Kasper, and K. Witte, "Angular chirp and tilted light pulses in cpa lasers", Applied Physics B **70**, 1–9 (2000) (cit. on p. 64).

[61] K. Varju, A. Kovacs, G. Kurdi, and K. Osvay, "High-precision measurement of angular dispersion in a cpa laser", Applied Physics B **74**, s259–s263 (2002) (cit. on pp. 64, 117).

[62] J. Müller, "Fokusoptimierung an einem hochintensitaetslaser mit hilfe einer adaptiven optik unter verwendung der programmiersprache labview", MA thesis (Friedrich-Schiller-Universitaet Jena, 2014) (cit. on p. 66).

[63] A. Buck, K. Zeil, A. Popp, K. Schmid, A. Jochmann, S. D. Kraft, B. Hidding, T. Kudyakov, C. M. S. Sears, L. Veisz, S. Karsch, J. Pawelke, R. Sauerbrey, T. Cowan, F. Krausz, and U. Schramm, "Absolute charge calibration of scintillating screens for relativistic electron detection", Review of Scientific Instruments **81**, 033301 (2010) (cit. on pp. 67, 69).

[64] K. Nakamura, A. J. Gonsalves, C. Lin, A. Smith, D. Rodgers, R. Donahue, W. Byrne, and W. P. Leemans, "Electron beam charge diagnostics for laser plasma accelerators", Phys. Rev. ST Accel. Beams **14**, 062801 (2011) (cit. on pp. 67, 68).

[65] J. Bahrdt, W. Frentrup, A. Gaupp, M. Scheer, and U. Englisch, "Magnetic field optimization of permanent magnet undulators for arbitrary polarization", Nuclear Instruments and Methods in Physics Research Section A: Accelerators, Spectrometers, Detectors and Associated Equipment **516**, 575–585 (2004) (cit. on p. 69).

[66] J. C. O. Chubar P. Elleaume, "A 3d magnetostatics computer code for insertion devices", in Sri97 conference august 1997 (1997) (cit. on p. 69).

[67] M. de Loos, "General particle tracer: a new 3d code for accelerator and beamline design", Proceedings of EPAC 1996, Sitges, Spain (1996) (cit. on p. 70).

[68] A. Popp, J. Vieira, J. Osterhoff, Z. Major, R. Hoerlein, M. Fuchs, R. Weingartner, T. P. Rowlands-Rees, M. Marti, R. A. Fonseca, S. F. Martins, L. O. Silva, S. M. Hooker, F. Krausz, F. Gruener, and S. Karsch, "All-optical steering of laser-wakefield-accelerated electron beams", Phys. Rev. Lett. **105**, 215001 (2010) (cit. on pp. 83, 84).

[69] A. Sävert, S. P. D. Mangles, M. Schnell, E. Siminos, J. M. Cole, M. Leier, M. Reuter, M. B. Schwab, M. Moeller, K. Poder, O. Jäckel, G. G. Paulus, C. Spielmann, S. Skupin, Z. Najmudin, and M. C. Kaluza, "Direct observation of the injection dynamics of a laser wakefield accelerator using few-femtosecond shadowgraphy", Phys. Rev. Lett. **115**, 055002 (2015) (cit. on pp. 91, 112).

[70] A. Pak, K. A. Marsh, S. F. Martins, W. Lu, W. B. Mori, and C. Joshi, "Injection and trapping of tunnel-ionized electrons into laser-produced wakes", Phys. Rev. Lett. **104**, 025003 (2010) (cit. on p. 96).

[71] G. Z. Sun, E. Ott, Y. C. Lee, and P. Guzdar, "Self focusing of short intense pulses in plasmas", Physics of Fluids **30**, 526–532 (1987) (cit. on pp. 96, 109).

[72] G. Golovin, S. Banerjee, S. Chen, N. Powers, C. Liu, W. Yan, J. Zhang, P. Zhang, B. Zhao, and D. Umstadter, "Control and optimization of a staged laser-wakefield accelerator", Nuclear Instruments and Methods in Physics Research Section A: Accelerators, Spectrometers, Detectors and Associated Equipment **830**, 375–380 (2016) (cit. on pp. 103, 111, 112).

[73] J. M. Cole, J. C. Wood, N. C. Lopes, K. Poder, R. L. Abel, S. Alatabi, J. S. J. Bryant, A. Jin, S. Kneip, K. Mecseki, D. R. Symes, S. P. D. Mangles, and Z. Najmudin, "Laser-wakefield accelerators as hard x-ray sources for 3d medical imaging of human bone", Scientific Reports **5**, 13244– (2015) (cit. on p. 105).

[74] J. van Tilborg, S. Steinke, C. G. R. Geddes, N. H. Matlis, B. H. Shaw, A. J. Gonsalves, J. V. Huijts, K. Nakamura, J. Daniels, C. B. Schroeder, C. Benedetti, E. Esarey, S. S. Bulanov, N. A. Bobrova, P. V. Sasorov, and W. P. Leemans, "Active plasma lensing for relativistic laser-plasma-accelerated electron beams", Phys. Rev. Lett. **115**, 184802 (2015) (cit. on p. 111).

[75] A. Buck, M. Nicolai, K. Schmid, C. M. S. Sears, A. Savert, J. M. Mikhailova, F. Krausz, M. C. Kaluza, and L. Veisz, "Real-time observation of laser-driven electron acceleration", Nat Phys **7**, 543–548 (2011) (cit. on p. 112).

Acknowledgments

I am using this opportunity to express my gratitude to everyone who contributed to this work and supported me during my time as a Ph.D. student. Without their help, enthusiasm and fruitful discussions this thesis would not have been possible. In particular, I would like to thank the following people:

- Prof. Dr. W. Sandner for giving me the opportunity to be part of this excellent group at the MBI. I am sorry that he could not live to see me graduate.
- Prof. Dr. Andreas Jankowiak for the credit of trust granted by becoming my supervisor.
- Prof. Dr. Matt Zepf and Prof. Dr. Lazlo Veisz for being referees of this thesis.
- Dr. M. Schnürer for his extraordinary dedication, competence, mentoring and help.
- Prof. Dr. Malte Kaluza and Dr. Johannes Bahrdt for providing advice and resources for the experimental work
- Dr. Alexander Sävert for his outstanding assistance and mentoring that he offered, despite having no obligation to do so.
- Dr. Andrea Lübke for her very detailed reviews of my thesis.
- J. Bränzel for her friendly support and Dr. Florian Abicht for his help, support and for the Latex template of this thesis.
- Dr. H. Stiel, L. Ehrentraut, M. Heinicke, D. Sommer, G. Kommol and D. Rohloff, P. Friedrich, S. Szlapka, B. Becker, J. Meißner and J. Gläsel.
- The group at LBNL for teaching me about LWFA. In particular Prof. Dr. W. Leemans, Dr. T. Sokollik, N. Ybarrolaza, Dr. S. Steinke
- Last but not least, my family for their personal support and Carolin Schneemann for her support in the toughest times of this project

Selbstständigkeitserklärung

Ich erkläre, dass ich die Dissertation selbständig und nur unter Verwendung der von mir gemäß § 7 Abs. 3 der Promotionsordnung der Mathematisch-Naturwissenschaftlichen Fakultät, veröffentlicht im Amtlichen Mitteilungsblatt der Humboldt-Universität zu Berlin Nr. 126/2014 am 18.11.2014 angegebenen Hilfsmittel angefertigt habe.